PE&RS

December 2022

Volume 88, Number 12

PHOTOGRAMMETRIC ENGINEERING & REMOTE SENSING

The official journal for imaging and geospatial information science and technology

Digital Elevation Model Technologies and Applications: The DEM Users Manual, 3rd Edition

Edited by David F. Maune, PhD, CP and Amar Nayegandhi, CP, CMS

To order, visit https://www.asprs.org/dem

The 3rd edition of the DEM Users Manual includes 15 chapters and three appendices. References in the eBook version are hyperlinked. Chapter and appendix titles include:

1. Introduction to DEMs
   David F. Maune, Hans Karl Heidemann, Stephen M. Kopp, and Clayton A. Crawford
2. Vertical Datums
   Dru Smith
3. Standards, Guidelines & Specifications
   David F. Maune
4. The National Elevation Dataset (NED)
   Dean B. Gesch, Gayla A. Evans, Michael J. Oimoen, and Samantha T. Arundel
5. The 3D Elevation Program (3DEP)
   Jason M. Stoker, Vicki Lukas, Allyson L. Jason, Diane F. Eldridge, and Larry J. Sugarbaker
6. Photogrammetry
   J. Chris McGlone and Scott Arko
7. IfSAR
   Scott Hensley and Lorraine Tighe
8. Airborne Topographic Lidar
   Amar Nayegandhi and Joshua Nimetz
9. Lidar Data Processing
   Joshua M. Novac
10. Airborne Lidar Bathymetry
    Jennifer Wozencraft and Amar Nayegandhi
11. Sonar
    Guy T. Noll and Douglas Lockhart
12. Enabling Technologies
    Bruno M. Scherzinger, Joseph J. Hutton, and Mohamed M.R. Mostafa
13. DEM User Applications
    David F. Maune
14. DEM User Requirements & Benefits
    David F. Maune
15. Quality Assessment of Elevation Data
    Jennifer Novac

Appendix A. Acronyms

Appendix B. Definitions

Appendix C. Sample Datasets

This book is your guide to 3D elevation technologies, products and applications. It will guide you through the inception and implementation of the U.S. Geological Survey's (USGS) 3D Elevation Program (3DEP) to provide not just bare earth DEMs, but a full suite of 3D elevation products using Quality Levels (QLs) that are standardized and consistent across the U.S. and territories. The 3DEP is based on the National Enhanced Elevation Assessment (NEEA) which evaluated 602 different mission-critical requirements for and benefits from enhanced elevation data of various QLs for 34 Federal agencies, all 50 states (with local and Tribal input), and 13 non-governmental organizations.

The NEEA documented the highest Return on Investment from QL2 lidar for the conterminous states, Hawaii and U.S. territories, and QL5 IfSAR for Alaska.

Chapters 3, 5, 8, 9, 13, 14, and 15 are "must-read" chapters for users and providers of topographic lidar data. Chapter 8 addresses linear mode, single photon and Geiger mode lidar technologies, and Chapter 10 addresses the latest in topobathymetric lidar. The remaining chapters are either relevant to all DEM technologies or address alternative technologies including photogrammetry, IfSAR, and sonar.

As demonstrated by the figures selected for the front cover of this manual, readers will recognize the editors' vision for the future – a 3D Nation that seamlessly merges topographic and bathymetric data from the tops of the mountains, beneath rivers and lakes, to the depths of the sea.

Co-Editors

David F. Maune, PhD, CP and
Amar Nayegandhi, CP, CMS

PRICING

Student (must submit copy of Student ID)	\$50 +S&H
ASPRS Member	\$80 +S&H
Non-member	\$100 +S&H
E-Book (only available in the Amazon Kindle store)	\$85

To have your press release published in *PE&RS*, contact Rae Kelley, rkelley@asprs.org.

ANNOUNCEMENTS

NV5 Geospatial is transforming the way utilities manage their distribution networks with remote sensing data analysis. Having mapped more than 5.5 million miles of utility distribution networks in the U.S., NV5 Geospatial offers proven solutions that combine a variety of lidar and orthoimagery sensors on mobile and airborne platforms to acquire data for both asset and vegetation management. Analysis of this geospatial data then enables electric utilities to minimize risk and maximize reliability, while increasing efficiency.

"An aging grid, workforce shortages, increasing energy demands and an uptick in major weather events are combining to create a perfect storm that could impact reliability, customer service and safety for electric utilities across the country," said Eric Merten, Vice President, Commercial Group at NV5 Geospatial. "A boots-on-the-ground approach to management cannot keep up with demands related to aging equipment, compliance, pole loading and vegetation encroaching on infrastructure. NV5 Geospatial's innovative remote sensing applications and data analysis tools give utilities the power to proactively address problems in their distribution network before they impact operations or customers."

Built on the success of its remote sensing applications for utility transmission networks, NV5 Geospatial's distribution management solutions offer end-to-end capabilities – from acquiring accurate, high-quality geospatial data to data analysis and visualization using custom viewers and enterprise GIS – and can be customized to meet utilities use cases and budgets.

With a single data collection via remote sensing, NV5 Geospatial makes it easier for utilities to manage, maintain and monitor their distribution networks, whether it relates to their assets and infrastructure, or vegetation that may interfere with it.

Asset Management — NV5 Geospatial remote sensing processes involve more than 25 asset measurements, quickly delivering a comprehensive inventory of utility pole capacity with greater accuracy than traditional boots-on-the-ground surveys. Using NV5 Geospatial's tools, distribution network asset managers can:

- Achieve compliance with National Electrical Safety Code (NESC) clearance guidelines
- Get clear visibility into joint use of poles to prevent pirating, which can be a safety risk because of overcapacity issues, and increase revenue opportunities if poles are capable of supporting attachments of additional communications wires and equipment
- Ensure safe pole loading through analysis of weight load on each pole to prevent breaking or falling during severe weather and get insight into whether the pole can handle more joint use applications

Vegetation Management — NV5 Geospatial's remote sensing data also can help vegetation managers quantify vegetation with distribution rights-of-way and determine risk based on proximity to wires and poles. With customized data inputs and analysis parameters, vegetation managers can improve decision-making and prioritize tree trimming work where risks are greatest. NV5 Geospatial's vegetation management analytics also play a key role in helping utilities save millions of dollars during contractor negotiations and bidding processes by clearly identifying where work needs to be done.

To learn more about NV5 Geospatial Distribution Solutions, go to: https://www.nv5.com/distribution-solutions/.

UP42 made the first major announcement of its new partnership with the introduction of the UP42 ArcGIS Pro Add-in. Available on the **Esri ArcGIS Marketplace**, the UP42 add-in allows users to access UP42 data sets and projects from within ArcGIS Pro.

UP42, a Silver Partner in the Esri Partner Network (EPN), unveiled the add-in today in stand C1.020 at the INTERGEO 2022 Conference this week in Essen, Germany.

Esri's ArcGIS Pro is a standalone application extensively used by geospatial solution builders, GIS professionals and developers to visualize, analyze, compile, and share geospatial data. The UP42 marketplace currently contains over 160 satellite and aerial image products and derived data sets along with dozens of processing algorithms from leading geospatial organizations.

"By integrating UP42 and Esri, we have given users a streamlined way to access the data and analytics products they purchase on UP42 directly from ArcGIS Pro," said UP42 CEO Sean Wiid. "This dramatically simplifies imagery analysis workflows and facilitates advanced geospatial visualization."

The UP42 add-in will significantly reduce the time it takes to access data, build visualization workflows, and develop geospatial solutions. Without leaving the Esri ArcGIS environment, customers can use the new add-in to access the UP42 platform where they can open projects they are already working on, download purchased data sets into ArcGIS and view metadata. New geospatial data products will soon be available for order through the add-in.

The UP42 ArcGIS Pro Add-in is available at no cost and can be downloaded from the UP42 Marketplace or the Esri ArcGIS Marketplace.

Teledyne FLIR Integrated Imaging Solutions is pleased to announce the all new Ladybug6— the latest addition to its field proven Ladybug series. Ladybug6 is the leading high-resolution camera designed to capture 360-degree spherical images from moving platforms in all-weather conditions. Its industrial grade design and out-of-the-box factory calibration produces 72 Megapixel (MP) images with pixel values that are spatially accurate within +/- 2 mm at 10-meter distance.

"The new Teledyne Ladybug6 is designed for mobile mapping and all-weather inspection projects requiring excellent image quality and high resolution," said Mike Lee, Senior Product Manager at Teledyne FLIR. "With the addition of Ladybug6, we are now pleased to offer a wider variety of spherical cameras with higher resolutions ranging from 30 MP to 72 MP."

The new Ladybug6 builds on Teledyne's machine vision heritage with increased image resolution, enhanced on-board processing, and robust IP67-rated connectors. Building on the field proven Ladybug5+, the Ladybug6 captures, compresses, and transmits 8-bit or 12-bit pixel data delivering outstanding images across a wide range of lighting conditions with excellent color response, low noise, and a high dynamic range. Designed from the ground up to capture images from moving platforms in outdoor environments, the Ladybug6 features a wide operating temperature range (-30° C to 50° C), support for additional Global Navigation Satellite Systems, and trigger control by hardware or software with advanced APIs for complete camera control.

Ladybug6 cameras are engineered to deliver high-accuracy, high-resolution, and dependable results for applications such as HD mapping, asset management, roadside inspection, panoramic street image production for street view, road surveying, heritage scanning, building management, among several others.

For more information about Ladybug6 models www.flir.com/products/ladybug6/.

CALENDAR

- 27 January, **ASPRS GeoByte — Allen Coral Atlas: A New Technology for Coral Reef Conservation**. For more information, visit https://www.asprs.org/geobytes.html.
- 15-17 February, **ASPRS Annual Conference at Geo Week**, Denver, Colorado. For more information, visit https://my.asprs.org/2023conference.
- 5 May, **ASPRS GeoByte — SeaSketch 2.0: A New, Free and Open Source software Service for Map-based Surveys and Collaborative Geodesign.** For more information, visit https://www.asprs.org/geobytes.html.

PE&RS

PHOTOGRAMMETRIC ENGINEERING & REMOTE SENSING

The official journal for imaging and geospatial information science and technology

December 2022 Volume 88 Number 12

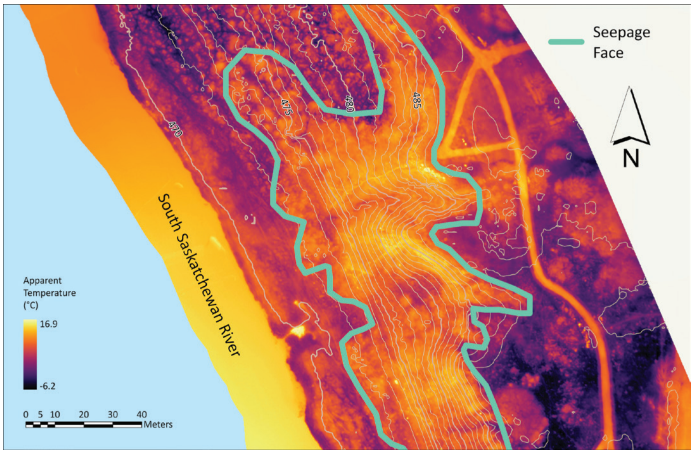

COLUMNS

ANNOUNCEMENTS

DEPARTMENTS

Both UAV photogrammetry and lidar have become common in deriving three-dimensional models of urban scenes, and each has its own advantages and disadvantages. However, the fusion of these multi-source data is still challenging, in which registration is one of the most important stages. In this article, we propose a method of coarse point cloud registration which consists of two steps. The first step is to extract urban building facades in both an oblique photogrammetric point cloud and a lidar point cloud. The second step is to align the two point clouds using the extracted building facades.

Over the last two decades, urban growth has become a major issue in Lahore, accelerating land surface temperature (LST) rise. The present study focused on estimating the current situation and simulating the future LST patterns in Lahore using remote sensing data and machine learning models.

The permanganate index (CODMn), defined as a comprehensive index to measure the degree of surface water pollution by organic matter and reducing inorganic matter, plays an important role in indicating water pollution and evaluating aquatic ecological health. However, remote sensing monitoring of water quality is presently focused mainly on phytoplankton, suspended particulate matter, and yellow substance, while there is still great uncertainty in the retrieval of CODMn. In this article, the Landsat-8 surface reflectance data set from Google Earth Engine and in situ CODMn measurements were matched. The support vector regression (SVR) machine learning model was calibrated using the matchups.

The Yangtze River Delta urban agglomeration (YRDUA) is one of the most active economic development regions in China. However, the YRDUA is facing a severe test of sustainable development. Therefore, this study evaluates the urban comprehensive carrying capacity (UCCC) of cities in the YRDUA from 2009 to 2019 from natural, social, and economic perspectives, and uses the Geographically and Temporally Weighted Regression model to analyze driving factors of spatiotemporal variations of the UCCC.

See the Cover Description on Page 744

COVER DESCRIPTION

On most days, South Australia's Lake Torrens shows up in satellite images as a relatively dry salt and mud flat. But in October 2022, a substantial amount of water returned to this ephemeral lake.

The Operational Land Imager-2 (OLI-2) on Landsat 9 acquired these images on October 28, 2022, when water spanned much of the lakebed. Wet areas are green-brown, salty surfaces are white, and land is red-brown.

Lake Torrens is located within in the east-central part of South Australia, just over 100 kilometers (60 miles) south of the Lake Eyre and 450 kilometers (280 miles) north of Adelaide. It lies between the Arcoona Plateau to the west and the Flinders Ranges to the east. The lake arose from a depression that formed east of the Torrens Fault about 70 million years ago. Today, it is one of Australia's largest inland salt lakes, and is a sacred site to nearby Aboriginal nations.

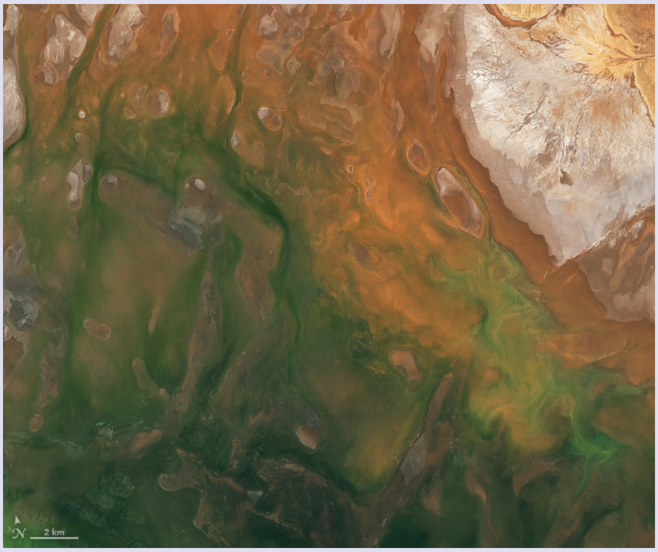

The region is generally very dry, averaging only a few hundred millimeters of rain each year. Unlike Lake Eyre, which receives most of its water from runoff during the summer monsoon, water in Lake Torrens depends primarily on rainfall from the southern hemisphere westerlies during winter.

Across South Australia, an unusually wet winter in 2022 has extended into spring, with the state seeing its wettest October on record (since 1900). Some areas, including the Flinders district, received more than 100 millimeters (4 inches) of rain, making it the wettest October on record. Areas around Roxby Downs, about 30 kilometers southwest of Andamooka, recorded more than eight times their average monthly rainfall for October.

Lake Torrens is typically endorheic, which means that the lake has no outflow and instead loses water via evaporation or seepage into the ground. That was probably still the case this year. But on rare occasions, most recently in 1989, extreme rainfall fills the lake with so much water that it flows south across the Pirie-Torrens corridor and into the Spencer Gulf.

To see the full image, visit https://landsat.visibleearth.nasa.gov/view.php?id=150566

NASA Earth Observatory images by Lauren Dauphin, using Landsat data from the U.S. Geological Survey. Story by Kathryn Hansen.

asprs

THE IMAGING & GEOSPATIAL INFORMATION SOCIETY

PHOTOGRAMMETRIC ENGINEERING & REMOTE SENSING

Journal Staff

Publisher ASPRS
Editor-In-Chief Alper Yilmaz
Director of Publications Rae Kelley
Electronic Publications Manager/Graphic Artist
Matthew Austin

Photogrammetric Engineering & Remote Sensing is the official journal of the American Society for Photogrammetry and Remote Sensing. It is devoted to the exchange of ideas and information about the applications of photogrammetry, remote sensing, and geographic information systems. The technical activities of the Society are conducted through the following Technical Divisions: Geographic Information Systems, Photogrammetric Applications, Lidar, Primary Data Acquisition, Professional Practice, Remote Sensing Applications, and Unmanned Autonomous Systems Division. Additional information on the functioning of the Technical Divisions and the Society can be found in the Yearbook issue of *PE&RS*.

Correspondence relating to all business and editorial matters pertaining to this and other Society publications should be directed to the American Society for Photogrammetry and Remote Sensing, 8550 United Plaza Boulevard, Suite 1001, Baton Rouge, LA 70809, including inquiries, memberships, subscriptions, changes in address, manuscripts for publication, advertising, back issues, and publications. The telephone number of the Society Headquarters is 301-493-0290; the fax number is 225-408-4422; web address is www.asprs.org.

PE&RS. *PE&RS* (ISSN0099-1112) is published monthly by the American Society for Photogrammetry and Remote Sensing, 425 Barlow Place, Suite 210, Bethesda, Maryland 20814-2144. Periodicals postage paid at Bethesda, Maryland and at additional mailing offices.

SUBSCRIPTION. For the 2022 subscription year, ASPRS is offering two options to our *PE&RS* subscribers — an e-Subscription and the print edition. e-Subscribers can add printed copies to their subscriptions for a small additional charge. Print and Electronic subscriptions are on a calendar-year basis that runs from January through December. We recommend that customers who choose print and e-Subscription with print renew on a calendar-year basis.

The rate for a Print subscription for the USA is $1105.00 USD, for Canadian* is $1164.00 USD, and for Non-USA is $1235.00 USD.

The rate for e-Subscription (digital) Site License for the USA and Non-USA is $1040.00 USD and for Canadian* is $1089.00 USD.

The rate for e-Subscription (digital) plus Print for the USA is $1405.00 USD, for Canadian* is $1464.00 USD, and for Non-USA is $1435.00 USD.

*Note: e-Subscription, Print subscription, and e-Subscription plus Print for Canada includes 5% of the total amount for Canada's Goods and Services Tax (GST #135123065). **PLEASE NOTE: All Subscription Agencies receive a 20.00 USD discount.**

POSTMASTER. Send address changes to *PE&RS*, ASPRS Headquarters, 8550 United Plaza Boulevard, Suite 1001, Baton Rouge, LA 70809. CDN CPM #(40020812).

MEMBERSHIP. Membership is open to any person actively engaged in the practice of photogrammetry, photointerpretation, remote sensing and geographic information systems; or who by means of education or profession is interested in the application or development of these arts and sciences. Membership is for one year, with renewal based on the anniversary date of the month joined. Membership Dues include a 12-month electronic subscription to *PE&RS*. To receive a print copy of *PE&RS* there is an additional postage fee of $60.00 USD for U.S. shipping; $65.00 USD for Canadian shipping; or $75.00 USD for international shipping per year. Annual Individual Member dues for members residing in the U.S. and Other Foreign Members are $150.00 USD and $158.00 USD for Canadians. Annual Student Member dues for members residing in the U.S. are $50.00 USD; $53.00 USD for Canadian; and $60.00 USD for Other Foreign Members. A tax of 5% for Canada's Goods and Service Tax (GST #135123065) is applied to all members residing in Canada.

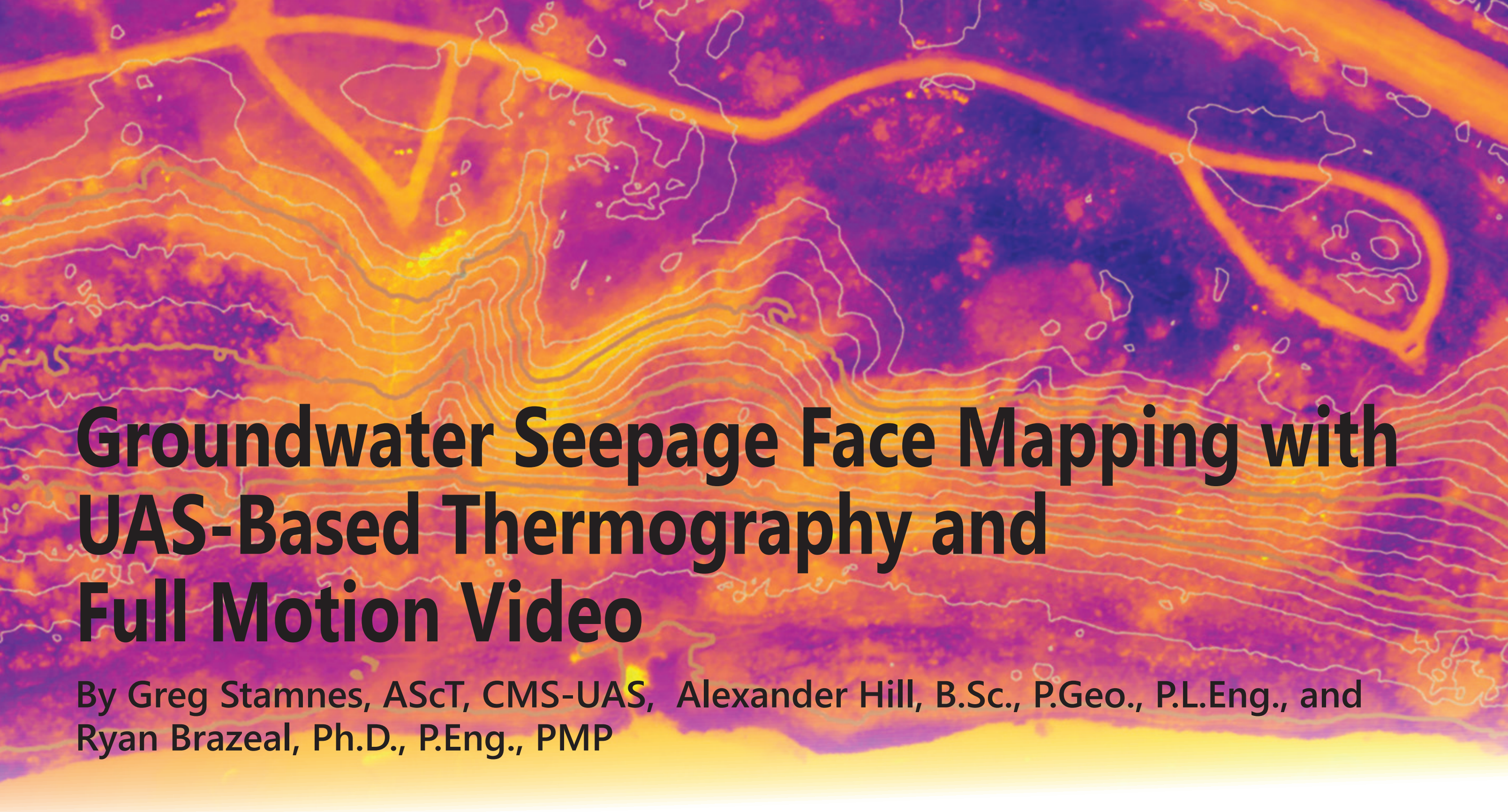

Groundwater Seepage Face Mapping with UAS-Based Thermography and Full Motion Video

By Greg Stamnes, AScT, CMS-UAS, Alexander Hill, B.Sc., P.Geo., P.L.Eng., and Ryan Brazeal, Ph.D., P.Eng., PMP

Introduction

Groundwater seepage is a geohazard which can be difficult to detect visually that contributes to terrain instability and possibly catastrophic failure (Budhu & Gobin, 1996; Alberta Environment, 2022). When terrain instability occurs near dams, highways, and other critical infrastructure, groundwater seepage can have immense economic, environmental, and public safety implications.

Groundwater seepage can be found by identifying the seepage face; the boundary where the flowing groundwater meets the atmosphere (Scudeler, et al., 2017). Identification is often achieved using remote sensing techniques and/or visual assessment via boots-on-the-ground survey. A variety of remote sensing techniques including image interpretation of stereo aerial images (e.g., terrain analysis of current and historical aerial photos), digital orthoimages, and more recently via thermography are utilized by hydrologists, geomorphologists, and geotechnical engineers to locate groundwater seepage faces (USGS, n.d.).

The use of thermographic sensors carried by Unoccupied Aerial Systems (UAS) can be an efficient alternative for identifying groundwater seepage faces. However, the method does have some limitations if the common practice of using a Structure from Motion (SfM) software package to produce a single orthorectified thermal index map from UAS-collected imagery is all that is utilized. This article highlights using Full Motion Video (FMV) to visually identify and georeference groundwater seepage locations using thermography.

There are also limitations of visual interpretation for groundwater seepage identification. Terrain analysis begins with the identification and distinguishing of elements of the landscape. These elements can typically be categorized as; topography or landform, drainage and erosion, vegetation and land-use (Mollard & Janes, 1984). This process requires the skills and knowledge of an analyst to determine the importance and significance of the identifiable features and elements of an observed landscape within the imagery, such as stereoscopic aerial photography.

A common approach is to conduct aerial photography analysis using softcopy photogrammetry. One of the many advantages to this approach is the ability to incorporate and overlay different sources of data and imagery including high-resolution digital aerial photography, orthorectified imagery, and Digital Elevation Models (DEM) to aid in the identification and interpretation of the landscape. This allows the analyst to navigate digitally in 3-Dimensional (3D) space without nominal scale constraints, which is especially important for viewing possible seepage faces. In the identification of groundwater seepage and drainage patterns using this method, the analyst is still reliant on visual cues, especially recognizing tone, shape, vegetation type and terrain relief.

Photogrammetric Engineering & Remote Sensing
Vol. 88, No. 12, December 2022, pp. 746-752.
0099-1112/22/746-752

doi: 10.14358/PERS.88.12.746

Analysts must acknowledge that site conditions may differ significantly when comparing conditions at the time of capture of the aerial photography to those currently being assessed. The occurrence of groundwater seepage at a particular area or site may be a function of other variables such as geology, ground stability, vegetation cover, human activity or be seasonal in nature. It is therefore possible that seasonal seepage issues may not be recognized by the analyst when conducting image interpretation of aerial photography alone. In Figure 1 this is illustrated by overlaying seepage identified from 1991 dated aerial photography interpretation (pink hatch), with more recent aerial photography interpretation (green hatch).

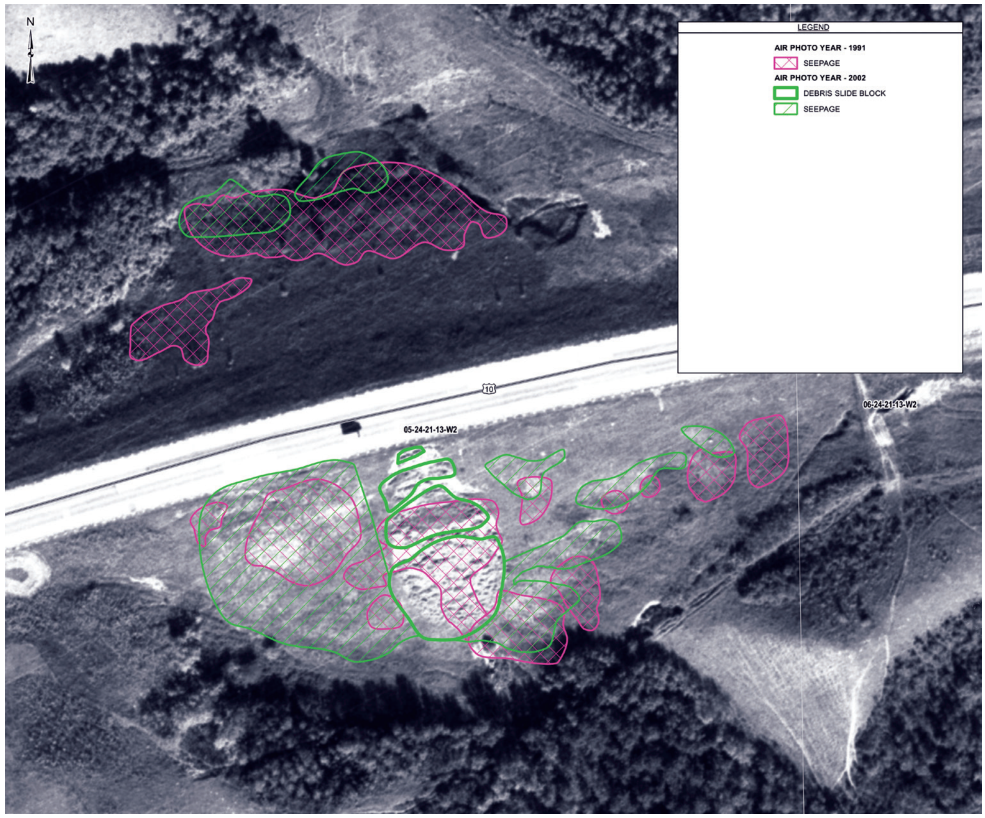

Figure 1: Typical black and white aerial photography used for terrain analysis and identification of potential seepage locations.

Analysis should include on-site ground truthing to validate the findings of the image interpretation phase and order to check the accuracy and relevancy of the mapped terrain features as shown in Figure 1. This is especially important when theorizing what relationships exist between landforms. Answering this question may also provide clues to where groundwater seepage may occur if not obvious from the aerial photography interpretation alone.

> ***Aerial thermography can be used in the context of groundwater seepage to answer two questions: firstly, are there radiometric indications when seepage is occurring within an area of interest, and secondly, where (geographically) is the seepage occurring?***

Aerial Thermography for Groundwater Seepage

Aerial thermography can be used in the context of groundwater seepage to answer two questions: firstly, are there radiometric indications when seepage is occurring within an area of interest, and secondly, where (geographically) is the seepage occurring?

Aerial thermal data acquisition for identifying seepage faces should be timed to commence when the greatest temperature difference occurs between the groundwater flow and the surrounding ground (Ozotta, 2021). This could be during late summer when the flowing groundwater is cooler than the surrounding warmer soil, or in the spring and autumn when the flowing groundwater is warmer than the cooler ground. However, there should not be snow cover on the ground, and the ground should not be deeply frozen during the acquisition of the thermal data (Harvey, et al., 2019). Data collection should occur at night with optimum meteorological conditions, including low wind speeds of less than 24 km/hr, humidity less than 50%, and no precipitation within the previous 24 hours (Infrared Training Center, 2019). Thermal sensors are a passive type of sensor and therefore suffer from environmental factors such as the effects of vegetation occlusion when mapping the ground surface (Ozotta, 2021; Infrared Training Center, 2019). As a result, it is recommended to conduct thermal imaging missions for groundwater seepage detection and mapping during the spring months before seasonal vegetation growth.

Our research was conducted on the riverbanks of the South Saskatchewan River near Saskatoon, SK, Canada in May, July, and October of 2020, and April, July, and November of 2021 in an area with known groundwater seepage.

The surficial geology of the test site comprises alluvial floodplain deposits and glaciofluvial kame terrace deposits (Christiansen, 1992). However, no forms of intrusive or non-invasive geotechnical/geological investigations were undertaken prior to thermal imaging of the test site.

Figure 2: Location of the research at the South Saskatchewan River. The study area along the river is about 650m long and 100m wide.

Thermal imagery datasets were collected using a DJI M200 UAS with a DJI Zenmuse XT2 payload with 13mm lens. The XT2 is a long-wave infrared (LWIR) camera with an uncooled VOx microbolometer, 640 x 512 resolution, and 30 Hz full frame rate. The total project area was approx. 65,000m². During an additional flight, UAS-based lidar data was also collected for orthorectification of the thermal images with Pix4DMapper and to create a DEM of the area for higher accuracy video frame reprojection. Our research concluded that the ideal time to collect data in this region was shortly after spring snow melt when the ground was thawing, and groundwater flow levels were above average.

SfM for Thermal Index Maps

Completing SfM mapping from thermal imagery has the advantage that the produced orthorectified thermal index map can be used in Geographic Information System (GIS) software to correlate areas of increased thermal index (i.e., temperature) with slope, as seepage typically occurs where groundwater zones intersect the faces of slopes (Winter, et al., 1998).

Figure 3 shows contour lines of the ground surface overlaid on an SfM-generated thermal index map created from the data collected on May 7, 2020, shortly after snow melt. The thermal imagery was collected over the course of multiple UAS flights totaling 4 hours in duration from an altitude of 121m above ground level (AGL) resulting in an average Ground Sample Distance (GSD) of 16.9 cm/pixel.

There is a distinct temperature increase noticeable near the top of the riverbank as identified in Figure 3, but it is difficult to confidently delineate where the seepage exists using only the thermal index map and contours. This is primarily due to the lower resolution of the input thermal imagery and the color blending applied to each pixel as part of the SfM orthorectification process. Because of the color blending, other objects with elevated temperatures in relation to the ground, such as trees, contribute to the elevated index values surrounding them and falsely represent the elevated ground temperatures.

Our experience reveals that thermal mapping using SfM has several limitations. Groundwater seepage faces are commonly composed of homogeneous earth with similar geological properties and/or permeability characteristics that heats and cools at similar rates resulting in low thermal contrast. This low thermal contrast in turn results in featureless imagery which can lead to SfM key point generation failure. SfM software developers have thermal data collection recommendations including 90% front and side overlap, low flight speeds of 2-3 m/s, using a gimballed camera, and flying higher to assist key point matching (Pix4D, 2019; Pix4D, 2018a; Pix4D, 2018b). However, by following these guidelines challenges arise due to the volume of image data from acquiring imagery with high overlap. To reduce data volume the solution is to fly higher, but this reduces the image resolution. Flying at higher altitudes increases the volume of atmosphere between the ground and the sensor, resulting in thermal energy loss due to atmospheric attenuation (Infrared Training Center, 2019). Flying at very slow speeds increases image quality by reducing motion blur but contributes to the impractical data acquisition and processing limitations of UAS mapping.

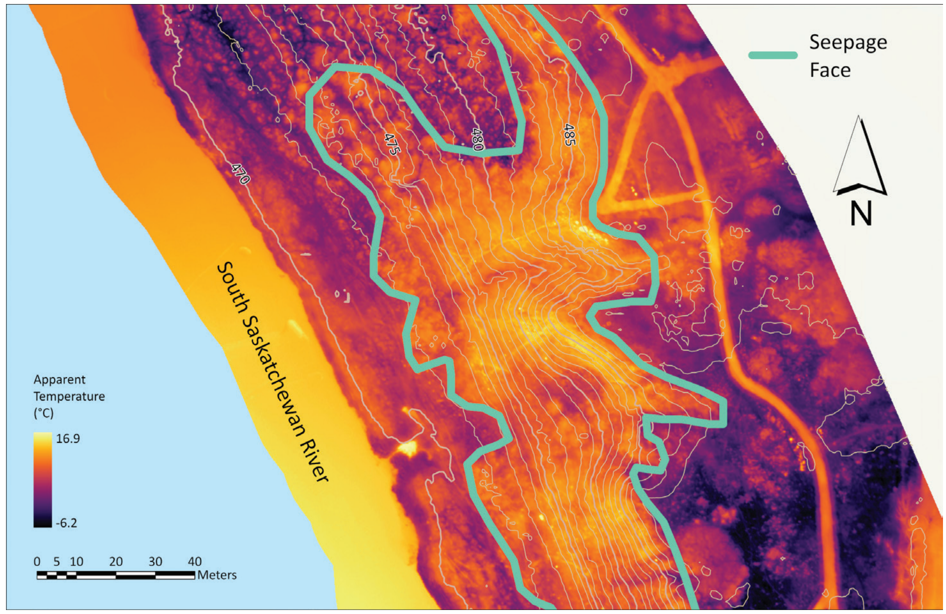

Figure 3: Thermal index map with elevated temperature on riverbank slopes. The contour interval is 1m. Date of data collection: May 7, 2020.

Another issue with SfM-based thermal mapping is the inconsistency of input data due to the loss of thermal energy over time. On larger projects that require multiple UAS flights and span several hours in duration, the data collected at the beginning of the acquisition period may have different thermal energy than the data collected near the end of the period over the same geographical area. In addition to all the above noted problems, thermal cameras onboard UAS will typically automatically adjust their measurable temperature range throughout the flight depending on the thermal energy that reaches the sensor. This is synonymous with collecting color imagery while adjusting the ISO light sensitivity setting significantly throughout acquisition. The resultant imagery can be difficult to process within SfM software in order to produce meaningful mapping products.

> *FMV is similar to Augmented Reality in that it combines real-world video data with georeferenced digital data such as point, polyline, and area features. Contour lines can be used to assist with the visualization of elevation change during FMV video review to identify temperature changes in areas of slope change.*

FMV for Identifying Groundwater Seepage

In addition to the high-altitude UAS flights, a single lower-altitude flight (45m AGL) was performed over the known seepage locations in order to investigate the practicality of using close-range thermal video for identifying groundwater seepage. This reduction in altitude subsequently increased the image resolution and reduced the volume of atmosphere between the thermal camera and the ground. This in turn resulted in an improved level of discernable temperature difference between the seepage faces and the surrounding ground. In order to georeference the features of interest identified within the thermal video, tests were conducted using FMV. FMV refers to a video file which has been combined with geospatial metadata to make the video file geospatially aware (Esri, n.d.). FMV is similar to Augmented Reality in that it combines real-world video data with georeferenced digital data such as point, polyline, and area features. Contour lines can be used to assist with the visualization of elevation change during FMV video review to identify temperature changes in areas of slope change.

To create a thermal index map with accurate absolute temperature values for each pixel, thermographic imagery collected with a radiometric camera needs to be corrected for emissivity and bias (Abdullah & Turek, 2021). This procedure presents challenges for FMV. However, in the case of locating seepage faces, apparent temperature differences are sufficient due to its qualitative nature (Harvey, et al., 2019). The non-disruptive nature of low-altitude UAS flights in comparison to using occupied aircraft, along with the suitability of using apparent temperature differences, favors the use of FMV from UAS for identifying and mapping groundwater seepage faces.

Site specific variables such as (but not limited to) geology, terrain, thermal characteristics, and slope aspect may dictate that FMV for groundwater seepage mapping be used in conjunction or at least supported by more conventional forms of terrain analysis (such as aerial photography analysis). Possible correlation between these variables and the findings of the FMV mapping and thermal imaging data may be drawn such that analysis can reliably map potential groundwater seepage areas.

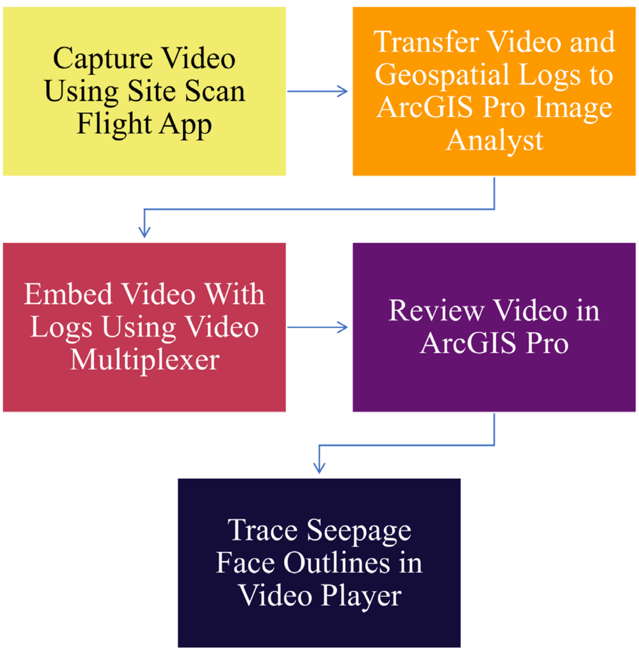

Figure 4: FMV Flow Chart (ArcGIS, 2020).

To create FMV, video data, along with position and orientation metadata of the UAS and gimbal orientation stored in geospatial flight logs created by Esri's Site Scan Flight app software, is combined using the Video Multiplexer tool within ArcGIS Pro. Areas of temperature change representing seepage can then be manually digitized to create vector feature classes, directly from the video frame within the Video Player similarly to how the area was manually digitized using the thermal index map as shown in Figures 3 and 5. The area of traced groundwater seepage in Figure 5 appears to coincide with the outcropping of more permeable soil deposits which may promote groundwater flow.

Another useful tool is the Frame Export tool which projects a single video frame onto the Esri map. Figure 5 shows an FMV frame that was overlaid onto the ArcGIS map view with the Frame Export tool.

Using ArcGIS Pro, the FMV can be displayed and a line feature displaying the UAS position during the flight will be shown in the map view (red parallel lines in Figure 6), as well as the position of where the video frame was recorded and the projected outline of the video frame on the ground. Feature classes that appear in the map or scene view can be displayed in the video frame, such as contours, cadastral boundaries, or manually digitized features by enabling the "Display Features" function. Such ability to view contours in the video frame assists reviewers in visually correlating changes in slope to the seepage faces. It also functions to ensure that all identified areas of interest within the video have been delineated. Once the FMV review has been completed, the feature classes can be easily exported as vector features for downstream GIS and CAD visualization and analysis.

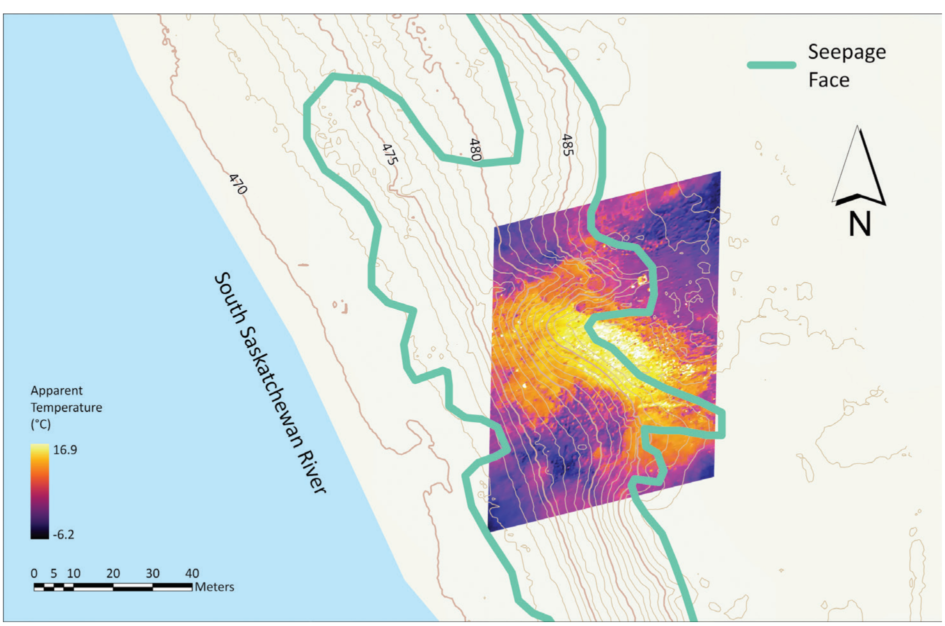

Figure 5: FMV Frame Export showing seepage face locations overlaid with contours – see the comments for Figure 3. Date of data collection: April 24, 2021.

In summary, there are many benefits to using FMV. It allows for reduced UAS flying height and distance from the sensor to the ground, reducing the effects of wind and other atmospheric conditions (e.g., humidity) within the thermal data. As a result, the FMV data are of more detail and higher resolution, and there is less thermal energy loss between the sensor and the ground. Parallel flight lines can be flown further apart as the high overlap for successful SfM processing is not required. The camera can be pointed in a nadir direction to reduce oblique distortion, and linear corridors can be mapped in a single pass, which is not successful when using SfM-based thermal mapping.

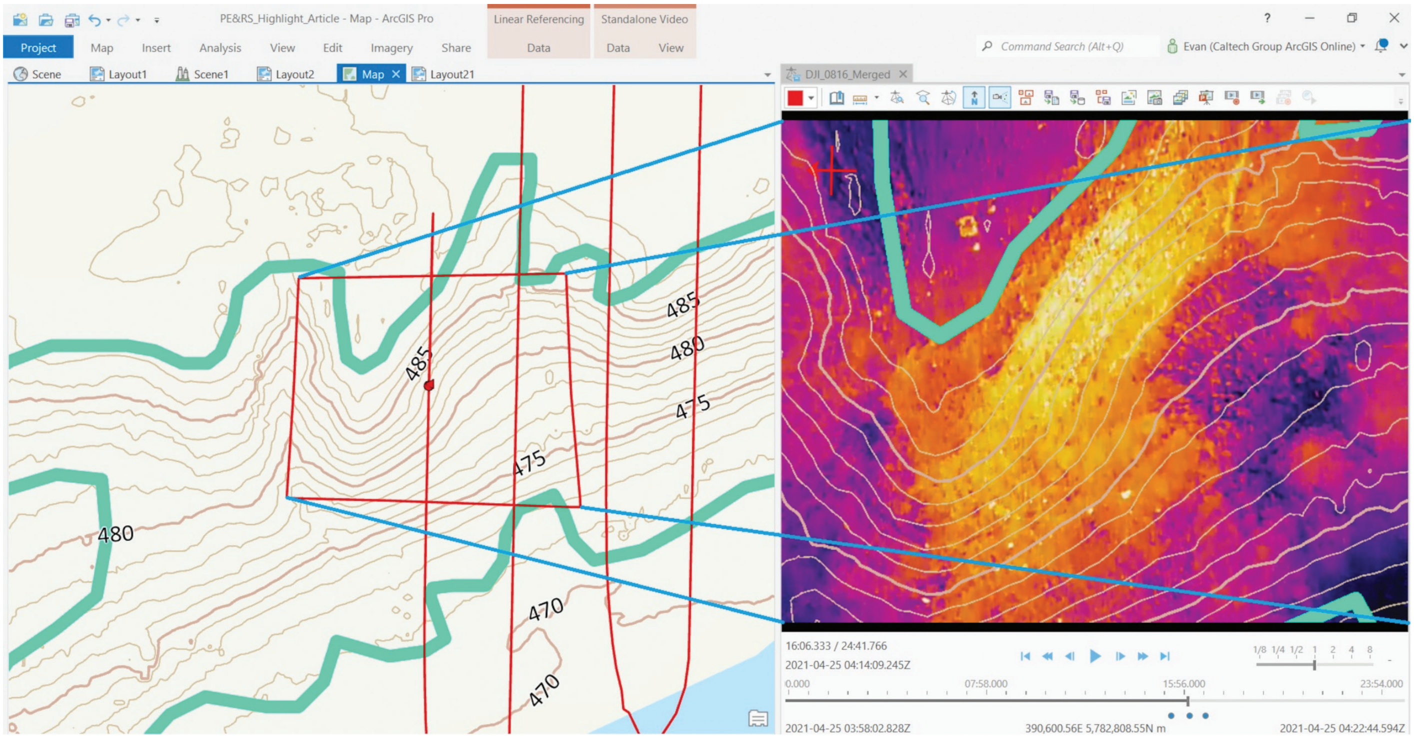

Figure 6: FMV Review in Esri's ArcGIS Pro Identifying Groundwater Seepage Face.

Although video files are typically large in size, the thermal video data collected over the research area was only 25% of the total size of the still thermal imagery collected. The total data collection time for the thermal video data was 40 mins, compared to 4 hours for still thermal imagery. Because the thermal data is collected faster, there will be less temperature variation from the beginning to the end of data collection. FMV data collection using UAS can be completed with high temporal frequency and in conjunction with aerial photography during sunlight to identify correlations. Lastly, groundwater seepage faces can still be identified in areas with reduced thermal contrast using FMV.

Similar to image interpretation of aerial photography (i.e., stereoscopic images), interpretation of FMV videos is required in order to identify and evaluate possible groundwater seepage areas. Misinterpretation of groundwater seepage due to vegetation cover and other land-use issues while using FMV increases without a fundamental understanding of the terrain.

> *"In summary, there are many benefits to using FMV."*

Future studies are to incorporate geology as a variable as it relates to thermographic mapping of potential groundwater seepage areas. Geology, specifically the physical characteristics of a soil or rock have influence over the thermal characteristics that will develop within a particular soil or rock. Heat transfer within a soil (other than conduction) may only be a factor in more permeable soils where groundwater flow is apparent (The Canadian Geotechnical Society, 2006).

The Future of FMV for Groundwater Seepage

One of the current trends in UAS industry is the integration of network connectivity for near real-time data transfer of imagery and video. Presently, some systems, such as the Freefly Systems Astro UAS, offer real-time viewing of data from several sensors including the Workswell WIRIS Pro or Flir Duo Pro R radiometric thermal cameras via the Auterion Suite. This allows for analysts to remotely view the thermal imagery from a live video dashboard and identify potential areas of interest to be further investigated while the UAS pilots are still in the field. The real-time data is not FMV, as it is not multiplexed with the position and orientation data streaming from the UAS and gimbal sensors. With the present ability to stream high-resolution video data to a remote viewer in real-time, it is perceivable that in the future it may be possible to perform the multiplexing of the video data and the position and orientation data for real-time FMV.

References

Abdullah, Q. & Turek, N., 2021. Thermal Imagery for Building and Utilities Owners. *Photogrammetric Engineering & Remote Sensing*, October, 87(10), pp. 689-696.

Alberta Environment, 2022. *Seepage Management & Internal Erosion Mitigation and Repair in Water Dams*, s.l.: Alberta Environment.

ArcGIS, 2020. *Accurate Geospatial Intelligence from Drone Imagery with Esri & DJI*. https://www.youtube.com/watch?v=eiC_K5bnJXY&t=2104s. [Accessed 29 April 2022].

Budhu, M. & Gobin, R., 1996. Slope Instability from Ground-Water Seepage. *Journal of Hydralic Engineering, July*. pp. 415-417.

Christiansen, E. A., 1992. Pleistocene stratigraphy of the Saskatoon area, Saskatchewan, Canada: an update. *Canadian Journal of Earth Sciences*, August, 29(8), pp. 1767 - 1778.

Esri, n.d. *Introduction to Full Motion Video*. https://pro.arcgis.com/en/pro-app/latest/help/analysis/image-analyst/introduction-to-full-motion-video-in-arcgis-pro.htm. [Accessed 28 April 2022].

Harvey, M. C. et al., 2019. Evaluation of Stream and Wetland Restoration Using UAS-Based Thermal Infrared Mapping. *Water*, July.Volume 11.

Infrared Training Center, 2019. *sUAS Level 1 Thermography Certification Course Manual*. Nashua(NH): Infrared Training Center.

Mollard, J. D. & Janes, J. R., 1984. *Airphoto interpretation and the Canadian landscape. Hull* (Quebec): Energy, Mines and Resources Canada.

Ozotta, O., 2021. Mapping Groundwater Seepage in a Fen Using Thermal Imaging. *Geosciences*, 11(29).

Pix4D, 2018a. *Processing thermal images*. https://support.pix4d.com/hc/en-us/articles/360000173463-Processing-thermal-images#label10. [Accessed 7 March 2022].

Pix4D, 2018b. *Thermal Image Capture Altitude Recommendation*. https://community.pix4d.com/t/thermal-image-capture-altitude-recommendation/7563. [Accessed 28 April 2022].

Pix4D, 2019. *Step 1. Before Starting a Project > 1. Designing the Image Acquisition Plan > a. Selecting the Image Acquisition Plan Type*. https://support.pix4d.com/hc/en-us/articles/202557459-Step-1-Before-Starting-a-Project-1-Designing-the-Image-Acquisition-Plan-a-Selecting-the-Image-Acquisition-Plan-Type#Thermal. [Accessed 7 March 2022].

Scudeler, C., Paniconi, D. & Putti, M., 2017. Examination of the seepage face boundary condition in subsurface and coupled surface/subsurface hydrological models. *Water Resources Research*, 3 March, 53(3), pp. 1799-1819.

The Canadian Geotechnical Society, 2006. C*anadian Foundation Engineering Manual. 4 ed*. s.l.:The Canadian Geotechnical Society.

USGS, n.d. *How Do Hydrologists Locate Groundwater?*. https://www.usgs.gov/special-topics/water-science-school/science/how-do-hydrologists-locate-groundwater#:~:text=As%20a%20first%20step%20in,openings%20to%20carry%20water%20underground. [Accessed 15 February 2021].

Winter, T., Harvey, J., Franke, O. & Alley, W., 1998. *Groundwater and Surface Water: A Single Resource Circular 1139*. Denver(CO): US Geological Survey.

Author(s)

Greg Stamnes, AScT, CMS-UAS, Saskatoon, SK, Canada. Greg Stamnes is a geospatial consultant that specializes in aerial and terrestrial mobile mapping, static terrestrial laser scanning, and mapping with UAS. With education relating to geomatics, GIS, and UAS, Greg is also an ITC level I-certified thermographer. When not working or studying Greg enjoys spending time with his 2 daughters and wife.

Alexander Hill, B.Sc., P.Geo., P.L.Eng., Calgary, AB, Canada. Alexander is a geohazard specialist with SNC-Lavalin with skills and experience in terrain mapping and geohazard identification and assessment within Canada and the UK. Alexander specializes in the evaluation of geohazards as they relate to linear infrastructure. Alexander is also a keen kayaker and trail walker when not at work.

Ryan Brazeal, Ph.D., P.Eng., PMP, Moose Jaw, SK, Canada. Ryan Brazeal is a geospatial scientist, innovator, and founder of the Open Mobile Mapping System (OpenMMS). In his spare time, he enjoys developing STEM-based projects for kids.

GIS

Tips & Tricks

Al Karlin, Ph.D. CMS-L, GISP

Getting your bearings in GIS?

In the September 2022 issue of *PE&RS*, this column asked "Which Way is Up?", discussed three definitions of "North", and provided tips on how to symbolize each on your map. This month's tip focuses on a similar issue, how to calculate the bearing (i.e., compass direction) of a line.

As with "North", there are several ways to define a "bearing." In navigation and GIS-mapping, a bearing is the horizontal angle, measured in degrees, between the direction of an object and another object, or between that object and that of "true" (i.e. celestial) north. The "absolute bearing" refers to the angle, measured in degrees, between magnetic north (i.e. the magnetic bearing) and an object, while the "relative bearing" refers to the angle, again, measured in degrees, between a craft's forward direction and the location of another object. Bearings are frequently referred to as "azimuths" which can be measured in degrees clockwise from "north" as geodetic (from celestial north), magnetic (measured from magnetic north) astronomic (from the south) or assumed azimuths. So, when reporting bearings (or azimuths) it is always a good idea to specify which is being reported. For additional information, https://theconstructor.org/surveying/azimuths-bearings-surveying-difference-determination/38494/, is a good general reference.

While calculating a bearing in an Esri GIS system seems like it should be a simple matter, the bearing is not one of the properties that is recorded in the standard line-attribute table. Furthermore, the bearing is also not one of the seven geometric features of a line that can be calculated by the "Calculate Geometry" function in the linetable field functions. Then, to make matters even more complex, when displaying or calculating a bearing in ArcGIS Desktop, the bearing is reported counterclockwise from East but calculated by the Add Geometry Attributes script as clockwise from North! So, here are some tips for getting your bearings.

In ArcGIS Desktop

Method 1—Interactive when editing/creating a line feature without point snapping – When in an editing session and creating a line feature, start the line, and move the cursor to the end-point. Before clicking the end-point, right-click on the mouse or use the key combination Crtl-A to reveal the "Direction …" of the line as in Figure 1. The Direction… window will display the bearing as in Figure 2. IMPORTANT NOTE: This "direction" is measured counterclockwise from the EAST (East=0, North=90, West =180, South=270) so to derive the compass bearing, you may want to adjust the value to North. In this case (Figure 2), the reported bearing of 27.2269º, is converted to the compass direction 62.7731º from North.

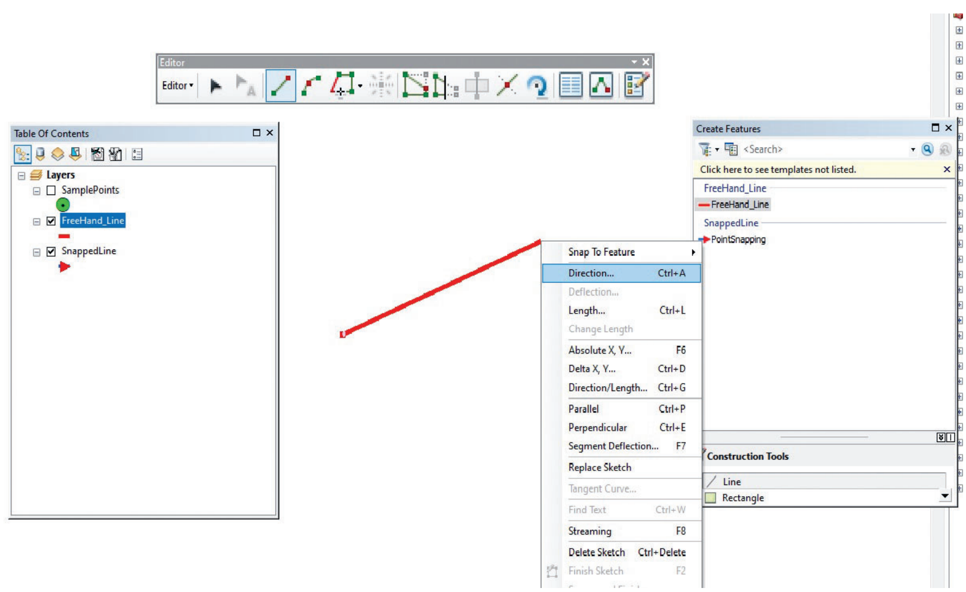

Figure 1. Using the key combination Ctrl-A (or right-mouse clicking) on the end-node of a freehand drawn line feature to start the Properties menu, then selecting the Direction… property.

Photogrammetric Engineering & Remote Sensing
Vol. 88, No. 12, December 2022, pp. 753-755.
0099-1112/22/753-755

doi: 10.14358/PERS.88.12.753

Method 2—Interactive when **editing/creating a line feature with feature snapping**. When in an editing session and constructing line features by snapping to points, the direction of any segment can be revealed as in Method 1. After snapping to the node, use the Ctrl-A sequence to show the direction. Again, the direction is measured counterclockwise from East. So, in this example (Figure 3), the reported bearing of 158.9755° is converted to 291.0245° from North.

Method 3— Using the Add Geometry Attributes script from ArcToolbox to **add the bearing to a line feature class**. Finally, with ArcGIS 10.8, there is an "Add Geometry Attributes" script in the Data Management Tools | Features Toolset that will add additional geometric attributes, including the bearing, to line feature classes (and/or shapefiles). In the example below, I added three lines to the SnappedLine feature class. Opening the Add Geometry Attributes tool (Figure 4) and check the desired attributes, indicate the linear units and Coordinate Reference System; running the tool will result in those attributes being added to the feature class table (Figure 5). Of course, the direction of the line is From_Node toward To-Node BUT the BEARING is reported from CELESTIAL NORTH!

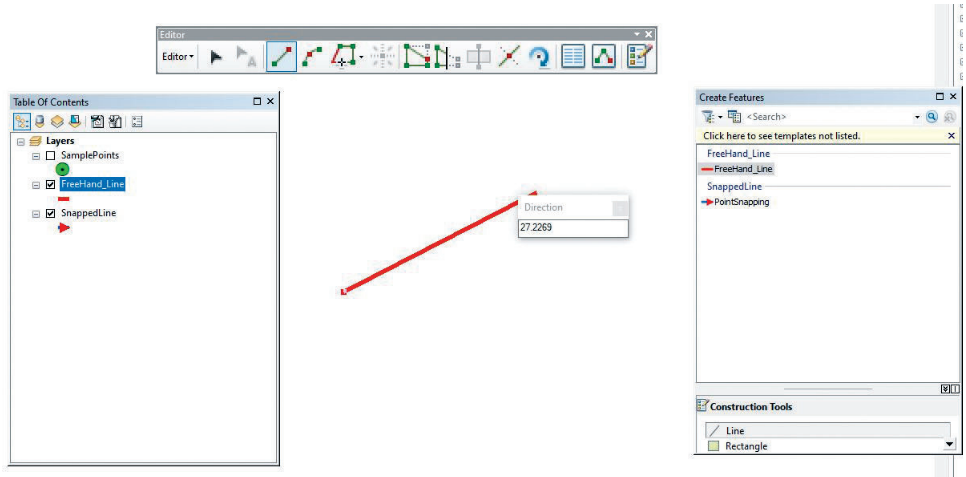

Figure 2. The Direction Window showing the bearing of the line feature. Note: this angle is computed counterclockwise from East.

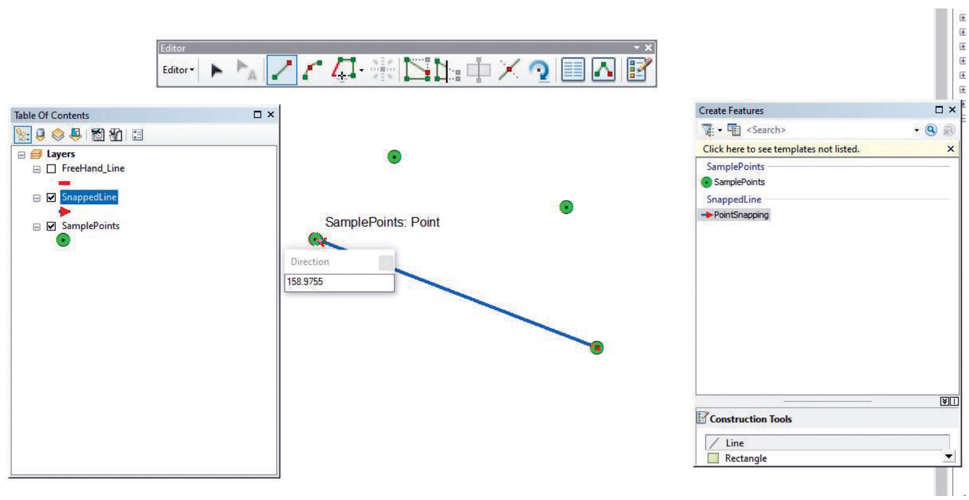

Figure 3. Using the key combination Ctrl-A after snapping a line feature to an end-point to show the Direction window. Again, note that the Direction is reported from East.

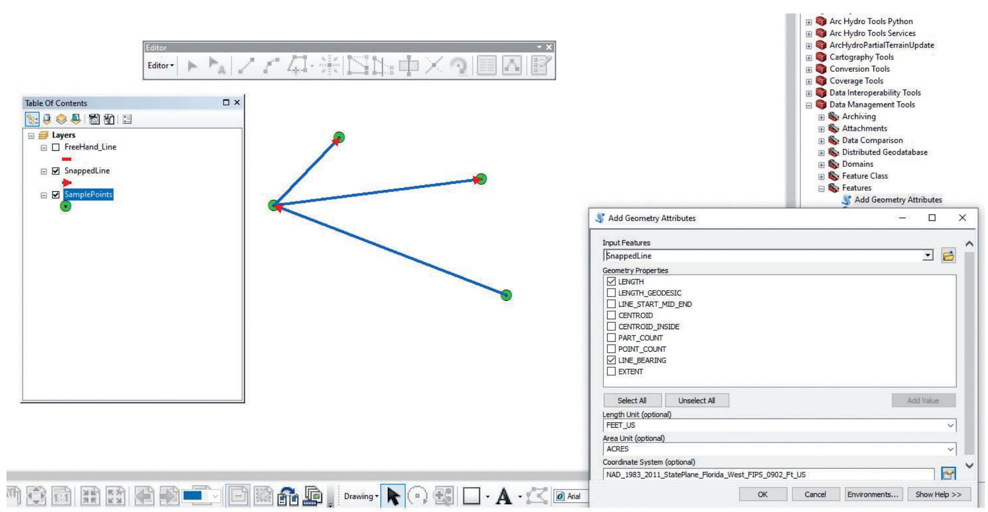

Figure 4. Using the Add Geometry Attribute script found in the Data Management Tools | Features toolset and choosing to add the LENGTH and LINE_BEARING attributes to the SnappedLine feature class.

In ArcGIS Pro

The same interactive and tabular methods described for ArcGIS Desktop also work in ArcGIS Pro. The only difference is that the interactive methods now give you options (Figure 6. drop down arrow) of displaying the direction as NAz (North=True Azimuth), SAz (South = Astronomic Azimuth), P (Polar Azimuth), or QB (Quadrant Bearing). The Add Geometry Attributes tool is again found in the Data Management Tools | Features Toolset.

While not as straight-forward as a user might hope, determining the direction of a line or a line feature class is not that challenging once you get your bearings.

Send your questions, comments, and tips to GISTT@ASPRS.org.

Al Karlin, Ph.D., CMS-L, GISP is with Dewberry's Geospatial and Technology Services group in Tampa, FL. As a senior geospatial scientist, Al works with all aspects of Lidar, remote sensing, photogrammetry, and GIS-related projects. He also teaches beginning map making at the University of Tampa.

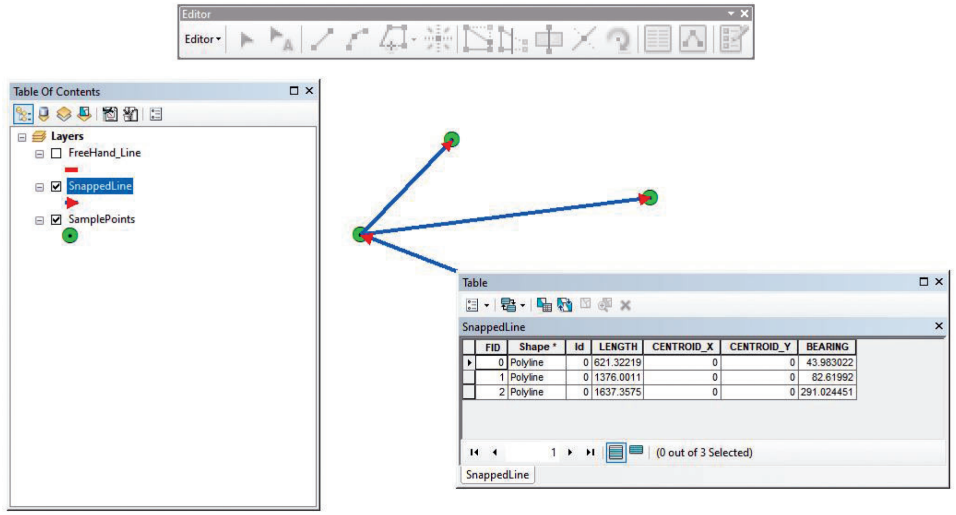

FID	Shape *	Id	LENGTH	CENTROID_X	CENTROID_Y	BEARING
0	Polyline	0	621.32219	0	0	43.983022
1	Polyline	0	1376.0011	0	0	82.61992
2	Polyline	0	1637.3575	0	0	291.024451

Figure 5. The resulting feature attribute table after running the Add Geometry Attributes script. Note that the script added the CENTROID_X and CENTROID_Y field but did not calculate these values. Use "Calculate Geometry" to populate these fields. Also note that the BEARING values are reported from Celestial North!

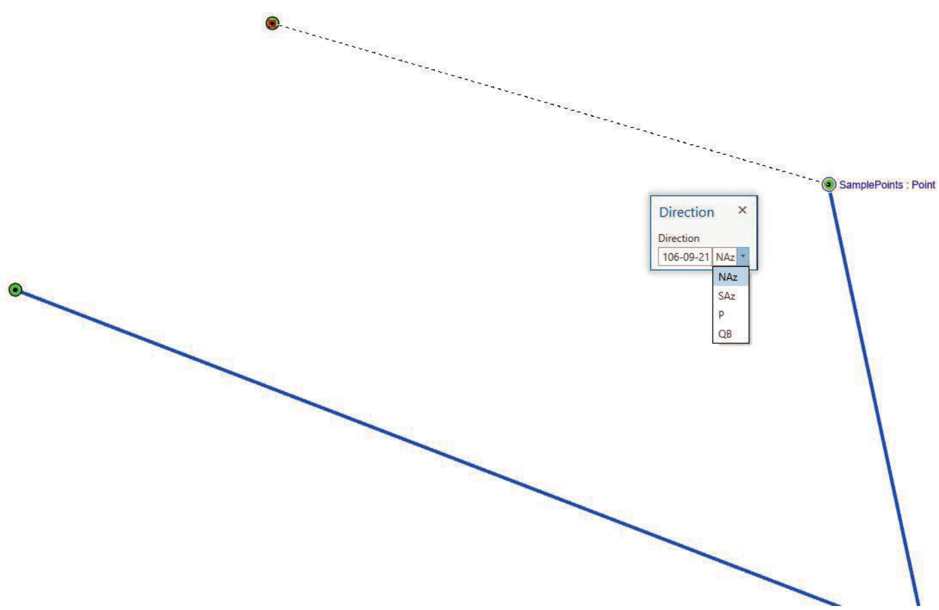

Figure 6. In ArcGIS Pro, the interactive (Ctrl-A) Direction property provides optional reports for the bearing.

Mike Zoltek

The Impact of Certification/Licensure on Your Geospatial Career

Certification and Licensure directly impacts all practicing Geospatial professionals. However, it is a challenge in the current environment of fast-paced technological advancement to ensure those providing geospatial products and services are both capable and qualified to fulfill the needs of clients and customers. How do users of current and future technologies choose providers? How do they know that the product or service they are receiving will have a reasonable expectation for correctness and completeness? Certification and licensure have provided traditional paths for demonstrating knowledge and technical proficiency. "Certification" has historically been used to evaluate and ensure technical competence, while "licensure" has traditionally been the mandate of legislation (at both the state and federal level) premised by the need to ***"protect the public health, safety and welfare."*** Traditional requirements to become licensed include a combination of a defined level of formal education, experience, and testing.

Licensing has long been a requirement for doctors, lawyers, engineers, and land surveyors. As technologies have advanced, many states have realized the need to license photogrammetrists, providers of a variety of geospatial information (e.g., GIS practitioners), and those providing lidar data collection and processing services (a.k.a. topographic mapping products & services). As more states enact legislation relating to existing and new geospatial products and services, it is difficult for practicing professionals, state and national organizations, and the public to keep up with changes to existing rules and regulations. The American Society for Photogrammetry and Remote Sensing (ASPRS), as the leading scientific organization representing the photogrammetry and remote sensing profession, provides a resource to readily access this new and changing information through its published maps and variety of geospatial mapping products and services.[1] The "Licensure Maps and Regulations" website1 shown in Figure 1 provides metadata on State Surveying Regulations; State Licensure Map for GIS Services, Lidar and Topographic Products, Georeferenced Imagery and Authoritative Imagery, respectively, with references to each state's existing Regulations, Board Websites, Individual State Regulations and also provides a Composite State Regulation Document.

Currently there are twenty-one (21) states that have existing regulations relating to georeferenced imagery products and services, thirty-three (33) that have existing regulations relating to authoritative imagery products and services, forty-seven (47) states with regulations relating to topographic mapping-related products and services (which includes lidar services), and fifteen (15) states with existing regulations relating to GIS-related products and services.

Having a list of the current regulations is just the first step. Every provider of a potentially regulated product or service should be aware of and understand how specific state regulations impact their practice because each state regulates geospatial products and services differently. Products or services that are regulated in one state may not be regulated the same way (or at all) in another state. For the practicing geospatial professional (whether it be an engineer, surveyor, photogrammetrist, GISP or UAS pilot), knowledge of an individual area of practice is essential. Knowledge of state, local and possibly even federal regulations are required to properly perform services, provide products, and fulfill contractual requirements for clients.

As mentioned earlier, the geospatial industry is constantly going through rapid changes as advancements are made in measurement technologies and capture platforms. The lower cost and easy access to measurement technologies (e.g. imagery and lidar systems) combined with the new and readily available low-cost UAS have allowed for an unprecedented opportunity for both individuals and firms to get into the business of collecting data to support an ever-expanding variety of geospatial products and services. The field-to-finish (e.g., black box) software solutions supporting these new advancements allow for virtually anyone to provide products that appear to be the same as those that have historically been created utilizing validated geospatial methodologies.

At almost every major geospatial conference in the last few years, the "big" giveaway is a UAS. Does this mean that

[1]http://www.asprs.org/PPD-Division/Licensure-Maps-and-Regulations.html

Photogrammetric Engineering & Remote Sensing
Vol. 88, No. 12, December 2022, pp. 757-759.
0099-1112/22/757-759

doi: 10.14358/PERS.88.12.757

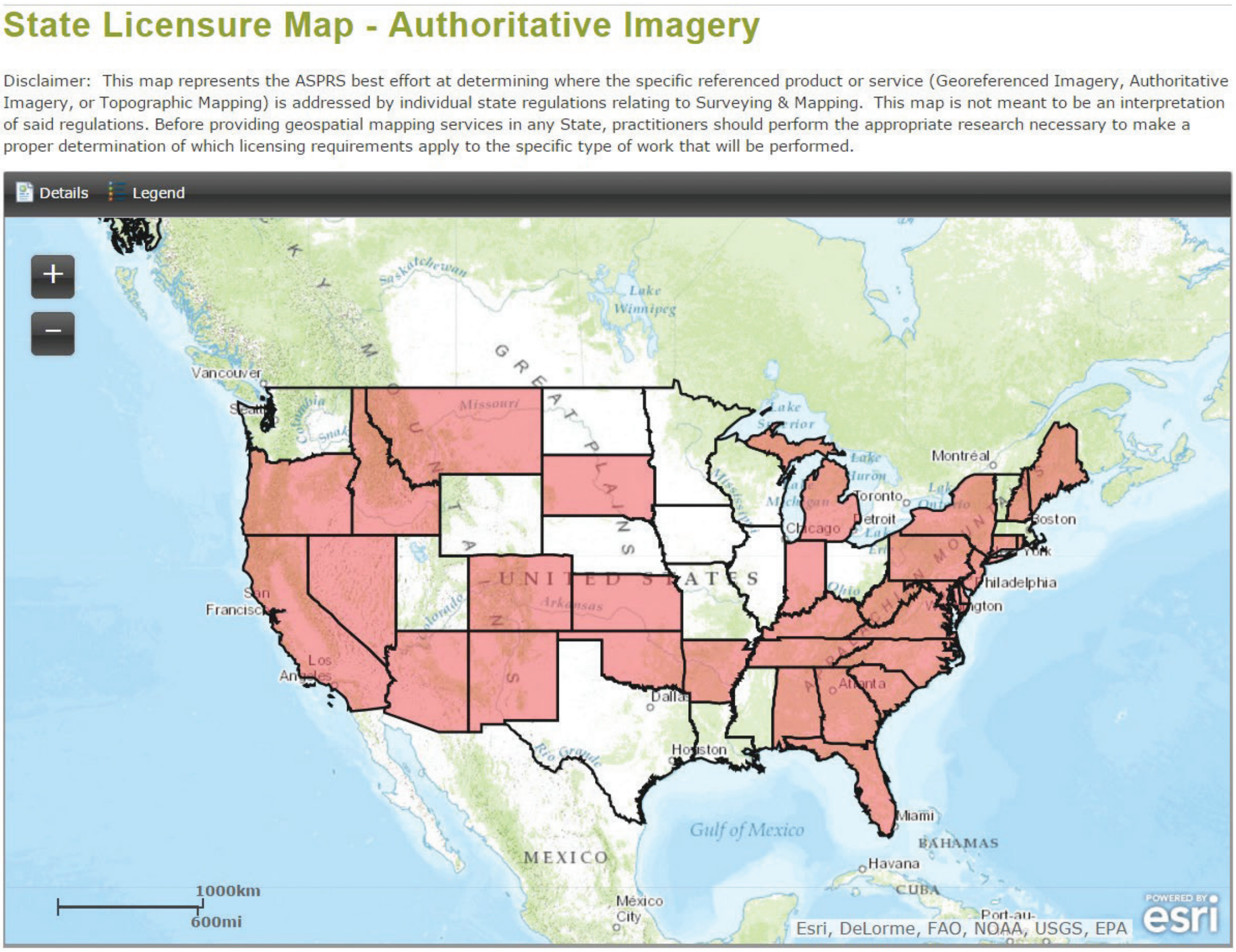

Figure 1. From the "Licensure Maps and Regulations" in ASPRS Profession Practice Division: The State Licensure Map—Authoritative Imagery

anyone can use this technology to create and provide services to the public? Various states have proposed or enacted legislation that clearly states otherwise. Over the last few years, there have been regulations enacted by over twenty (20) states regarding UAS use.[2] The 2012 FAA enacted its Section 333 exemption policies,[3] and in November 2015 published its report, Unmanned Aircraft Systems (UAS) Registration Task Force (RTF) Aviation Rulemaking Committee (ARC) Task Force Recommendations Final Report,[4] in which it recommended that all UAS flying within U.S. airspace that have a mass of more than 250 grams (~0.55 pounds) be registered with the FAA.

The new legislation and rules are examples of how the landscape of certification and licensure is being affected by new technologies. Rapid changes in technology require us to continually ask the questions as to which geospatial products and services should require certification and which should require licensure. How will the current and future practice of certified and/or licensed professional practice be affected by these changes? The answers to these questions will define the future of all practicing geospatial professionals, whether they are engineers, surveyors, photogrammetrists, GISPs or UAS pilots.

To help facilitate appropriate regulations regarding certification and licensure, the ASPRS Professional Practice Division (PPD)[5] proactively engages states to discuss potential legis-

---

[2] *Current Unmanned Aircraft State Law Landscape*, by National Conference of State Legislators, November 25, 2015: http://www.ncsl.org/research/transportation/current-unmanned-aircraft-state-law-landscape.aspx

[3] *FAA Modernization and Reform Act*, of 2012, HR 658, by Federal Aviation Administration (FAA): https://www.faa.gov/uas/media/Sec_331_336_UAS.pdf and https://www.faa.gov/uas/legislative_programs/section_333/

[4] *Unmanned Aircraft Systems (UAS) Registration Task Force (RTF) Aviation Rulemaking Committee (ARC) Task Force Recommendations Final Report* November 21, 2015: https://www.faa.gov/uas/publications/media/RTFARCFinalReport_11-21-15.pdf

[5] http://www.asprs.org/Divisions/Professional-Practice-Division.html

[6] http://www.asprs.org/Divisions/Unmanned-Autonomous-Systems-Division.html

lative changes and assists states by reviewing current and proposed state licensure laws related to geospatial products and services. ASPRS PPD works with individual states to ensure that there is an available licensure path for appropriately educated and experienced professionals. ASPRS PPD also actively engages other national geospatial organizations (URISA, NSPS, MAPPS, etc.) to coordinate efforts of regulation review and interpretation, with the goal of appropriately advising legislative bodies on legislation relating to existing and future geospatial products and services. Additionally, ASPRS has formed its Unmanned Aerial Systems Division whose "objectives include outreach and education, liaising with UAS-interested parties outside the Society, development and promotion of standards and best practices, establishment of calibration and validation sites, and credentialing and certification activities…"[6]

While it is in the best interest of every practicing professional to be active in their individual national organizations, it is incumbent upon every practicing geospatial professional to stay up to date on the specific rules affecting their practice. This combination of these two items is the only way to ensure the appropriate implementation of certification and licensing requirements, while also ensuring the protection of the health, safety, and welfare of the public in our fast-paced geospatial world.

Author

Mike Zoltek is a land surveyor, photogrammetrist, and GIS professional with over 30 years of geospatial experience. As the National Geospatial Program Director at GPI Geospatial, Inc (GPI), Mike is responsible providing operational oversight while leading new geospatial initiatives for the firm. A licensed surveyor who holds active surveying/photogrammetry registrations in 26 states, Mike has extensive experience with a wide variety of geospatial services, ranging from boundary surveying to remote sensing services. Mike currently serves as a member of Florida's State Board of Professional surveyors & Mappers, is the chair of the ASPRS Evaluation for Certification Committee and serves on the ASPRS Standards Committee that is currently updating the ASPRS standards for geospatial products and services. Mike has presented numerous technical seminars at universities and community colleges, as well as at industry conferences, and as has served as expert witness in boundary litigation cases in the state of Florida.

The book *"The Essentials of SAR, A Conceptual View of Synthetic Aperture Radar and its Remarkable Capabilities"* is authored by Thomas P. Ager. Mr. Ager is an expert in the SAR (Synthetic Aperture Radar) industry. He provides SAR consulting and teaching services.

This book comprises a total of six parts that the author refers to as "Apertures" – each with several chapters. SAR is not unknown to the imaging industry. As the author stated in the Foreword of the book: "SAR is well known as an imaging technology that can see through clouds and darkness, but SAR remains a confusing and enigmatic sensor for many. Its image is naturally different from the optical views wired into the human visual system, and SAR has an electrical engineering heritage that is incomprehensible to most ordinary people." Adroitly, the author explains the SAR technology to make it a clear and appealing subject for users who do not have advanced degrees in electrical engineering.

The author highlights the values of SAR in the preface, from which the reader can learn and appreciate important characteristics of SAR technology. These characteristics are "cloud penetration", "day and night coverage", "high resolution independent of distance", "variable resolution and coverage", "accurate geolocation", and "coherent illumination and many products".

Aperture, reviews basic sensor design and explains microwave sensors and how a simple form of radar imaging works. He then addresses how these processes enable for SAR imaging thoroughly providing the formulas behind the science. The author provides various examples of SAR theories behind those image phenomenon.

Aperture Three provides an overview of SAR products so readers can learn how SAR products are produced. Aperture Four explains how SAR geolocation works and gives examples of geodetic level accuracy derived from a commercial spaceborne SAR satellite. The author reviews how a radar pulse works and how the echoes, and the sources of all SAR data behave when they arrive at the antenna while also explains why SAR images sometimes have ghostly misplaced features in Aperture Five. The final Aperture describes the SAR's future by reviewing examples of ease, speed and automation in SAR processing of how to access the harmonic depth of SAR by replacing orderable, individual products. The book also includes appendices to discuss further considerations of SAR while reader can also find a list of symbols and acronyms, and an Index in the book.

The book provides basic concepts and explains the practices of SAR technology in great detail. The book is well organized so the reader can follow the contents in a logical

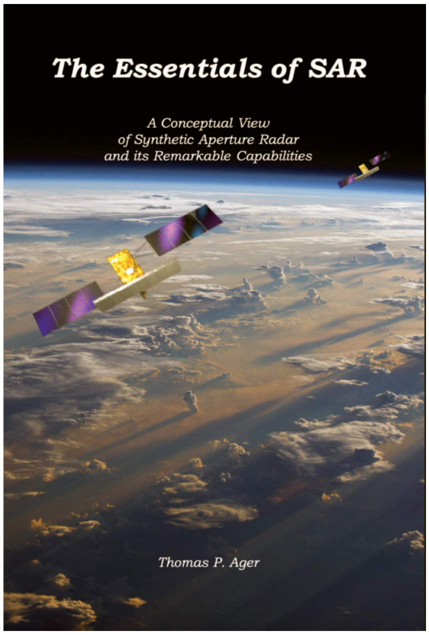

The Essentials of SAR, A Conceptual View of Synthetic Aperture Radar and its Remarkable Capabilities

By Thomas P. Ager

Independently published, August 2021. 309 pp. ISBN-13 979-8512864487, ASIN B09CGKTLZV.

Reviewed by Connie Krampf, CP, CMS/GIS-LIS, Senior Geospatial Analyst, DroneView Technologies LLC, Bloomfield Hills, Michigan

way with ease. The book could be used as a text book for undergraduates or graduates who study remote sensing science. It also can be a valuable reference for remote sensing professionals.

SAR is a serious technical topic. To help the reader understand the subject more easily and to keep the discussion interesting, the author uses tables, charts and related pictures, some of them even cartoon-like illustrations, to present the theories of SAR. The book uses some mathematical formulas, stories and even music and

continued on page 764

Photogrammetric Engineering & Remote Sensing
Vol. 88, No. 12, December 2022, pp. 760, 764.
0099-1112/22/760, 764

doi: 10.14358/PERS.88.12.760

Grids & Datums
NEW ZEALAND

BY Clifford J. Mugnier, CP, CMS, FASPRS

The Grids & Datums column has completed an exploration of every country on the Earth. For those who did not get to enjoy this world tour the first time, *PE&RS* is reprinting prior articles from the column. This month's article on New Zealand was originally printed in 2005 but contains updates to their coordinate system since then.

New Zealand is the southernmost extent of colonization by Polynesians. It is believed that the colonization took place in at least two major waves, the first of which is thought to have occurred around 950 AD and the second around 1200 to 1400 AD. The first group consisted of hunters who depended for survival on the flightless "Moa" bird that is now extinct. The second Polynesian group was more agrarian, and archeological evidence indicates that the two cultural groups overlapped. Abel Janszoon Tasman, a captain for the Dutch East Indies Company, was the first European to discover the Maori of New Zealand. He sighted a "large land, uplifted high" near the modern day town of Hokitika on the West Coast of South Island on 13 December 1642. He sailed northwards to a bay which he subsequently named Murderer's Bay (now renamed Golden Bay), after four of his men were attacked and killed by Maori warriors. The entire region was once thought by Tasman to be part of Tierra del Fuego, so he named it Staten Landt. Soon after Tasman's voyage it was discovered that it was not Staten Landt, and it was renamed Nieuw Zeeland.

In the late 1800s, modern surveying had begun. Captain James Cook, son of a Scottish migrant farmhand, was apprenticed to a Quaker ship owner and he learned his trade in the difficult waters of the North Sea. He studied mathematics at night during off seasons, and later in Nova Scotia he mastered surveying with the plane table and alidade. He was chosen to command a scientific voyage to the Pacific Ocean. He was commissioned Lieutenant prior to his first survey and he was promoted to the rank of Captain before his third and last survey voyage. On the first voyage (1768-1771), his charter was to first go to Tahiti and observe the transit of Venus. These observations were to be later combined with other simultaneous observations (by others) in different locations in order to establish the magnitude of one astronomical unit (AU), which is defined as the mean distance of the Earth from the Sun. (See "The Republic of Mauritius," *PE&RS*, February 1999). After making these observations, Cook was to sail south and discover or not the supposed Antipodes or great Southern Continent. The East Coast of

Photogrammetric Engineering & Remote Sensing
Vol. 88, No. 12, December 2022, pp. 761-764.
0099-1112/22/761-764

doi: 10.14358/PERS.88.12.761

North Island was sighted 07 October 1769. Cook circumnavigated North and South Island while taking almost continual observations. It took six months to produce an "astonishing" chart of New Zealand that mapped 2400 miles of coastline. On this first voyage, Cook did not sail with John Harrison's chronometer but instead used Dr. Maskelyne's Lunar Almanac, published in 1767, which he used to fix his longitudes. However, Cook did use Harrison's chronometer on his two subsequent voyages (1772-1775, 1776-1780); he verified his longitudes to within 30 minutes. Cook's chart was used for the next 100 years as the settlement of New Zealand began. Thanks to Peggy Haeger for the above research done in the late 1990s for a graduate-level course on coordinate systems that I used to teach at the University of New Orleans.

According to L.P Lee in *First-order Geodetic Triangulation of New Zealand 1909-49* and *1973-74*, "In New Zealand, as indeed in many a similar young country, … the settlement survey proceeded well in advance of the triangulation, which should have controlled it. Even the triangulations were done in reverse order, the smaller networks being observed first, the larger and more accurate networks later. Thus, the procedure has been one of successive approximations, and each stage has led to a revision or recalculation of the work done earlier."

The first use of triangulation to control local surveys was by Felton Mathew, the first Surveyor-General in 1840-41; the limited area covered was near Auckland. In 1849 another small triangulation was begun near Christchurch. Both of these were superseded by more accurate surveys. In 1852, six Provincial Governments were formed to administer New Zealand, and later this increased to nine provinces; each of which had its own survey department. (A special department of the General Government conducted Surveys of native Maori lands). Henry Jackson based his land surveys on triangulation in Wellington Province beginning in 1865. The principal sections were in Wellington, Wairarapa, and Rangitikei covering the three districts where settlements were located, and each section was erected upon its own baseline, with several check bases included for verification.

The specifications for surveying the New Zealand public lands with steel tapes originated with experiments on the Thames gold-fields in 1869. The specifications were finally written to require steel tapes only (no chains) by James McKerrow in 1886, which preceded both the Swedish Jäderin steel wire apparatus in 1887, and the U.S. Coast & Geodetic Survey steel tapes in 1891!

"In the Province of Otago a control net of triangulation was not used, but a uniform system to govern the orientation of surveys was introduced by J.T. Thomson in 1856. The Province was divided into for large districts called 'meridional circuits.' Within each circuit an initial station was selected and true meridian was determined by astronomical observation. Bearings, but not distances, were carried outwards by traverse from the initial station to the boundaries of the circuit, following the chief valleys suitable for settlement. Points on these traverses were called 'geodesic stations,' and were usually from 15 to 25 km apart, providing a series of reference points by which any survey within the meridional circuit could be oriented in terms of the meridian of the initial station. Any further control was merely local, being based upon a small triangulation net extending only over the region where is was immediately required, so that a large number of independent triangulations came to be distributed throughout the settled area of the Province. Each such triangulation was regarded as the control for an area around it called a 'survey district,' and each meridional circuit was eventually divided into many such districts, often irregular in shape: although the later additions tended to be bounded by lines parallel to and perpendicular to the meridian of the initial station. Local surveys could be coordinated with reference to the geodetic stations within a survey district."

The original datum for New Zealand was the Mt. Cook Datum of 1883, located in the city of Wellington.

Thompson eventually adopted the meridional circuit system for all of New Zealand in 1877 as modeled by his original system earlier used in Otago. A total of 28 Meridional Circuits were established: nine in the North Island and 19 in the South Island. Those Meridional Circuits with their original initial origins are: Mt. Eden/Mt. Eden, Bay of Plenty/Maketu, Poverty Bay/Patutahi, Taranaki/Huirangi, Tuhirangi/Thuirangi, Hawkes Bay/Hawkes Bay, Wanganui/Mt. Stewart, Wairarapa/Opaki, Wellington/Mt. Cook, Collingwood/Parapara, Nelson/Botanical Hill, Karamea/Karamea, Marlborough/Goulter Hill, Buller/Buller Initial, Grey/Grey Initial, Amuri/Isolated Hill, Hokitika/Hokitika Initial, Okarito/Abut Head, Mt. Pleasant/Mt. Pleasant, Gawler/Gawler Downs, Jacksons Bay/Mt. Eleanor, Timaru/Mt. Horrible, Lindis Peak/Lindis Peak Initial, Mt. Nicholas/Mt. Nicholas, Mt. York/Mt. York, Observation Point/Observation Point, North Taieri/North Taieri, and Bluff/Observation Spot. Computations on these meridional circuits were performed on the plane with the point of origin being the initial point. With the geodetic coordinates known for each initial point, the survey computations were equivalent to using the Polyhedric projection, which is the same as the Local Space Rectangular, commonly used in computational photogrammetry.

In 1901 a new secondary triangulation was started in order to bring all the different nets of triangles into harmony in the Wellington and Taranaki districts. The North Island geodetic triangulation of 1921-1938 started actual field observations in 1923 and continued until being suspended during the Great Depression of the early 1930s. It resumed in 1936. The South Island geodetic triangulation of 1938-1942 started with the observations across Cook Strait in a quadrilateral with one line measuring 120 km from Papatahi to Attempt Hill. Final fieldwork was observed from 1947-1949 including baseline-measuring equipment obtained on loan from Tanganyika (now Tanzania), which was used for three South Island bases. In 1948, 12 LaPlace stations were observed with time signals transmitted from Dominion Observatory especially for this purpose. When the computations were completed, the "New Zealand Geodetic Datum 1949" (NZGD49) was established where the initial station of origin was: Papatahi Trig Station Φ_o = 41º 19´ 08.9000˝ S, Λ_o = 175º 02´ 51.0000˝ E of Greenwich, azimuth to Kapiti No. 2 α_o = 347º 55´ 02.500˝, and the ellipsoid of reference is the International 1924 where a = 6,378,388 m and $^1/_f$ = 297. Papatahi is a centrally situated station of the main net and one of the corner stations of the subsidiary net containing Kelburn. The values of deflection of the vertical for the north-south component at 65 latitude stations and deflection of the vertical for the east-west component at 39 azimuth stations from the first adjustment were known, and the latitude and azimuth at Papatahi were chosen so as to make the means of these differences equal to zero. The longitude adopted for Papatahi was that derived from Kelburn. The stations were coordinated on the National Grids, each island being on an independent Transverse Mercator projection, which had been selected by H.E. Walshe just before WWII. The New Zealand North Island Belt Latitude of Origin φ_o = 39° S, Central Meridian, λ_o = 175° 30´ E, Scale Factor at Origin, m_o = unity, False Northing = 400,000 yards, False Easting = 300,000 yards where 1 foot = 0.304799735. The New Zealand South Island Belt Latitude of Origin, φ_o = 44° S, Central Meridian, λ_o = 171° 30´ E, Scale Factor at Origin, m_o = unity, False Northing = 500,000 yards, False Easting = 500,000 yards. No further first-order work was contemplated for about 25 years, and in 1972-1974, some reobservation and extension was done with theodolites and Geodimeter Model 8 electronic distance meters.

When the metrication of surveys was begun in 1973, a one-projection coordinate system was adopted for topographic maps (the New Zealand Map Grid), but for cadastral surveying it was decided to retain the meridional circuit systems but the Polyhedric coordinates were replaced by Transverse Mercator coordinates referred to the old origins.

In August 1998, "Land Information New Zealand" (LINZ) approved the adoption and implementation of a new geocentric datum, New Zealand Geodetic Datum 2000 (NZGD2000). The new coordinates of points changed by approximately 200 meters relative to the old datum, NZGD49. A one-projection coordinate system was adopted for 1:50,000 scale and 1:250,000 scale topographic maps (the New Zealand Transverse Mercator 2000) that replaces the NZMG. The NZTM2000 Latitude of Origin, φ_o = 0°, Central Meridian, λ_o = 171° E, Scale Factor at Origin, m_o = 0.9996, False Northing = 10,000,000 meters, and False Easting = 1,600,000 meters. For cadastral surveys in terms of NZGD2000 the 28 new meridional circuits replace the existing circuits, which were in terms of NZGD49. The new circuits are referred to as "<name> Circuit 2000," to distinguish them from the old circuits. The origins of latitude and longitude of the NZGD2000 circuit projections are almost the same as their NZGD49 equivalents being rounded down to the nearest arc second. The central meridian scale factors at origin of the NZGD2000 circuit projections are the same as those of their NZGD49 equivalents. The false origin coordinates of NZGD2000 circuit projections are 100 km greater then their NZGD49 equivalents, being 800 km N and 400 km E. This is to reduce the risk of confusion between the NZGD2000 and NZGD49 projections. The NZGD2000 circuit projections are based on the GRS80 ellipsoid of revolution where a = 6,378,137 m and $^1/_f$ = 298.257222101. The SI standard for the meter has been adopted. The NZGD2000 circuit projections have a scale factor at origin of unity except for North Taieri 2000 (0.99996) and Mt. Eden 2000 (0.9999).

The Circuit Parameters are as follows: Mount Eden 2000 - φ_o = 36º 52´ 47˝ S, λ_o = 174° 45´ 51˝ E, m_o = 0.9999; Bay of Plenty 2000 - φ_o = 37º 45´ 40˝ S, λ_o = 176° 27´ 58˝ E, m_o = 1.0; Poverty Bay 2000 - φ_o = 38º 37´ 28˝ S, λ_o = 177° 53´ 08˝ E, m_o = 1.0; Hawkes Bay 2000 - φ_o = 39º 39´ 03˝ S, λ_o = 176° 40´ 25˝ E, m_o = 1.0; Taranaki 2000 – φ_o = 39º 08´ 08˝ S, λ_o = 174° 13´ 40˝ E, m_o = 1.0; Tuhirangi 2000 - φ_o = 39º 30´ 44˝ S, λ_o = 175° 38´ 24˝ E, m_o = 1.0; Wanganui 2000 - φ_o = 40º 14´ 31˝ S, λ_o = 175° 29´ 17˝ E, m_o = 1.0; Wairarapa 2000 - φ_o = 40º 55´ 31˝ S, λ_o = 175° 38´ 50˝ E, m_o = 1.0; Wellington 2000 - φ_o = 41º 18´ 04˝ S, λ_o = 174° 46´ 35˝ E, m_o = 1.0; Collingwood 2000 - φ_o = 40º 42´ 53˝ S, λ_o = 172° 40´ 19˝ E, m_o = 1.0; Nelson 2000 - φ_o = 41º 16´ 28˝ S, λ_o = 173° 17´ 57˝ E, m_o = 1.0; Karamea 2000 - φ_o = 41º 17´ 23˝ S, λ_o = 172° 06´ 32˝ E, m_o = 1.0; Buller 2000 - φ_o = 41º 48´ 38˝ S, λ_o = 171° 34´ 52˝ E, m_o = 1.0; Grey 2000 - φ_o = 42º 20´ 01˝ S, λ_o = 171° 32´ 59˝ E, m_o = 1.0; Amuri 2000 - φ_o = 42º 41´ 20˝ S, λ_o = 173° 00´ 36˝ E, m_o = 1.0; Marlborough 2000 - φ_o = 41º 32´ 40˝ S, λ_o = 173° 48´ 07˝ E, m_o = 1.0; Hokitika 2000 - φ_o = 42º 53´ 10˝ S, λ_o = 170° 58´ 47˝ E, m_o = 1.0; Okarito 2000 - φ_o = 43º 06´ 36˝ S, λ_o = 170° 15´ 39˝ E, m_o = 1.0; Jacksons Bay 2000 - φ_o = 43º 58´ 40˝ S, λ_o = 168° 36´ 22˝ E, m_o = 1.0; Mount Pleasant 2000 - φ_o = 43º 35´ 26˝ S, λ_o = 172° 43´ 37˝ E, m_o = 1.0; Gawler 2000 – φ_o = 43º 44´ 55˝ S, λ_o = 171° 21´ 38˝ E, m_o = 1.0; Timaru 2000 - φ_o = 44º 24´ 07˝ S, λ_o = 171° 03´ 26˝ E, m_o = 1.0; Lindis Peak 2000 - φ_o = 44º 44´ 06˝ S, λ_o = 169° 28´ 03˝ E, m_o = 1.0; Mount Nicholas 2000 - φ_o = 45º 07´ 58˝ S,

λ_o = 168° 23´ 55˝ E, m_o = 1.0; Mount York 2000 - φ_o = 45º 33´ 49˝ S, λ_o = 167° 44´ 19˝ E, m_o = 1.0; Observation Point 2000 - φ_o = 45º 48´ 58˝ S, λ_o = 170° 37´ 42˝ E, m_o = 1.0; North Taieri 2000 - φ_o = 45º 51´ 41˝ S, λ_o = 170° 16´ 57˝ E, m_o = 0.99996; and Bluff 2000 - φ_o = 46º 36´ 00˝ S, λ_o = 168° 20´ 34˝ E, m_o = 1.0.

Thanks to Graeme Blick of LINZ for a copy of L.P. Lee's monograph on the history of geodetic triangulation in New Zealand and to Mal Jones of Perth Australia for his continuing generous help.

New Zealand Update

"The geodetic system has been and will continue to be upgraded and enhanced. Often this is in response to increased accuracy requirements, but it is also to meet the needs of an increasing range of users. Accurate positioning is increasingly carried out by non-surveyors, often in a fully automated manner. LINZ must therefore consider how the geodetic system can support the needs of applications such as Intelligent Transportation Systems (ITS), indoor positioning and precision agriculture.

"From a user perspective, a geodetic system would ideally provide the highest levels of absolute and relative accuracy without changing coordinates. In a country such as New Zealand, these requirements are mutually exclusive. At the same time, the exploding use of GNSS-enabled technology providing ITRF coordinates through techniques such as precise point positioning (PPP) requires that LINZ provide greater support for the global reference frame.

"To support these diverse user needs LINZ is considering how to implement a two-frame system whereby both national and global datums are actively supported, with well-defined transformations between them (Donnelly et al. 2015). This would effectively be a formalization of existing practice. Applications such as cadastral surveying might continue to use NZGD2000, but other applications could then work directly in ITRF." *From Static to Dynamic Datums: 150 years of Geodetic Datums in New Zealand*, G. Blick & N. Donnelly, 2016. https://www.tandfonline.com/doi/full/10.1080/00288306.2015.1128451.

The contents of this column reflect the views of the author, who is responsible for the facts and accuracy of the data presented herein. The contents do not necessarily reflect the official views or policies of the American Society for Photogrammetry and Remote Sensing and/or the Louisiana State University Center for GeoInformatics (C^4G).

This column was previously published in *PE&RS*.

Book Review

continued from page 760

prose to illustrate technical principles. For example, he makes an analogy to Clapton's "Layla and other Love Songs" to demonstrate a point. He often takes into consideration the reader's perspective to help make technical concepts understandable to the new students. The viewer finds blue insert boxes at chapter endings throughout the book which are very interesting, informational, and fun to read. The author provides more information in those insert boxes to support the points of view presented in each chapter.

The book cover is well designed, the font size of the book makes for easy reading. The illustrations are well placed to keep the subject matter relevant to the chapter content. The print quality of the book is good for the most part, but some minor improvement might be possible. Some of the SAR images in the book could be better colorized and larger size of some image could better convey the author's messages. If used as a text book, the instructor of the course would have to invest his/her time to develop questions for homework for students since no homework exercises are provided in the book. Nevertheless, the book is highly recommended for the student of SAR technology or for the remote sensing professional who wants to enhance his/her knowledge of SAR.

THE ASPRS 2023 ANNUAL CONFERENCE WILL TAKE PLACE AT GEO WEEK IN DENVER, COLORADO

Geo Week showcases the increased integration between the built environment, advanced airborne/terrestrial technologies, and commercial 3D technologies.

The ASPRS Annual Conference will feature:

- 2-hour and 4-hour workshops will take place on Monday, February 13
- Technical sessions will take place on Tuesday, February 14 and Wednesday, February 15
- Awards and scholarships will be presented on Tuesday, February 14
- The annual business meeting and Installation of Officers will take place on Wednesday, February 15.

Details on the ASPRS Program will be announced on www.asprs.org and in the weekly newsletter. For additional information or questions, contact programs@asprs.org.

WWW.GEO-WEEK.COM WWW.ASPRS.ORG

NEW ASPRS MEMBERS

ASPRS would like to welcome the following new members!

Mark Allen
Richard Allen
Adam Arrington
Oluwatosin Oluyemisi Ayo
Golky Eduardo Barrios Quintana
Zeltis Peteris Beldavs
Cody Burmeister
Evan Zachary Clark
Nathan Eick
Nicholas Fulton
Christopher DL Howard
Scott Karlins
Robert Klau
Sai Charan Kukunoor
Shengjie Liu
Gilberto Maldonado
Dan Mason
Alexander McFadden
Sierra Melton
Corey Miller
David Moloney
Prof. Abdulkader Murad, Ph.D.
Mahmood Muttaqee
Mina Nada
Oren Ben Yair Nardi
Bret Okraski
Logan Pennington
Kristina Preucil, Student
Ian Ray
Johannes Riegl, Jr.
Constantine John Roros
Kyle Jacob Steen
Hashir Tanveer
Dilsad Unsal
Matt Viverito
Doug Woodruff
Betsy Young
Basnewende B. F. Zoungrana

FOR MORE INFORMATION ON ASPRS MEMBERSHIP, VISIT **HTTP://WWW.ASPRS.ORG/JOIN-NOW**

Call for *PE&RS* Special Issue Submissions

Innovative Methods for Geospatial Data using Remote Sensing and GIS

Internationally comparable data is a global need for managing resources, monitoring current trends and taking actions for sustainable living. Even though there has been a significant progress on geospatial data availability, extensive data gaps are still a major problem for general assessment and supervise the progress through the years. According to United Nations 2022 The Sustainable Development Goals Report, while health and energy sectors have the highest data available, limited data available for climate action.

The COVID-19 crisis has also shown that there are innovative data collection methods utilizing information and computer technologies. However, only 5% of the countries have benefit from remote sensing technologies to measure the impact of COVID-19. Additionally, novel approaches such as artificial intelligence should be used in conjunction with assessments to make sure they are put to use for critical situations.

The recent developments in remote sensing, geographic information systems and ICT have provided a wide accessibility to create geospatial data for various purposes. The proposed special issue focuses on *"Innovative Methods for Geospatial Data using Remote Sensing and GIS" for wide range of applications. This special issue aims to bring researchers to share knowledge and their expertise about innovative methods to contribute to fill data gaps around the world for a better future.*

The proposed special issue aims to contributes ASPRS's key mission on 'Simplify and promote the use of image-based geospatial technologies for the end-user', 'Promote collaboration between end users and geospatial experts to match data and technology to applications and solutions' and 'promote the transfer of geospatial data and information technology to developing nations' by providing innovative methods to create geospatial data using remote sensing and geographic information systems utilizing state-of-the-art developments and solutions.

Deadline for Manuscript Submission—July 1, 2023

Submit your Manuscript to http://asprs-pers.edmgr.com

Guest Editors

Dr. Tolga Bakirman, bakirman@yildiz.edu.tr , *Yildiz Technical University, Department of Geomatic Engineering*, Davutpasa Campus, 34220 Esenler-Istanbul/Turkey

Dr. George Arampatzis, garampatzis@pem.tuc.gr, *Technical University Crete, School of Production Engineering & Management*, 73100 Chania – Crete/Greece

Automatic Registration Method of Multi-Source Point Clouds Based on Building Facades Matching in Urban Scenes

Yumin Tan, Yanzhe Shi, Yunxin Li, and Bo Xu

Abstract
Both UAV photogrammetry and lidar have become common in deriving three-dimensional models of urban scenes, and each has its own advantages and disadvantages. However, the fusion of these multi-source data is still challenging, in which registration is one of the most important stages. In this paper, we propose a method of coarse point cloud registration which consists of two steps. The first step is to extract urban building facades in both an oblique photogrammetric point cloud and a lidar point cloud. The second step is to align the two point clouds using the extracted building facades. Object Vicinity Distribution Feature (Dijkman and Van Den Heuvel 2002) is introduced to describe the distribution of building facades and register the two heterologous point clouds. This method provides a good initial state for later refined registration process and is translation, rotation, and scale invariant. Experiment results show that the accuracy of this proposed automatic registration method is equivalent to the accuracy of manual registration with control points.

Introduction
Point cloud registration is to calculate the rigid transformation relationship between two sets of point cloud data, align the two sets of point cloud data, and construct a complete model. In many instances, there is a need to align point cloud data collected at different times from different platforms. For example, using well-registered lidar point clouds and optical images at the same time can easily improve measurement and interpretation accuracy(Campos-Taberner *et al.* 2016; Kwak *et al.* 2006).

There are two main stages for pairwise three-dimensional (3D) point cloud registration: (i) the coarse alignment and (ii) the refined alignment. The Iterative Closest Point (ICP) algorithm is currently the most widely used registration method. The algorithm can well register two point clouds together after multiple iterations (Besl and McKay 1992; Chen and Medioni 1992; Rusinkiewicz and Levoy 2001). For over two decades, many variants of the ICP algorithm have been developed. Gruen and Akca (2005) proposed an alternative to ICP referred to as "Least Squares 3D Surface Matching". This method gives the opportunity of matching arbitrarily oriented 3D surface patches and fully considers 3D geometry. Bae and Lichti (2008) developed the "Geometric Primitive ICP" method which uses normal vector information together with change in surface curvature for point cloud matching. It improved the precision of the estimated relative transformation parameters by as much as a factor of 5, which provides a window of opportunity to use this automated registration method in practical applications such as terrestrial surveying and deformation monitoring. Bouaziz *et al.* (2013) introduced "Sparse ICP" which is less sensitive to outliers than the classical ICP.

All these methods give meaningful results only if the pair of point clouds have already been coarsely co-registered. More importantly, the performance of these refined alignment methods depends on the quality of the coarse co-registration. Therefore, the coarse point cloud co-registration is a critical step to the final registration results. In this paper, we focus on addressing the initial coarse point cloud co-registration problem. We propose a method that uses specific objects, which can be segmented in the scene, to determine the transformation parameters. Specifically, in the urban scene, this object is determined to be the facade of buildings. By comparing the distribution of surrounding facades, we identify the corresponding facades in the matching, and calculate the similarity transformation matrix of the two point clouds. This method provides a good initial state for later refined registration process and is translation, rotation, and scale invariant.

Related Work
Automated Coarse Point Cloud Registration
Cross-source point cloud registration is very challenging because of the density difference, scale difference, partial overlap, and combination of considerable noise between point clouds. The existing 3D point cloud registration methods can be divided into two categories: (i) descriptor-based methods and (ii) non–descriptor-based methods. The main difference between the two methods is whether they rely on key point based descriptors to represent features.

Descriptor-Based Methods
Many traditional point cloud registration methods rely on the extraction of salient key points. Descriptors are formed by using various types of local neighborhood shape attributes of the point cloud. Similar descriptors on source and target point clouds can then be matched to find corresponding key points. Various three-dimensional point cloud descriptors have been developed, including Fast Point Feature Histograms (Rusu *et al.* 2009), Signature of Histograms of Orientations (Salti *et al.* 2014). When the source and target point clouds have a scale difference, these descriptors will fail during the feature matching process.

To overcome the difference of scale, some descriptors use local scale to define the local region used for descriptor generation. For example, the Scale Invariant Feature Transform (Lowe 2004) detector uses a "Difference of Gaussian" framework for estimating the local

Zhang Yan is with the School of Computer and Information Engineering, Tianjin Chengjian University, Tianjin, China, and the Tianjin Intelligent Elderly Care and Health Service Engineering Research Center, Tianjin, China.

Wang Xiangyu, Zhang Zhongwei, and Sun Yemei are with the School of Computer and Information Engineering, Tianjin Chengjian University, Tianjin, China (gucaszzw@163.com).

Liu Shudong is with the School of Computer and Information Engineering, Tianjin Chengjian University, Tianjin, China, and the Tianjin Intelligent Elderly Care and Health Service Engineering Research Center, Tianjin, China.

Contributed by Jan Dirk Wegner, April 11, 2022 (sent for review July 4, 2022; reviewed by Devrim Akca, Yongbo Wang).

Photogrammetric Engineering & Remote Sensing
Vol. 88, No. 12, December 2022, pp. 767–782.
0099-1112/22/767–782

doi: 10.14358/PERS.22-00069R3

scale. The three-dimensional extensions of scale-invariant feature transform (SIFT) (Flitton *et al.* 2010) and Speeded Up Robust Features (Knopp *et al.* 2010) are volume-based methods which use three-dimensional voxel representations instead of direct point cloud data. Four-Points Congruent Sets (4PCS) (Aiger *et al.* 2008) extracts all coplanar four-points sets from a 3D point set that are approximately congruent, under rigid transformation, to a given set of coplanar four-points. Based on this method, in order to drastically thin out the original point clouds while retaining characteristic features, K-4PCS (Theiler *et al.* 2014) resort to extracting 3D key points, it can better suit the characteristics of laser scans.

Because of the density difference and combination of considerable noise between heterogeneous point clouds, descriptor matching methods based on key points still require improvement.

Non–Descriptor-Based Methods

There are also descriptor-free methods that solve the coarse three-dimensional point cloud registration problem. These methods can be divided into three categories: geometry-based methods, optimization-based methods, and learning-based methods.

The main idea of the geometry-based method is to use geometric shape features, such as lines and planes, to register point clouds. Dijkman and Van Den Heuvel (2002) proposed a semi-automatic registration method based on least squares fitting of the parameters of cylinder and plane. Stamos and Leordeanu (2003) used both linear and planar features to align laser scans of buildings. Von Hansen (2006) extracted planes in point cloud collected by terrestrial laser scanning and search the corresponding planes. Parmehr (Shijie *et al.* 2016) used linear features extracted from point clouds to match Airborne Laser Scanning and images. Yang (Yang *et al.* 2016) used vertical linear features to segment point cloud and then formed a network by triangulating features. A hashing table was used to find matching source and target triangles. These frameworks do not cater for scale differences.

To overcome the cross-source challenges, some optimization-based methods are developed. The main idea of the optimization-based method is to design an optimization strategy to transform the registration problem. For example, the normal distributions transform (NDT) (Biber and Straßer 2003) is used. It sliced the 3D scans into two-dimensional (2D) layers, and then used the 2D NDT algorithm for registration, but only works when the scale is same. CSGM (Huang *et al.* 2016) converts the registration problem into a graph matching problem and estimate the transformation matrix by graph matching optimization. Huang *et al.* (2019) convert the registration problem into a tensor optimization problem and introduce high order constraints to correspondences searching. The advantage of optimization-based methods is that rigorous mathematical theories could guarantee their convergence. But the challenges are large computation cost and generalization performance on different data sets.

Because of the robust at feature extraction, deep neural network is used for registration. Deep closest point uses deep features to estimate correspondences and use singular value decomposition to calculate the transformation (Wang and Solomon 2015). Deep Gaussian Mixture Registration (DeepGMR) (Yuan *et al.* 2020) uses deep learning to calculate the correspondences between Gaussian models and points and optimize the transformation based on Gaussian Mixture Model optimization. Feature-Metric Registration (Huang *et al.* 2020) applies deep learning to extract global features and uses the Lukas-Kanade algorithm to minimize feature differences. Both the accuracy robustness and efficiency of learning-based methods are still required to improve further.

The method proposed in this paper overcomes the problem of different density and distribution of multi-sensor point clouds by extracting objects instead of key points. Building facade is chosen as a common target in urban scenes.

Building Facades Extraction

There are already several methods proposed to extract building facades: random sample consensus (RANSAC), Hough transform, region growing, deep learning, etc.

Raguram *et al.* (2013) added normal vector constraints to RANSAC algorithm in extracting three-dimensional patches. The randomness of the RANSAC algorithm may lead to false detection results, adding certain constraints to it can improve the robustness.

Hough transform is a method of detecting parameterized targets, which can identify different targets such as straight lines, spheres, and planes. Hulik *et al.* (2014) extracted planes by voting at sampling points. Similar to RANSAC, Hough transform also has errors in plane recognition.

Different from the above two methods based on statistics, region growing relies on the adjacency relationship between points and the similarity of related attributes to transfer and then grows into extracted planes. To improve efficiency, an octree structure is used to increase the efficiency of voxel region growth (Vo *et al.* 2015).

At present, deep network-based frameworks have been widely used in the of 2D image processing, but there are huge challenges in applying them in three-dimensional data processing. Point-Net (Qi *et al.* 2017) directly applies deep learning to unstructured point clouds to handle tasks such as classification and segmentation, while it does not consider the characteristics of its local area, and Point-Net++ (Qi *et al.* 2017) is its upgraded version. In view of the irregular and disordered point cloud characteristics, the Point-CNN (Li *et al.* 2018) performs well on many complex data sets, while it requires a lot of training data and will take a fairly long processing time.

Besides, Brie *et al.* (2016) obtained local surface sampling step by conducting a first order Taylor expansion of planar point coordinates. Wang *et al.* (2018) used image features and considered structural information at the same time in extracting building facade features. Zolanvari *et al.* (2018) proposed an improved slicing method in three-dimensional building segmentation and opening boundaries detection even on roofs. All the above methods have their advantages and limitations; there is still a lack of adaptive thresholding or segmentation method.

This paper presents a novel approach in extracting urban building facades from both lidar and oblique photogrammetric point clouds based on statistical characteristics of point clouds, and then the façade feature descriptor named Object Vicinity Distribution Feature (OVDF) is taken as the basis of point clouds registration.

In the section "Methodology", we introduce the principle and steps of the method, and give the mathematical expression of the feature descriptor. The main idea of this kind of descriptor is that around the corresponding object, the distribution of other objects should be similar. The descriptor is theoretically invariant to rotation, translation, and scaling, so it has good adaptability in registration between point clouds with large differences in initial state and scaling.

In the section "Experiment and Analysis", we design experiments to justify the effectiveness of the method. Sample transformation parameters (scale, transition, rotation) are used to transfer a single point cloud to create a new point cloud in a new coordinate system. Then, our method is used to register the transferred point cloud to the original one. Finally, using real data sets of the Dublin area, we performed whole-area and partially overlapping registration experiments.

In section the "Discussion and Conclusion", we discuss the experimental results and analyze the advantages and disadvantages of our method.

Methodology

We propose a RANSAC-based method for building facade extraction in urban point cloud. Then extracted facades from two point clouds are used for registration. The methodology consists of two stages: (i) building facade extraction in urban point clouds with a RANSAC-based method, and (ii) point cloud registration with the extracted facades based on OVDF. Figure 1 is an overview of the method.

Our primary contribution is the development of an automatic coarse registration approach for multi-source point clouds in urban scenes. Point cloud pairs from multiple sensors have different point densities and point distributions, which increases the vulnerability of many existing coarse registration algorithms. We solve this problem by searching for matches between objects instead of key points. In addition, the scale, as an additional unknown entity, increases the complexity of

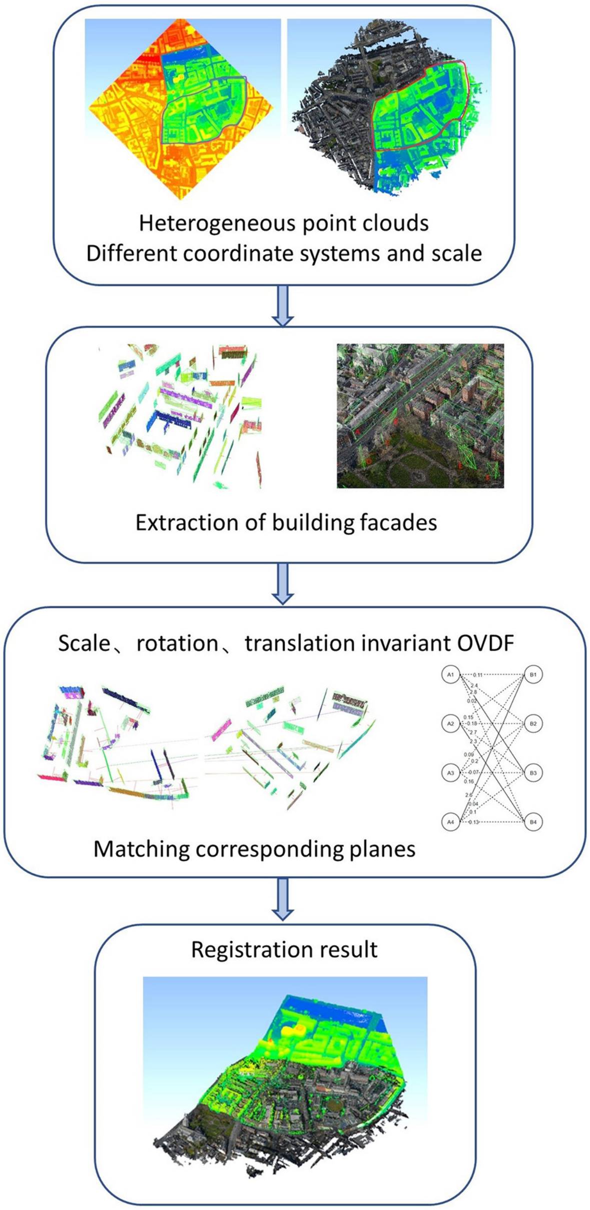

Figure 1. Overview of methodology.

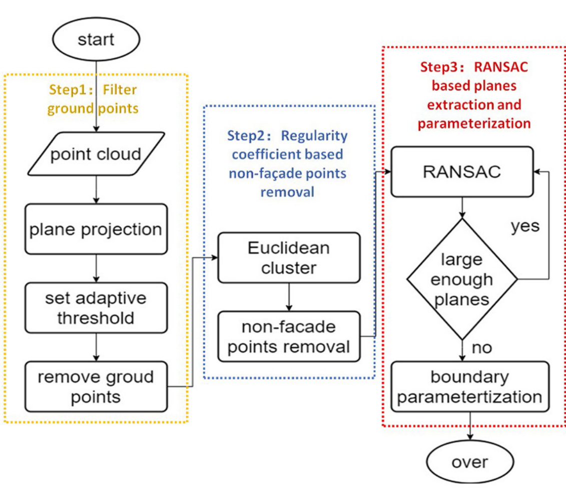

Figure 2. Framework of the proposed method in facades extraction.

matching algorithms, thus, we design the OVDF descriptor in this study so that all seven parameters in the 3D transformation matrix can be solved.

Extraction of Building Facades

The stage for building facades extraction comprises three main steps. The first step is to remove ground points, the second step is to remove non-facade points using a threshold called regularity coefficients, and the third step is to detect building facades with the RANSAC algorithm and boundary optimization. The framework is shown in Figure 2.

Ground Points Removal

Before extracting the building facades, it is necessary to remove irrelevant ground points. Filtering out ground points can reduce computational complexity and ensure that ground points will not be recognized as planes. In this paper, the building facades are assumed to be vertical, in which case the points of a facade will form a line after projected to a X-Y plane. Apparently, if all points in a point cloud are projected to the X-Y plane, where there are more projected points, a facade is more likely there. Therefore, the ground points could be removed by setting a proper threshold.

According to the above assumption, a raster can be obtained by projecting the point cloud to the plane. The gray value of a pixel in the raster represents the number of points that fall onto it, so we call this raster the plane density projection image. The pixel size of the raster depends on the density of the points in the point cloud data. The ground sampling distance, in this case, the ground distance between points, is the average distance among points.

Cumulative probability density can be calculated according to the gray histogram of the density projection image, as in Equation 1:

$$P(G) = P_g\{g < G\} \tag{1}$$

where G denotes the given gray value, g represents the variable of gray value, and P refers to the probability.

Generally, pixels corresponding to facade points have higher gray values, while ground points occupy much larger space. If a probability value is set as the threshold, the ground points could be easily segmented.

Figure 3 displays the process of ground points removal. According to the gray value of pixels, a curve similar to that in Figure 3d can be made. Figure 3d illustrates the way to compute the optimal threshold. By connecting the beginning and the end points of the curve, the point on the curve which is the farthest from the line can be found. This point is the inflection point, the gray value of which is taken as the threshold. By setting the gray value of all pixels greater than the threshold to 255, and those of all other pixels to 0, a binary image of point density projection is obtained as in Figure 3c, the final result of ground points removal is shown in Figure 3e.

Regularity Coefficient-Based Non-Facade Points Removal

In the previous step, ground points have been filtered out from the point cloud. In this step, the non-facade points are to be removed from the point cloud. First, all extracted points are grouped into several parts, which may represent a tree, a streetlamp, a facade, etc., based on Euclidean clustering, in which Euclidean distance is used for clustering-decision making. For a certain point P in space, K-dimensional tree-based, nearest neighbor search algorithm is applied to find k points closest to point P, and those points whose distance are less than a predetermined distance threshold is clustered into set Q. If the number of elements in Q does not increase, the entire clustering process ends. Otherwise, other points in set Q must be selected and the above process is repeated until the number of elements in Q does not increase. The distance threshold can be adapted according to the density of the point cloud. In this paper, it is taken as the average minimum distance between all points in the point cloud plus three times the standard deviation of the minimum distance.

The next step is to remove non-facade parts in order to avoid misdetecting other objects as facades. For each point, an auto-covariance matrix is calculated from Equation 2:

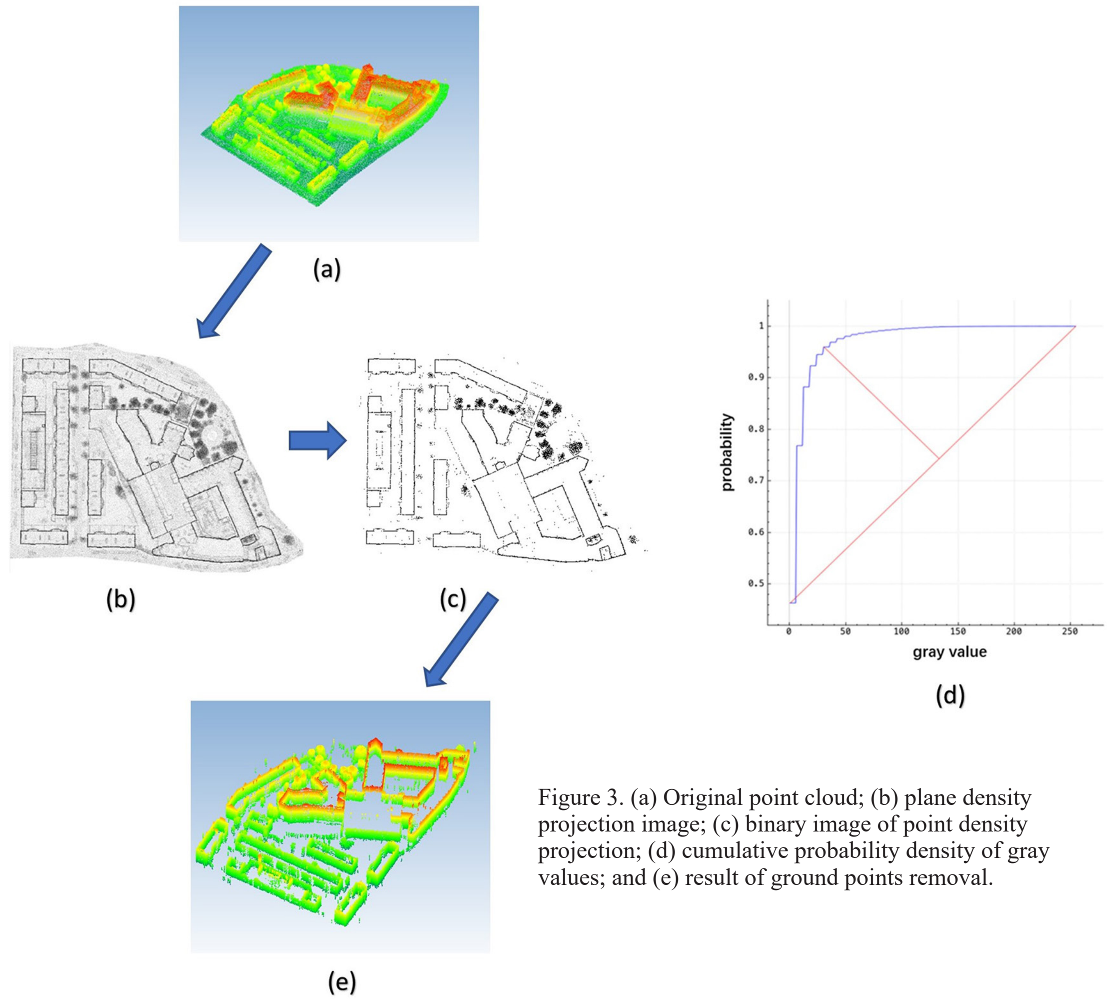

Figure 3. (a) Original point cloud; (b) plane density projection image; (c) binary image of point density projection; (d) cumulative probability density of gray values; and (e) result of ground points removal.

$$\Sigma = \sum_{i=1}^{m} \left(p_i - \bar{p}\right)\left(p_i - \bar{p}\right)^T \quad (2)$$

where p_i represents each point in the neighborhood; $\bar{p}$ refers to the mean value of all the points in the neighborhood, and m denotes the total number of points in the neighborhood According to eigenvalue decomposition of the auto-covariance matrix, its characteristics can be decomposed as in Equation 3:

$$\begin{cases} \Sigma e_1 = \lambda_1 e_1 \\ \Sigma e_2 = \lambda_2 e_2 \\ \Sigma e_3 = \lambda_3 e_3 \end{cases} \quad (3)$$

where λ_1, λ_2, λ_3 are the eigenvalues in descending order, e_1, e_2, and e_3 denote the eigenvectors with e_3 corresponding to local normal vector of a point.

We assume that for a relatively regular building facade, the normal vector of a point is not much different from the normal vector of its neighboring point, and they face almost the same direction. While, for other objects such as vegetation, the normal vectors of the points are inconsistent. If the angle between the normal vector of a point and that of its n nearest neighbor points is within θ degrees (n and θ are variables), the point is called a regular point. In this paper, considering that the angle between the normal vectors of facade points does not have a big difference, the default values of n and θ are 5 and 20, respectively.

These two thresholds each have a loose value range. The default value is selected to avoid the influence of local noise in the point cloud. In a single part formed after Euclidean clustering, the ratio of regular points to all points inside the part is called regularity coefficient. The threshold of the regularity coefficient is also adaptive. The single parts representing building facade have much higher regularity coefficients than those of other parts. The main filtering target is vegetation besides some streetlights and other objects.

From Figure 4, there are two peaks in the statistical distribution of the regularity coefficients of all extracted parts. The smaller peak is the regularity coefficient of most vegetation parts, and the larger peak is the regularity coefficient of most building facade parts. After connecting the two peaks and find the farthest point to the connecting line, the threshold can be calculated. Considering that the histogram of regularity coefficients usually has local fluctuations and that it is difficult to determine the extreme point, it is necessary to conduct kernel density estimate of the distribution histogram of the regularity coefficients in order to obtain a smooth curve. Then, the extreme point on the curve is identified, and a suitable threshold of the regularity coefficient is calculated. Finally vegetation and other parts are removed from the point cloud.

RANSAC-Based Building Facades Extraction and Parameterization

RANSAC is a common method to find the largest subset of data that conform to a given model. It can detect the largest plane in the point cloud. To detect all facades, it is necessary to remove interior points of the detected largest plane, and then run RANSAC on the remaining points repeatedly until the detected facade reaches the minimum limit. In this paper, we only need some planes with a high degree of matching, so the minimum limit is set to 200 points for a possible facade. The detected facade is an object with semantic information, such as a wall, so the boundary of the facade needs to be determined. Figure 5 illustrates an in-facade point data set which is projected on the facade. Taking the minimum inertial axis of a point as the *x* axis and the maximum inertial axis as *y*, these two axes can be determined by the two eigenvectors obtained from the afore mentioned eigenvalue decomposition of the point covariance matrix. These two eigenvectors are orthogonal. The *x* axis is in the direction of the largest degree of dispersion of the data points, the *y* is in the direction of the smallest degree of dispersion, and the *z*-axis perpendicular to the facade. The boundary of the facade can be determined by the maximum and minimum projections of the points on the *x* and *y* axes, which are the corner points A, B, C, D.

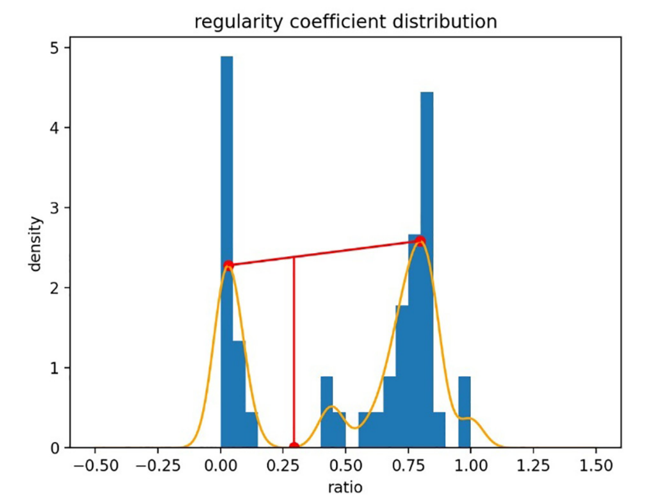

Figure 4. Determination of regularity coefficient threshold.

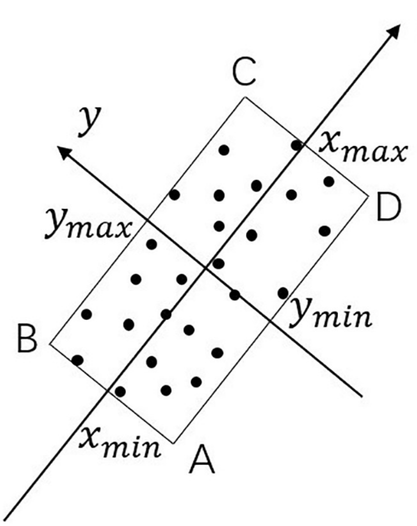

Figure 5. Determination of facade boundary.

Post-Processing

In this step, the “parallel and close” facades that have been repeatedly detected are fused. The method for identifying “repeatedly detected” facades is based on the angle of normal vectors and the vertical distance between parallel facades. If the angle between two normal vectors is small enough and the vertical distance of the two corresponding parallel facades is less than a threshold, the two facades are considered to be the same. The threshold is set as twice the average distance of points in the data, as in practice, there are very few walls within this distance.

However, there is another situation, in which the two walls of two buildings are indeed on the same facade, and there is a “side distance” d_s (Figure 6b). This kind of facades should not be merged into one, so it is necessary to set the “side distance” limit. Figure 6a illustrates the “parallel and similar” facades that need to be fused. When the vertical distance and the side distance of the parallel facades are within the shaded area in Figure 6c, the two facades are fused, and the facade boundary is re-determined.

Descriptor-Object Vicinity Distribution Feature

After all regular facades are extracted as the “control points” for point cloud registration, a feature descriptor, OVDF, is defined to describe the distribution of the regular facades, which is used in subsequent facade-matching. Then the best similar transformation matrix can be estimated based on the matched facades.

Figure 7 explains the principle of facade matching. If facade A in the source point cloud P and facade B in the target point cloud Q are corresponding facades, the distribution of other facades around the two facades should be similar in the two point clouds.

The planar spatial relationship vector $R_{A,i}$, as in Equation 4, is defined to describe the positional relationship between a neighboring facade and facade A.

$$R_{A,i} = (x_{A,i}, y_{A,i}, z_{A,i}, \alpha_{A,i}, \beta_{A,i}, \gamma_{A,i}, a_{A,i}, b_{A,i}, s_{A,i}) \tag{4}$$

where $x_{A,i}$, $y_{A,i}$, $z_{A,i}$ are the coordinates of the center point of facade *i* in the local coordinate system, and $\alpha_{A,i}$, $\beta_{A,i}$, $\gamma_{A,i}$ are the unit normal vector of facade *i* transformed to the local coordinate system, and $a_{A,i}$, $b_{A,i}$, $s_{A,i}$ are scale factors which are the square roots of the length, width and area of facade *i* in the local coordinate system.

OVDF is a unique signature to identify every facade, which is obtained by overlaying the surrounding relationship vectors of facade

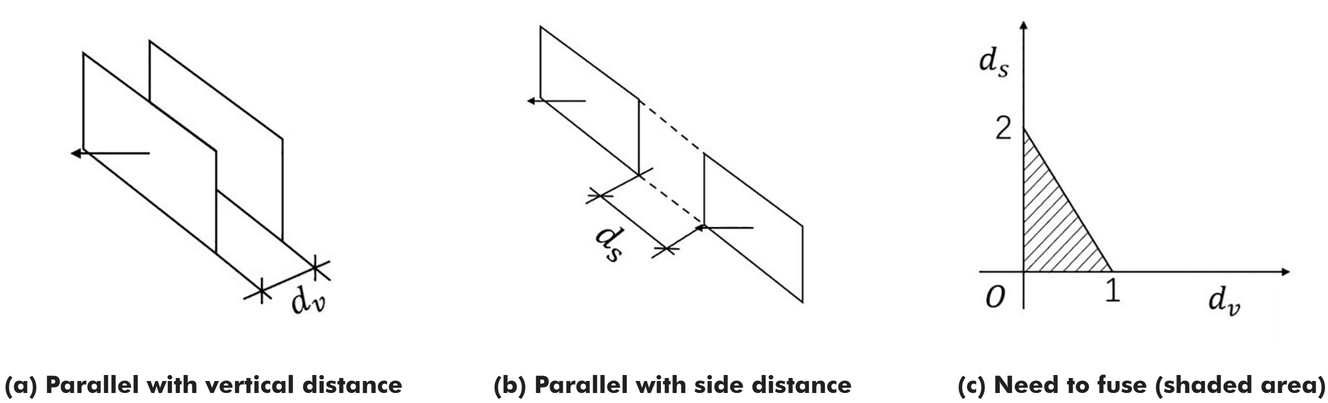

Figure 6. “Parallel and close” facades.

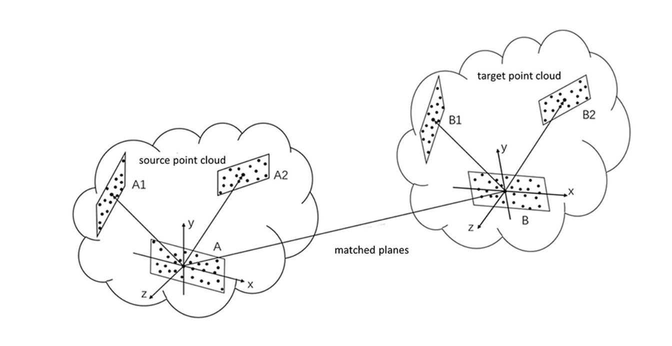

Figure 7. Principle of facade matching.

A. It expresses the facades around facade A relative to facade A's own distribution relationship.

$$F_A = (R_{A,1}, R_{A,2}, \ldots, R_{A,K}) \tag{5}$$

where, F_A is the OVDF vector of facade A which is constant in rotation, translation, and scale. After the local coordinate system is established, the $R_{A,i}$ in Equation 4 and Equation 5 can be interpreted as the relationship vector between the neighboring facade i and facade A in the local coordinate system of facade A. F_A is expressed by K surrounding relationship vectors.

There are rotation, translation, and scale differences between a lidar point cloud and an oblique photographic point cloud obtained by structure from motion (SFM). To maintain the relationship vector of the same pair of facades after the above non-rigid transformation, the relationship vector needs to keep rotation, translation, and scale invariant.

Translation and Rotation Invariance of OVDF

It is common to set a local coordinate system, and then calculate the feature relative to the local coordinate system to insure the translation and rotation invariance.

The local coordinate system determined in this paper is shown in Figure 8a, with the center of the facade as the origin of the coordinate system, and the z-axis perpendicular to the facade. The x-axis is the direction of the maximum projection of the facade data, and the y-axis is the direction of the minimum projection of the data. In practice, as shown in Equation 6, the covariance matrix is first calculated for the points in the facade, and then the three eigenvectors obtained from the eigenvalue decomposition are the three axis directions. Figure 8b and 8c are the coordinate system determination results of low buildings and high buildings, respectively.

$$\begin{cases} \Sigma = \sum_{i=1}^{m} \left(p_i - \bar{p}\right)\left(p_i - \bar{p}\right)^T \\ \Sigma e_x = \lambda_1 e_x \\ \Sigma e_y = \lambda_2 e_y \\ \Sigma e_z = \lambda_3 e_z \end{cases} \tag{6}$$

Calculate the area weighted center points of the three nearest facades so that the coordinate origin is roughly inside the building. Determining the coordinate axes and their directions can ensure the rotation invariance of the OVDF feature.

Scale Invariance of OVDF

When two point clouds are zoomed in out, different objects in the two point clouds should be zoomed to the same scale at the same time.

In Equation 7, e_x, e_y, e_z denote standard deviation of the coordinate axis directions, λ_1, λ_2, and λ_3 are the eigenvalues of the covariance matrix of the points which represent the sum of the squared deviations of the data in the three coordinate directions, m means the number of points in the facade, and $\sqrt{\lambda_i / m-1}$ is the unbiased estimate of standard deviation.

$$\begin{cases} e_x = \text{std}_x = \sqrt{\dfrac{\lambda_1}{m-1}} \\ e_y = \text{std}_y = \sqrt{\dfrac{\lambda_2}{m-1}} \\ e_z = \text{std}_z = \sqrt{\dfrac{\lambda_3}{m-1}} \end{cases} \tag{7}$$

When calculating the relationship vector, the position component and the scale component need to be divided by the corresponding e_i. The OVDF feature obtained in this way is scale-invariant.

OVDF-Based Facade Matching

If m facades are detected in the source point cloud and n facades are detected in the target point cloud, their similarity coefficients can be calculated from the OVDF features of each pair of facades in the source point cloud and the target point cloud. Considering that facade detection in the section "Extraction of Building Facades" may not be able to detect all, and the facades around facade A do not match one-on-one with the facades around the corresponding facade B in the target point cloud (refer to Figure 7), it is necessary to find the most likely pair in order to improve the robustness of the matching algorithm.

Equation 8 gives the calculation of the facade similarity coefficient:

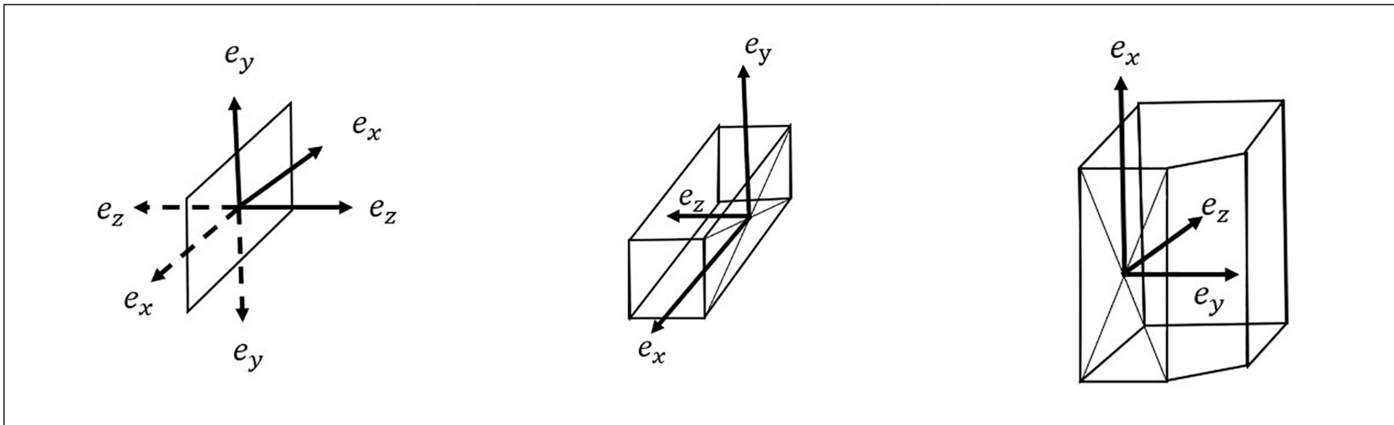

(a) Variable coordinate direction **(b) Coordinate direction I** **(c) Coordinate direction II**

Figure 8. Coordinate direction.

$$
\begin{cases}
W_{A,B} = \text{match}\left(\left\{R_{A,1}, R_{A,2}, \ldots, R_{A,K}\right\},\right. \\
\qquad \left.\left\{R_{B,1}, R_{B,2}, \ldots, R_{B,K}\right\}\right) \\
\text{Sim}\left(F_A, F_B\right) = \sum_{w \in W_{A,B}} w
\end{cases}
\tag{8}
$$

where $W_{A,B}$ is a set of matched relationship vector between facade A in the source point cloud and the corresponding facade B in the target point cloud. The similarity coefficient between facade A and B is the sum of the similarity coefficients of the relationship vectors. The similarity coefficient between the relationship vectors is computed in Equation 9:

$$
\begin{cases}
\text{Dis}\left(R_{A,k1}, R_{B,k2}\right) = \sqrt{\left(x_{A,k1} - x_{B,k2}\right)^2 + \left(y_{A,k1} - y_{B,k2}\right)^2 + \left(z_{A,k1} - z_{B,k2}\right)^2} \\
\text{Ang}\left(R_{A,k1}, R_{B,k2}\right) = acr\cos\left(\alpha_{A,k1} \cdot \alpha_{B,k1} + \beta_{A,k1} \cdot \beta_{B,k1} + \gamma_{A,k1} \cdot \gamma_{B,k1}\right) \\
\text{Sca}\left(R_{A,k1}, R_{B,k2}\right) = \sqrt{\left(a_{A,k1} - a_{B,k2}\right)^2 + \left(b_{A,k1} - b_{B,k2}\right)^2 + \left(s_{A,k1} - s_{B,k2}\right)^2} \\
\text{Sim}\left(R_{A,k1}, R_{B,k2}\right) = e^{-3\left(\frac{Dis}{a_1} + \frac{Ang}{a_2} + \frac{Sca}{a_3}\right)}
\end{cases}
\tag{9}
$$

where ($R_{A,k1}$, $R_{B,k2}$) means there are a facade $k1$ around facade A and a facade $k2$ around facade B; Dis($R_{A,k1}$, $R_{B,k2}$) denotes the positional distance between the center points of $k1$ and $k2$ in the local coordinate system; Ang($R_{A,k1}$, $R_{B,k2}$) is the angular distance which represents the angle between the normal vectors of $k1$ and $k2$; Sca($R_{A,k1}$, $R_{B,k2}$) refers to the scale distance, indicating the size difference between $k1$ and $k2$ in the local coordinate system; and a_1, a_2, a_3 represent distance, angle, and scale normalization parameter. If any of the above distances exceeds its corresponding parameter, the similarity score is close to 0. The default values are set to 0.5 m for distance, 15 degrees for angle, and 0.5 for scale. These are parameters used to balance the effects of translation, rotation, and scale transformation on OVDF.

The similarity of the two relationship vectors should be inversely related to the three distance measures. In this paper, an inverse exponential relationship is adopted. The steps for matching facades are as follows:

Step 1: Calculate the similarity coefficients for the 1~m facades in the source point cloud and the 1~n facades in the target point cloud, respectively.

Step 2: After obtaining the similarity coefficients between all the facades in the source point cloud and all the facades in the target point cloud, match similar facades in two point clouds to obtain the paired facades.

Step 3: Compare the similarity scores of all facade pairs to a threshold. The pairs with a similarity score higher than the thresholds that are considered corresponding facades.

Suppose each facade in the source point cloud and the target point cloud is a node. All nodes in the source point cloud form a set P, and all nodes in the target point cloud form a set Q. A weighted edge is formed between each node in P and each node in Q, and the weight of the edge is the similarity coefficient between the two nodes, i.e., facades. The strategy is to choose the one with the largest weight among the remaining edges each time, which represents the current optimal match. Figure 9 is an example of matching; the matching order is A1-B3, A4-B1, A2-B4.

This method does not need the sum of all edge weights to be the largest, so a greedy strategy is used to find the current largest weight. Once the pair with the largest weight is found, the two nodes are deleted. It can ensure that the currently found match is the best among the remaining pairs.

Finally, the transformation matrix T_s is calculated when the cost function J in Equation 10 takes the minimum value.

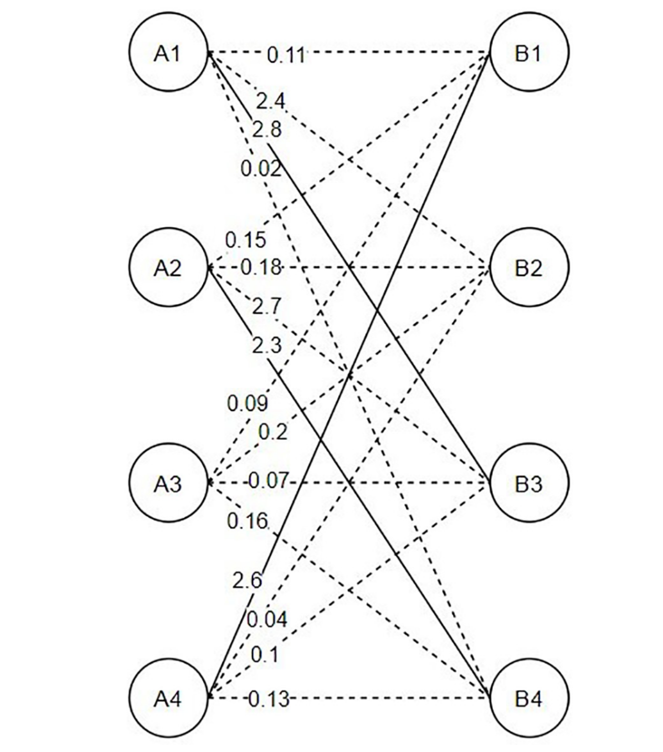

Figure 9. Bipartite graph matching.

$$
J = \sum_{i=1}^{n} \left\langle \vec{n}_i, T_s \vec{n}_i' \right\rangle^2 + \left(\left(T_s p_i' - p_i\right) \cdot \vec{n}_i\right)^2
\tag{10}
$$

where $\vec{n}_i'$ and $\vec{n}_i$ represent the normal vectors of paired facade i in the source point cloud and target point cloud, p_i' and p_i represent the center point coordinates of i, and T_s is the transformation matrix from the source point cloud to the target point cloud.

Discussion of Parameter Settings

A number of parameters are used in the implementation of the proposed method for coarse registration. These parameter values are set according to the statistical characteristics of the point cloud instead of heuristic settings. We consider the same parameter values for both lidar and photography point clouds. The parameter settings are discussed below.

In ground points removal step, the ground sampling distance is the average distance among the points, which ensures that most of the ground points can be removed according to the curve inflection point. In the process of calculating the regularity coefficients of single parts, there are two parameters n and θ. The normal vector directions of the points in a facade generally do not have a big difference, while the normal vector directions of the points in other objects are quite different. The value range of angle θ can have a relatively loose range. The value of n indicates the neighborhood size of a point. This value can be either an integer calculated according to the density and number of the points in the point cloud, or the number of points within a circular neighborhood with a certain radius. In the process of removing non-facade objects, the threshold value is easy to determine as there is a significant difference of the regularity coefficients between facade objects and non-facade objects. In addition, it is not necessary to use all facades in subsequent processing. If there exist a small number of other non-facade objects, it has little impact on the subsequent matching process because the matching degree of OVDF between two objects only increases if the pair are similar and not decreases if the pair are different. The post-processing method is based on the angle of normal vectors and the vertical distance. The angle threshold and distance threshold are limited to a small range, which ensures that the merged planes belong to the same facade.

The automatic registration and manual registration result in very similar outcomes. And the algorithm would obtain the same result and accuracy by switching the target point cloud.

Experiment and Analysis

The experiment includes two steps: the preliminary test step and the multi-sensor data fusion step. In the test step, a test is designed to verify the feasibility of the method. First, sample transformation parameters (transition, rotation, scale) are used to transfer a single ALS point cloud to a new point cloud in a new coordinate system. Then, the proposed method is used to register the transferred point cloud to the original one.

In the multi-sensor data fusion step, we apply the proposed method to multi-sensor data, i.e., a lidar data set and an oblique photogrammetric data set in Dublin, Ireland, to register both the entire study area and the partially overlapping area. Assessment is conducted to evaluate the effectiveness of the proposed method.

Preliminary Test

Figure 10 shows the original point cloud and the transformed point cloud. For display, the angle of view in Figure 10 has been adjusted.

The parameters of the transformation matrix are shown in Table.1. According to the method, the transformation matrix is calculated.

The two point clouds after the transformation are processed by the ICP algorithm, as shown in Figure 11, and the transformation matrix of ICP and the root-mean-square error (RMSE) between the two point clouds is calculated (Table 2).

By comparing the transformation matrix after coarse-fine registration with the original true value, we find that the proposed method provides a good initial value for ICP fine registration, and the result is very close to the true value.

Multi-Sensor Data Fusion

Multi-Sensor Data

After the preliminary test, the proposed method is proved to be feasible. In this step, the method is applied to multi-sensor data. The multi-sensor lidar and oblique photogrammetric data are both from the New York University Spatial Data Repository, which were collected on March 26, 2015, and cover an area of more than 2 km^2 in Dublin, Ireland. The ALS (lidar) data set is acquired by the TopEye system S/N 443 laser scanner, and the oblique photogrammetric data set is collected from a UAV by two cameras. Neither data set has positional information. Table 3 lists the information of the two point cloud data sets.

Table 3. Information of the multi-sensor point cloud data.

Type	Number	Density	Shortest Point Spacing/m	Largest Point Spacing/m	Average Point Spacing/m
Lidar	5926176	9 pt/m^2	0.400	4.592	0.477
Image + SfM	4404429	59 pt/m^2	0.150	2.973	0.167

SfM = structure from motion; pt = point.

Figure 12a displays the location of the study area. The area in Figure 12b is selected to verify the effectiveness of the method when the two point clouds only partially overlap.

Results of Building Facades Extraction

The results of ground points removal and non-facade points removal mentioned in the sections "Ground Points Removal" and "Regularity Coefficient-Based Non-Facade Points Removal" are shown in Figure 13 (a part of the study area is displayed).

Figure 13a displays the result of ground removal. Almost all pixels of facades and some pixels of other objects remain in the resulting data. Figure 13b illustrates the distribution of regularity coefficients of the single parts after Euclidean clustering segmentation. In Figure 13c, each single part is rendered a color based on its regularity coefficient.

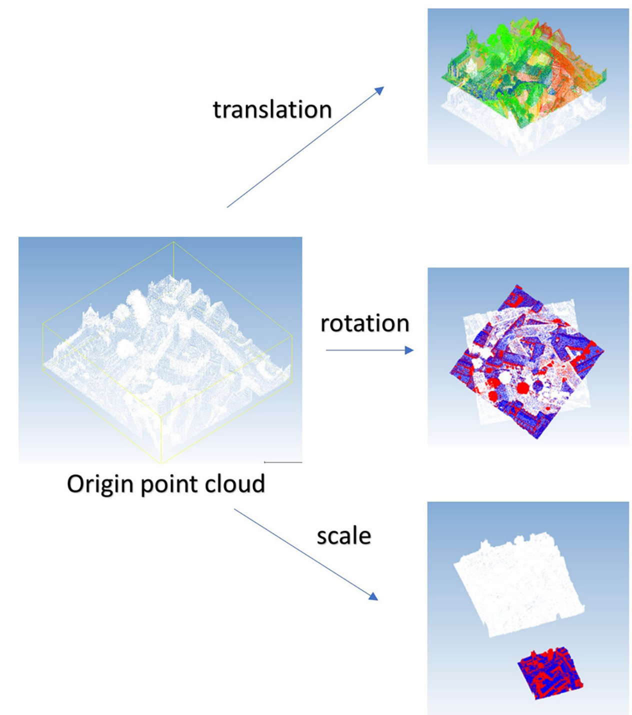

Figure 10. Samples of transform point cloud.

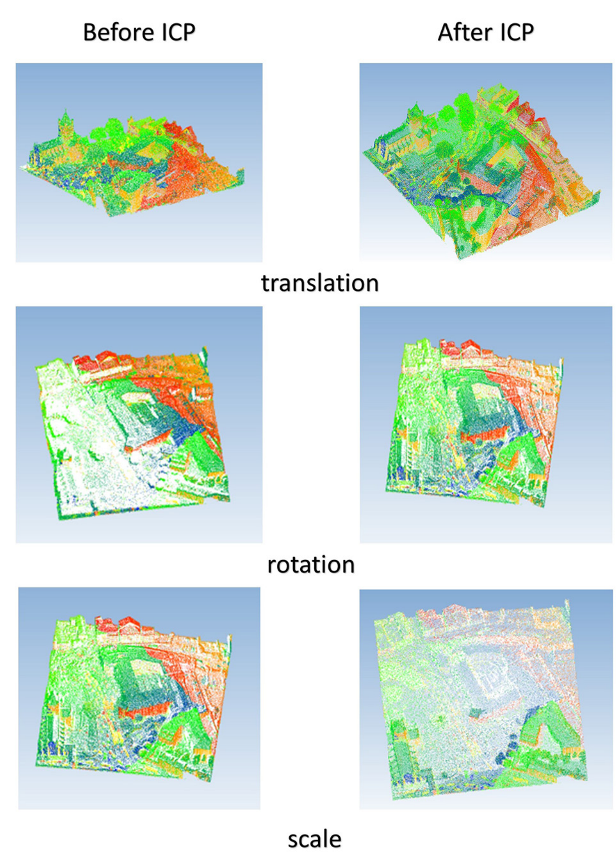

Figure 11. Registration before and after ICP.

Table 1. Parameters of the transformation matrix.

Type	Transformation Matrix	Result of Method
Translation	$\begin{bmatrix} 1 & 0 & 0 & 20 \\ 0 & 1 & 0 & 20 \\ 0 & 0 & 1 & 20 \\ 0 & 0 & 0 & 1 \end{bmatrix}$	$\begin{bmatrix} 1.0003 & 0.000024 & 0.00055 & 20.01388 \\ 0.000024 & 1.0003 & 0.000229 & 20.08074 \\ 0.00055 & 0.0000229 & 1.0003 & 20.14744 \\ 0 & 0 & 0 & 1 \end{bmatrix}$
Rotation	$\begin{bmatrix} 0.70710677 & -0.70710677 & 0 & 0 \\ 0.70710677 & 0.70710677 & 0 & 0 \\ 0 & 0 & 1 & 0 \\ 0 & 0 & 0 & 1 \end{bmatrix}$	$\begin{bmatrix} 0.705923 & -0.726378 & -0.063025 & -0.401441 \\ 0.72341 & 0.708618 & 0.070727 & -1.93856 \\ 0.094636 & -0.004294 & 1.010351 & 2.3073 \\ 0 & 0 & 0 & 1 \end{bmatrix}$
Scale	$\begin{bmatrix} 0.5 & 0 & 0 & 0 \\ 0 & 0.5 & 0 & 0 \\ 0 & 0 & 0.5 & 0 \\ 0 & 0 & 0 & 1 \end{bmatrix}$	$\begin{bmatrix} 0.499323 & -0.001161 & 0.003014 & 0.471401 \\ 0.001172 & 0.4993284 & 0.001975 & -0.111107 \\ 0.003005 & -0.001981 & 0.499321 & -0.058174 \\ 0 & 0 & 0 & 1 \end{bmatrix}$

Table 2. Iterative Closest Point (ICP) result and root-mean-square error (RMSE).

Type	ICP Transformation Matrix	Result of Method + ICP	RMSE
Translation	$\begin{bmatrix} 1.000 & 0.000 & 0.000 & 0.006 \\ 0.000 & 1.000 & 0.000 & -0.013 \\ 0.000 & 0.000 & 1.000 & -0.056 \\ 0.000 & 0.000 & 0.000 & 1.000 \end{bmatrix}$	$\begin{bmatrix} 1.0003 & 0.000024 & 0.00055 & 20.01985 \\ 0.000024 & 1.0003 & 0.000229 & 20.06772 \\ 0.00055 & 0.0000229 & 1.0003 & 20.09142 \\ 0 & 0 & 0 & 1 \end{bmatrix}$	0.730567
Rotation	$\begin{bmatrix} 0.996 & 0.013 & 0.093 & 1.546 \\ -0.012 & 1.000 & -0.09 & 1.146 \\ -0.093 & 0.09 & 0.996 & -2.815 \\ 0 & 0 & 0 & 1.000 \end{bmatrix}$	$\begin{bmatrix} 0.71677 & -0.72287 & 0.06825 & 0.035 \\ 0.705435 & 0.724387 & 0.07394 & -0.2071 \\ 0.000346 & 0.008786 & 1.015 & -0.3954 \\ 0 & 0 & 0 & 1 \end{bmatrix}$	0.82872
Scale	$\begin{bmatrix} 1.000 & 0.002 & 0.006 & -0.415 \\ -0.002 & 1.000 & -0.004 & 0.229 \\ -0.006 & 0.004 & 1.000 & 0.104 \\ 0 & 0 & 0 & 1 \end{bmatrix}$	$\begin{bmatrix} 0.499307 & -0.00015 & 0.006014 & 0.26422 \\ 0.000162 & 0.499338 & -0.00001 & -0.00295 \\ 0.000013 & -0.00002 & 0.499347 & -0.00794 \\ 0 & 0 & 0 & 1 \end{bmatrix}$	0.363455

Figure 13d(i) shows the result of non-facade points removal using the regularity coefficient threshold. The comparison between Figure 13d(i) and Figure 13d(ii) indicates that almost all non-facade single parts have been removed except two vegetation parts connected to the building single parts (the ellipse in Figure 13d(ii)). Because the vegetation and the facade are connected, they are segmented as one object during the Euclidean clustering process. Although the regularity coefficient of the object is smaller than the general facade object, it is still larger than the threshold, and thus not removed. This doesn't affect subsequent matching process, as these objects are not "optimal" matching objects.

Figure 14a displays the result of facade detection discussed in the section "RANSAC-Based Building Facades Extraction and Parameterization" in the same part of the study area as in Figure 13. The detected facades are generally correct, but there are two problems. One is that the same wall is detected in multiple facades with small differences, which is caused by the thickness of the wall. The other problem is that some points are on the extended surface of the wall, and the boundary of the detected facade is not accurate enough. Therefore, the detected facade boundary needs to be optimized. Figure 14b presents the result after the post-processing step.

Figure 15 is the final result of facade extraction in the entire study area: (a) is lidar point cloud, and (b) is UAV photogrammetry point cloud.

Results of Facade Matching

Table 4 lists the total number of extracted facades in the entire study area and the partially overlapping area.

To evaluate the result of facade extraction, the extracted facades are manually divided into three categories according to the quality. Perfect

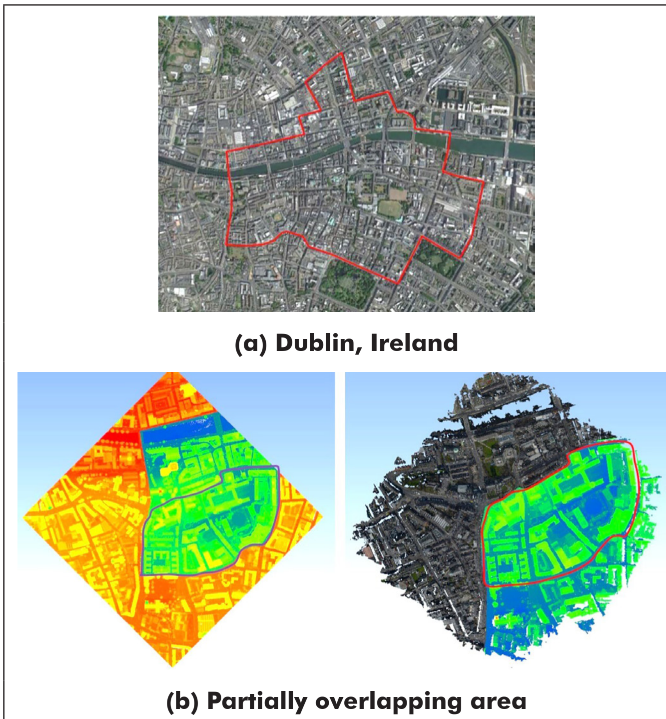

Figure 12. Multi-sensor data.

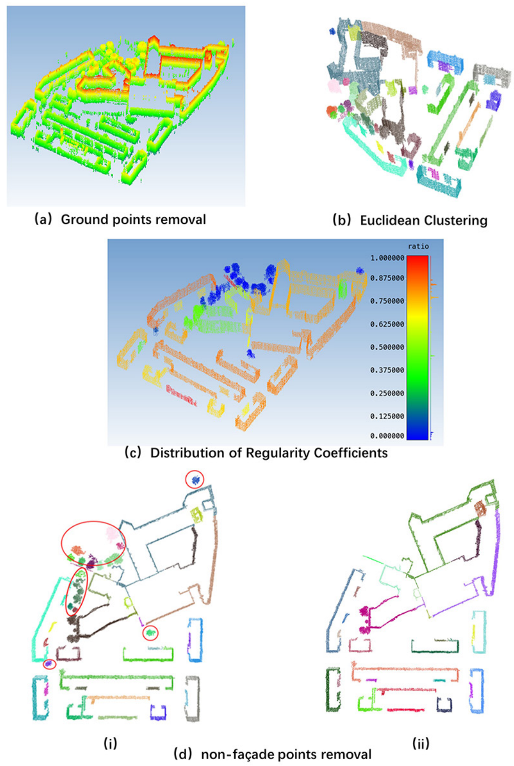

Figure 13. Intermediate results of ground points removal and non-facade points removal.

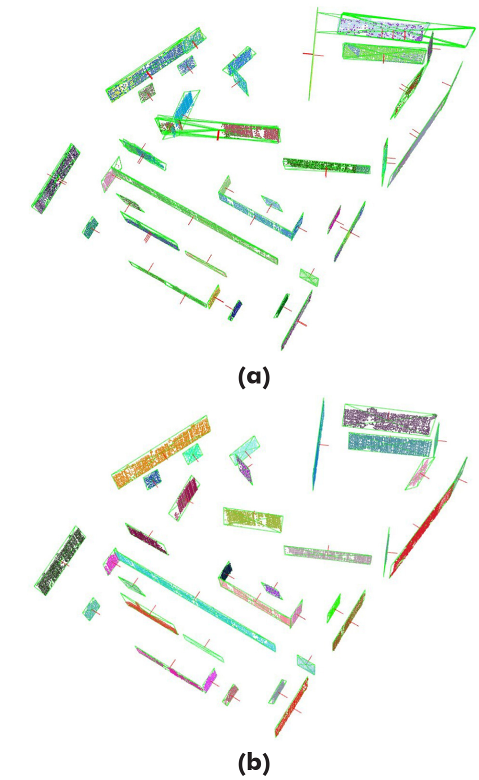

Figure 14. (a) Result of building facade extraction; (b) Result after the post-processing step.

Table 4. Number of extracted facades.

1-Lidar	1-Image	2-Lidar	2-Image
638	691	277	314

1 = the entire study area; 2 = the partially overlapping area; Image = the oblique photography point cloud.

Table 5. Result of matching facades.

Area	All	Correct	Perfect	Subpar	Bad
1	11	11	8	3	0
2	5	5	4	1	0

facades: the extracted facade points cover the entire area. Subpar facades: the extracted facades include the wall of the building and other points such as vegetation points. Bad facades: non-facade points are incorrectly extracted. Bad facades are not allowed to participate in the later facade matching process to avoid incorrect result.

Subsequently, OVDF is used to describe and match the facades. The number of the total matched facades and the matched three categories in two areas are shown in Table 5. Figure 16 displays the matching results in area 2 (area 2 is partially overlapping data, and the part framed in red is overlapped area). On the right is lidar point cloud and on the left is oblique photography point cloud. Five pairs of matches have been found in total.

Registration Results of the Two Data Sets

Finally, the transformation matrix of the matching facades, which is the transformation matrix from the oblique photography point cloud to the lidar point cloud, is calculated. The registration result is shown in Figure 17. Figure 17a is the registration result in the entire study area. Figure 17b displays the registration results in the partially overlapping area. Figure 17c–d show the alignment results of a vertical view.

Quantitative Evaluation

The proposed registration algorithm is quantitatively evaluated in two ways. The first way is to use manually selected control points and ICP as a reference and compare the difference of the transformation matrix

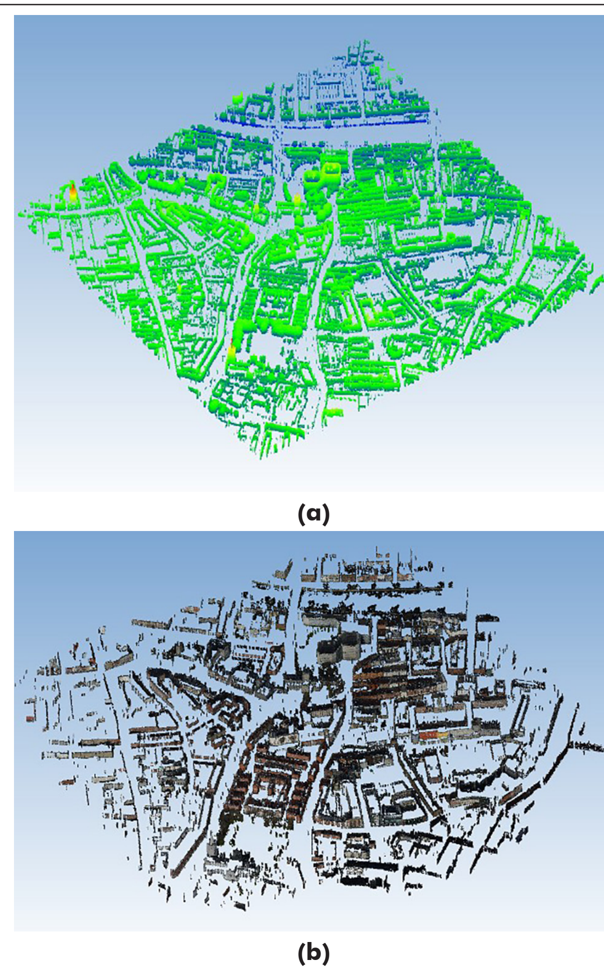

Figure 15. Facade extraction result in the entire study area.

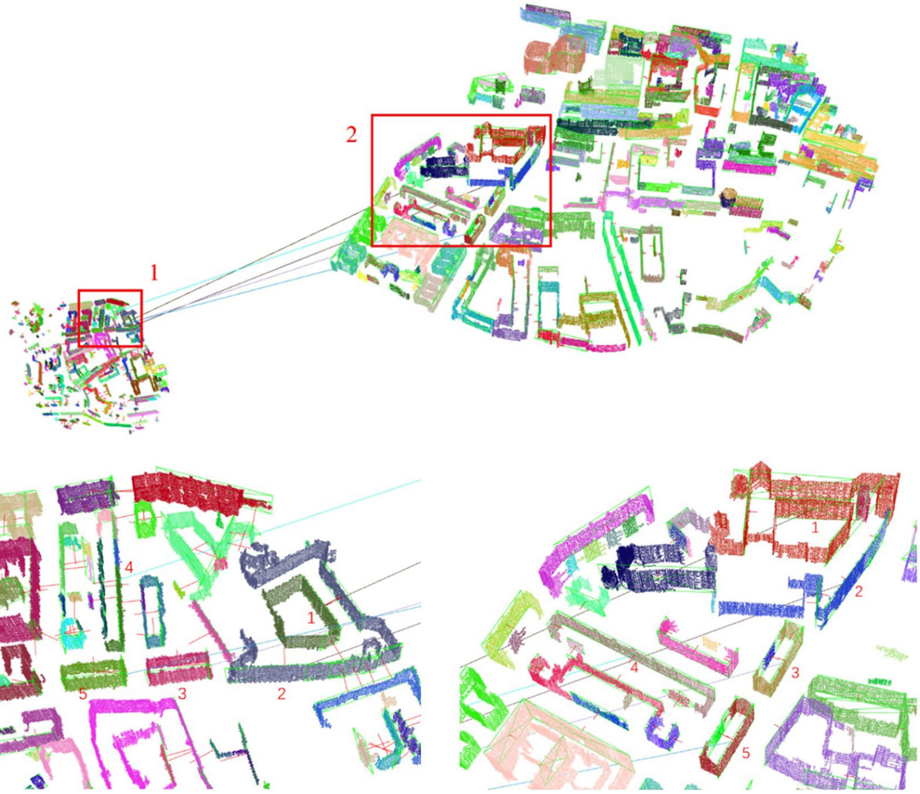

Figure 16. Matching result (five facades matched in total in area 2).

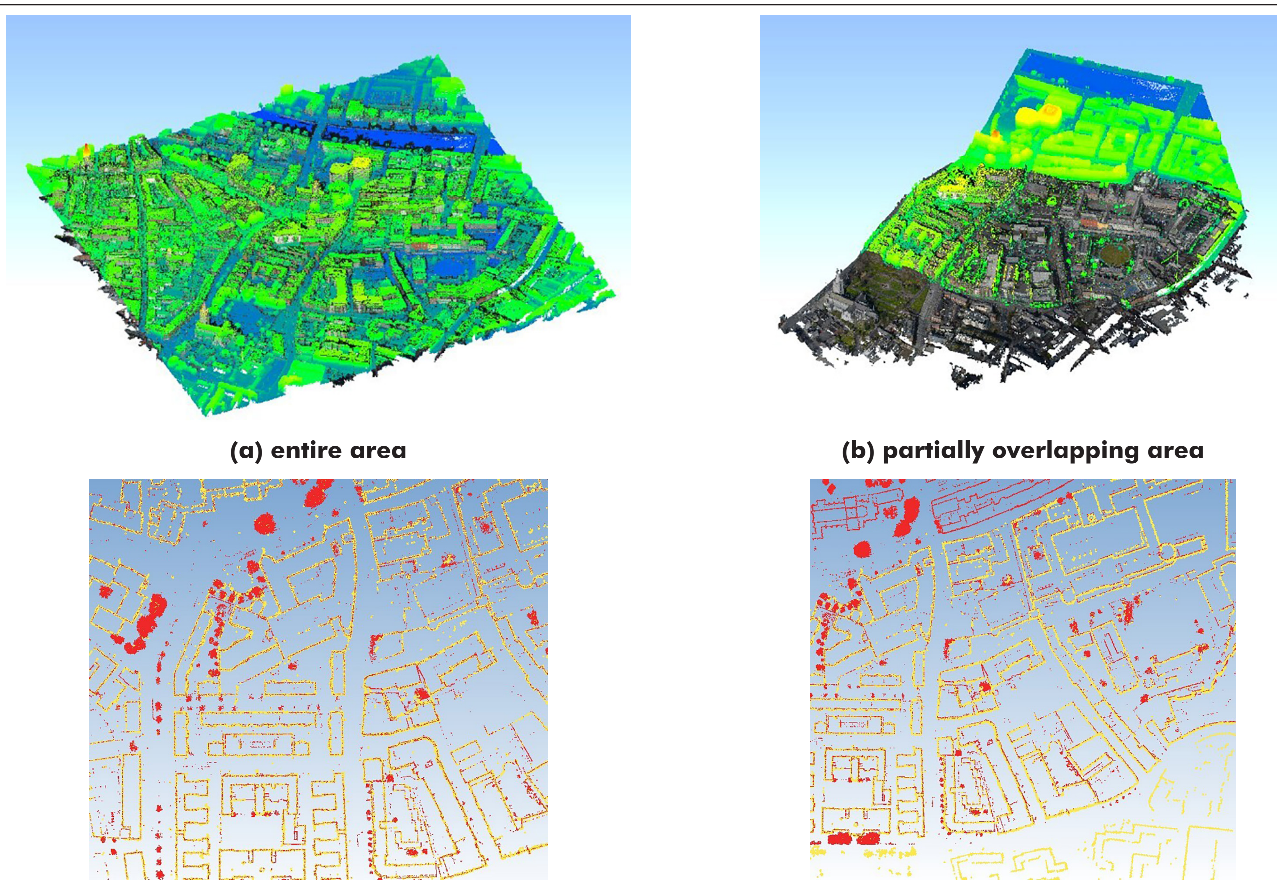

(a) entire area

(b) partially overlapping area

(c) Facade point alignment 1

(d) Facade point alignment 2

Figure 17. Automatic registration and alignment results.

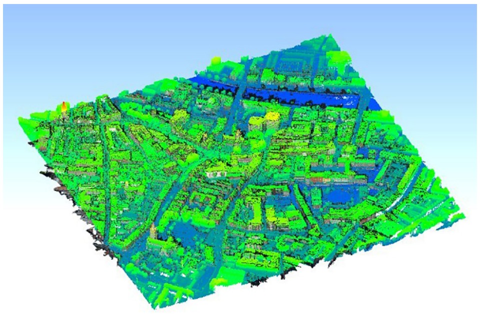

(a) test 1-Lidar data

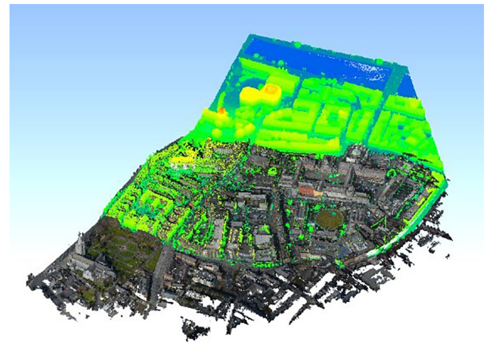

(b) test 1-oblique photography data

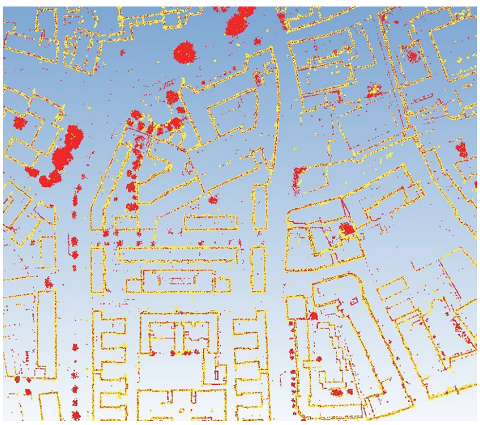

(c) test 2-LiDAR data

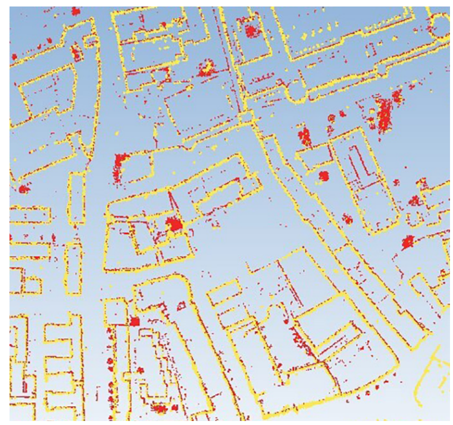

(d) test 2-oblique photography data

Figure 17. Automatic registration and alignment results.

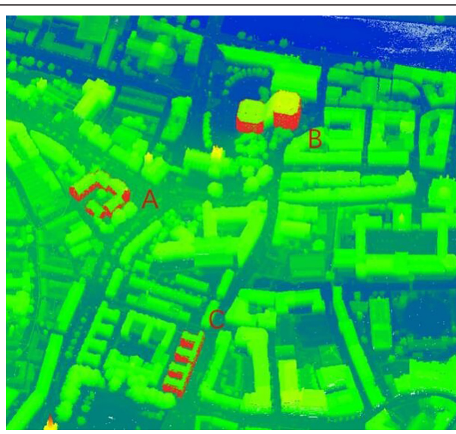

(a) manual registration test 1

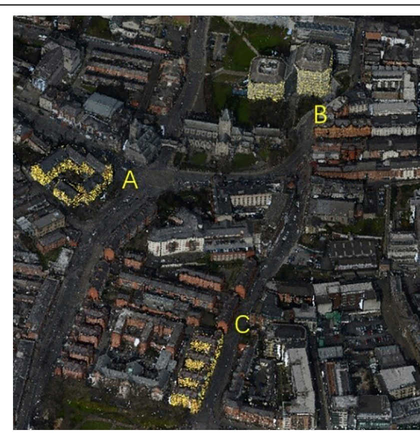

(b) manual registration+ICP test1

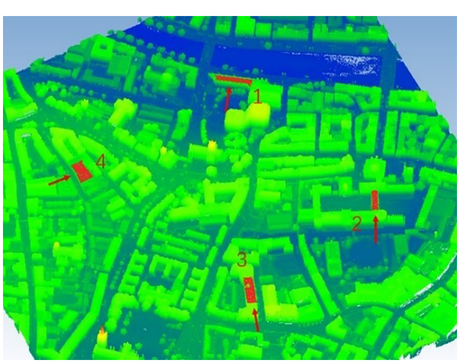

(c) manual registration test 2

(d) manual registration+ICP test 2

Figure 18. Test data 1 and 2.

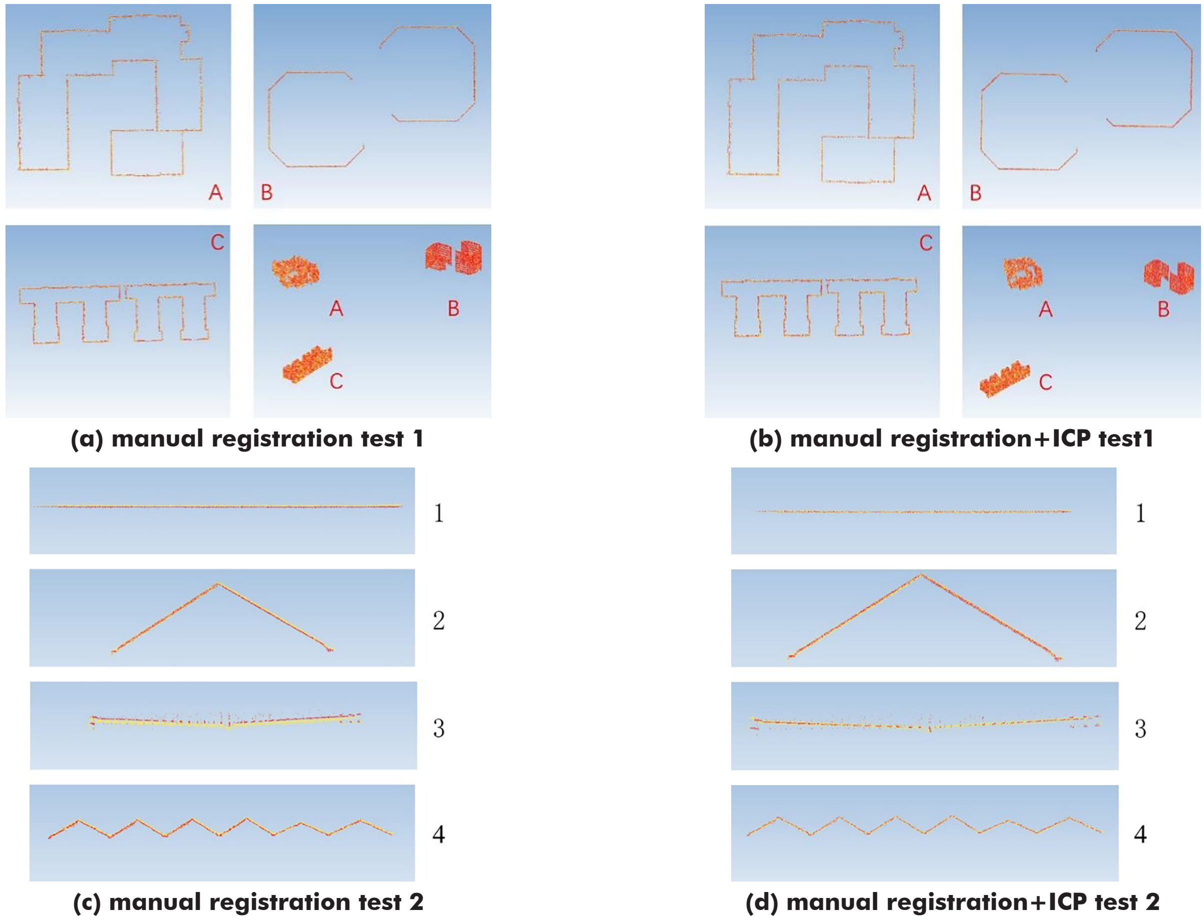

Figure 19. Manual registration results of the oblique photography point cloud and the lidar point cloud. Red color means lidar point; yellow color means oblique photography point.

between the automatic registration based on the prosed method and the manual registration. The second is to manually select some regular ground objects from the lidar point cloud and the oblique photography point cloud, calculate the transformation matrix, compute the distance from the points to their closest points in the two point clouds, and use the minimum, maximum, and average distance values to evaluate the difference between the two point clouds.

Figure 18 shows the test 1 data and test 2 data for the evaluation. Test 1 data are manually selected corresponding features from point cloud (the facades of three buildings, marked in red, respectively labeled A, B, and C), which are used to test the horizontal accuracy of the registration. Test 2 data are manually selected corresponding features used to verify the vertical accuracy of the registration. Ten control points are selected for each manual registration.

The alignment results of manual registration and manual registration + ICP for the two test data are shown in Figure 19. ICP can slightly improve the accuracy of manual registration. The result of the manual registration is further optimized and used as the reference standard for evaluating subsequent registration results. The accuracies, i.e., the distances, of manual registration + ICP, for the two test data are listed in Table 6. These accuracies theoretically reach the upper limit.

The automatic registration results based on the proposed method are shown in Figure 20 and Table 7.

Table 6. Distance between the oblique photography point cloud and the lidar point cloud for Manual + ICP.

Test Set	Minimum/m	Maximum/m	Average/m	Std/m
Test 1	0.002	2.625	0.330	0.176
Test 2	0.011	1.386	0.240	0.107

ICP = Iterative Closest Point; Std = standard.

The transformation matrix of the automatic registration is compared with the transformation matrix of the manual registration, which is regarded as the best registration result. The comparison between the results of the proposed method and manual registration is listed in Table 8.

Where α represents the scaling factor of the transformation matrix, t_x, t_y, and t_z represent the absolute values of translation amounts in the x, y, and z directions; roll, pitch, and yaw represent the absolute values of rotation angles around the x, y, and z axis. This result shows that the accuracy of proposed automatic registration method is equivalent to the accuracy of manual registration with control points.

Figure 21 illustrates the registration results of three pairs of objects. The first example of church illustrates that the lidar point cloud effectively fills in the missing parts in the UAV data after registration. In the second example of the exercise yard, in addition to the buildings, there is a large circular ground area. With the matching of building facades, the entire point cloud is registered. The third example of a residential area shows that when multiple similar facades exist at the same time, the method can effectively match the corresponding facades.

The complete point cloud registration result of the entire area is shown in Figure 22.

Discussion and Conclusion

The study proposed an algorithmic framework for automatic registration of lidar and UAV photogrammetry point clouds. Facades extraction instead of key points extraction not only eliminates the calculation of a large amount of point features, but also is less susceptible to local noise. The OVDF feature is theoretically invariant to rotation, translation, and scale when describing and matching planar objects.

To ensure the correctness of the results, the method will minimize the negative influences on the subsequent steps if there are inevitable inaccurate results in the previous step. In the lidar and oblique

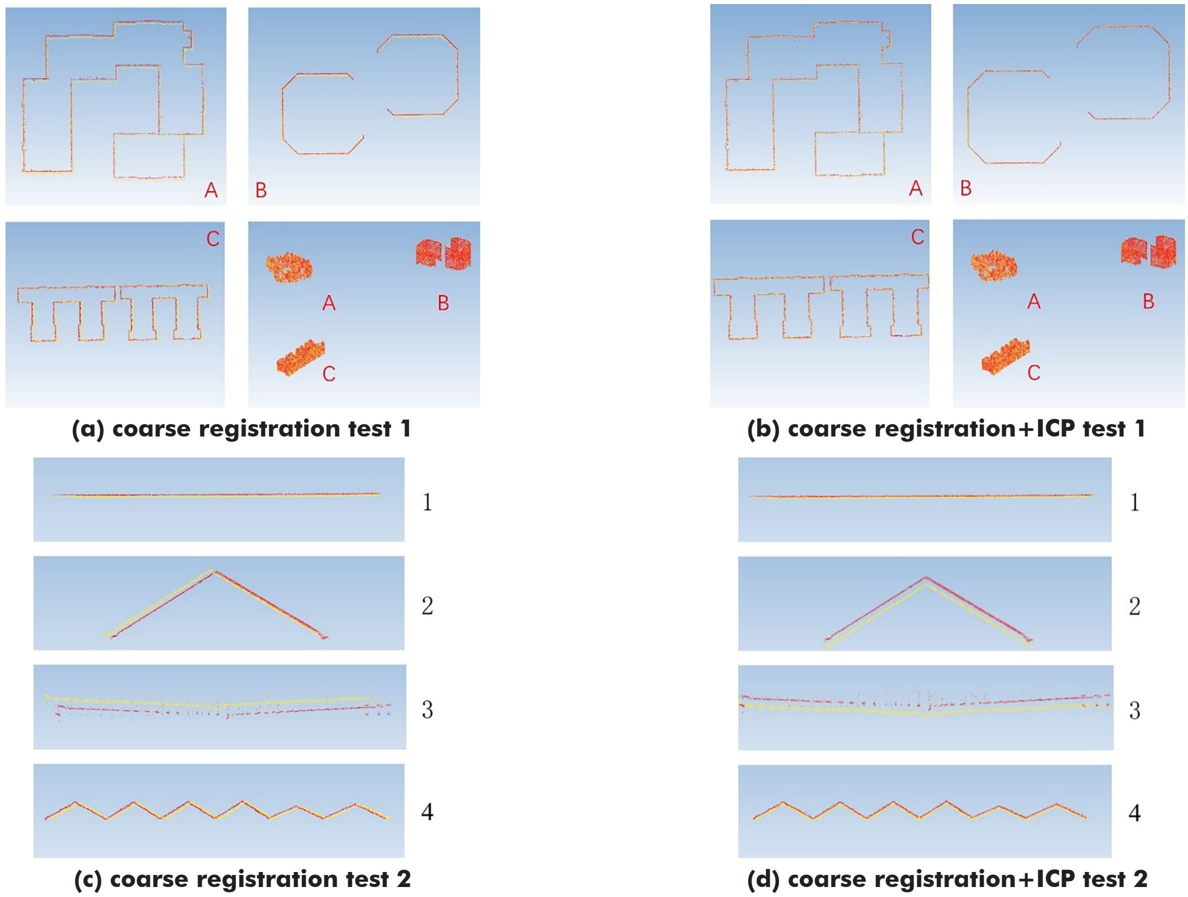

Figure 20. Automatic registration results of the oblique photography point cloud and the lidar point cloud based on the proposed method. Red color means lidar points; yellow color means oblique photography points.

photography data sets, the density and number of points are quite different, but the final extraction results of the facade objects are quite impressive. It further proves the robustness of the method. Experiment results show that the accuracy of this proposed automatic registration method is equivalent to the accuracy of manual registration with control points.

Table 7. Distance between the oblique photography point cloud and the lidar point cloud for the automatic registration based on the proposed method.

Test Set	Minimum/m	Maximum/m	Average/m	Std/m
Test 1	0.011	2.640	0.602	0.275
Test 1-ICP	0.016	2.346	0.347	0.178
Test 2	0.028	2.031	0.397	0.139
Test 2-ICP	0.031	1.539	0.347	0.099

ICP = Iterative Closest Point; Std = standard.

The entire process takes five minutes on a ubuntu virtual machine with 16 G of memory and 4 cores, 8 threads. The most time-consuming step is the calculation of regularity coefficient. This step needs to calculate the normal vector characteristics of the point; it takes more than 80% of the time.

One of the disadvantages of the method is that it may be less effective in urban data sets where there is a lack of building facades. According to the definition of OVDF, when there is a large error in the z-direction during the extraction of building facades, the registration accuracy is reduced. From the test result, the error in the z-direction is also larger than x-direction and y-direction. In future research, one solution is to add horizontal features to compensate for the errors in the z-direction instead of just assuming a vertical building facade to form OVDF. Another disadvantage is that although using the default parameter values can achieve good results, it requires further experimental exploration in the future.

Table 8. Comparison between the results of the proposed method and manual registration.

	Scale	Translation			Rotation		
Experiment	α	t_x/m	t_y/m	t_z/m	roll (x)/°	pitch (y)/°	yaw (z)/°
Standard	2.9647	383.001	356.914	318.387	0.7871	0.4670	56.0543
Test 1	2.9650	382.774	356.652	318.505	0.8670	0.5320	56.0600
1 + ICP	2.9650	383.091	356.816	318.135	0.7698	0.4744	56.0675
Difference 1	0.0003	0.090	0.098	0.252	0.0173	0.0074	0.0132
Test 2	2.9655	384.496	357.364	317.886	0.6031	0.8761	56.0816
2 + ICP	2.9655	381.891	356.732	318.549	0.9709	0.3556	56.9495
Difference 2	0.0008	1.110	0.182	0.162	0.1838	0.1114	0.8952

ICP = Iterative Closest Point.

Acknowledgments

This work was supported by China's National Key R&D Program (grant number 2019YFE0126400).

References

Aiger, D., N. J. Mitra and D. Cohen-Or. 2008. 4-points congruent sets for robust pairwise surface registration. *ACM Transactions on Graphics* 27(3):1–10.

Bae, K. H. and D. Lichti. 2008. A method for automated registration of unorganised point clouds. *ISPRS Journal of Photogrammetry Remote Sensing* 63(1):36–54.

Besl, P. J. and N. D. McKay. 1992. Method for registration of 3-D shapes. *IEEE Transactions on Pattern Analysis and Machine Intelligence* 14(2):239–256.

Biber, P. and W. Straßer. 2003. The normal distributions transform: A new approach to laser scan matching. Pages 2743–2748 in *Proceedings of the 2003 IEEE/RSJ International Conference on Intelligent Robots and Systems (IROS 2003)*, held in Las Vegas, Nev., 27 October–1 November 2003.

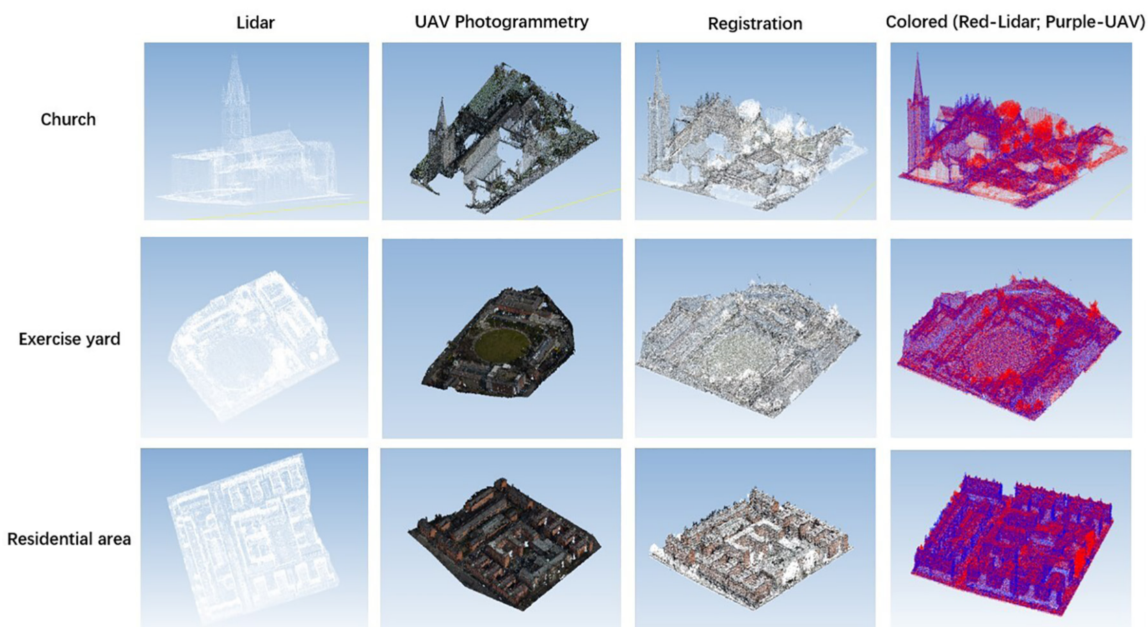

Figure 21. Automatic registration results of three pairs of objects.

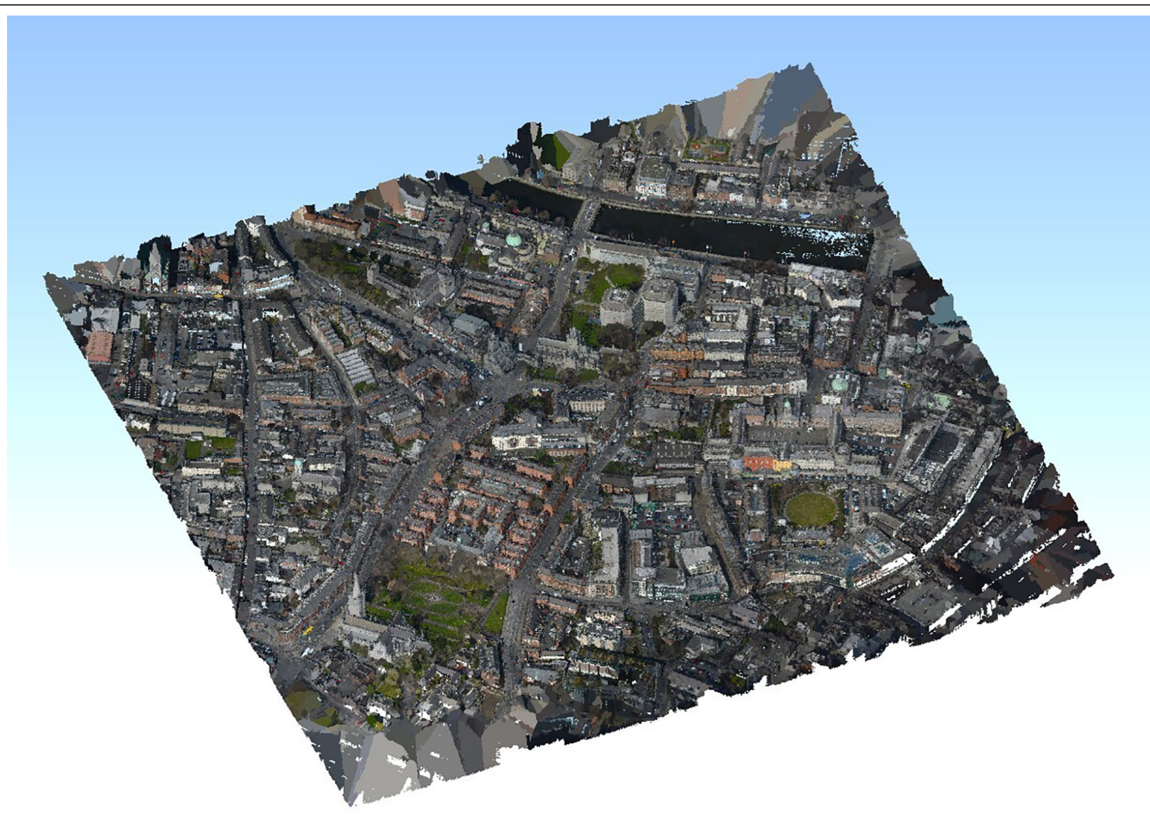

Figure 22. Automatic registration results of the entire area.

Bouaziz, S., A. Tagliasacchi and M. Pauly. 2013. Sparse iterative closest point. *Computer Graphics Forum* 32(5). https://doi.org/10.1111/cgf.12178.

Brie, D., V. Bombardier, G. Baeteman and A. Bennis. 2016. Local surface sampling step estimation for extracting boundaries of planar point clouds, *ISPRS Journal of Photogrammetry Remote Sensing* 119:309–319.

Campos-Taberner, M., A. Romero-Soriano, C. Gatta, G. Camps-Valls, A. Lagrange, B. Le Saux, A. Beaupere, A. Boulch, A. Chan-Hon-Tong, S. Herbin, H. Randrianarivo, M. Ferecatu, M. Shimoni, G. Moser and D. Tuia. 2016. Processing of extremely high-resolution LiDAR and RGB data: Outcome of the 2015 IEEE GRSS data fusion contest–Part A: 2-D Contest. *IEEE Journal of Selected Topics in Applied Earth Observations and Remote Sensing* 9(12):5547–5559.

Chen, Y. and G. Medioni. 1992. Object modelling by registration of multiple range images. *Image Vision Computing* 10(3):145–155.

Dijkman, S. and F. Van Den Heuvel. 2002. Semi automatic registration of laser scanner data. *International Archives of Photogrammetry Remote Sensing and Spatial Information Sciences* 34(5):12–17.

Flitton, G. T., T. P. Breckon and N. M. Bouallagu. 2010. Object recognition using 3D SIFT in complex CT volumes. Pages 1–12 in *Proceedings of the BMVC*, held in Aberystwyth, UK, 31 August–3 September 2010.

Gruen, A. and D. Akca. 2005. Least squares 3D surface matching. *Proceedings of the ASPRS 2005 Annual Conference*, held in Baltimore, Md., 7–11 March 2005.

Huang, X., L. Fan, Q. Wu, J. Zhang and C. Yuan. 2019. Fast registration for cross-source point clouds by using weak regional affinity and pixel-wise refinement. Pages 1552–1557 in *Proceedings of the 2019 IEEE International Conference on Multimedia and Expo (ICME)*. https://doi.org/10.48550/arXiv.1903.04630.

Huang, X., G. Mei and J. Zhang. 2020. Feature-metric registration: A fast semi-supervised approach for robust point cloud registration without correspondences. Pages 11363–11371 in *2020 IEEE/CVF Conference on Computer Vision and Pattern Recognition (CVPR)*, held in Seattle, Wash. https://doi.org/10.1109/CVPR42600.2020.01138.

Huang, X., J. Zhang, L. Fan, Q. Wu and C. Yuan. 2016. A systematic approach for cross-source point cloud registration by preserving macro and micro structures. *IEEE Transactions on Image Processing*. https://doi.org/10.1109/TIP.2017.2695888.

Hulik, R., M. Spanel, P. Smrz and Z. Materna. 2014. Continuous plane detection in point-cloud data based on 3D Hough Transform. *Journal of Visual Communication Image Representation* 25(1):86–97.

Knopp, J., M. Prasad, G. Willems, R. Timofte and L. V. Gool. 2010. Hough transform and 3D SURF for robust three dimensional classification. Pages 589–602 in *Proceedings of the Computer Vision–ECCV 2010–11th European Conference on Computer Vision,* held in Heraklion, Crete, Greece, 5–11 September 2010.

Kwak, T.-S., Y.-I. Kim, K.-Y. Yu and B.-K. Lee. 2006. Registration of aerial imagery and aerial LiDAR data using centroids of plane roof surfaces as control information. *KSCE Journal of Civil Engineering* 10(5):365–370.

Li, Y., R. Bu, M. Sun, W. Wu, X. Di and B. Chen. 2018. PointCNN: Convolution on χ-transformed points. Pages 828–838 in *Proceedings of the 32nd International Conference on Neural Information Processing Systems*, held in Montreal, Canada, 3–8 December 2018.

Lowe, D. G. 2004. Distinctive image features from scale-invariant keypoints. *International Journal of Computer Vision* 60(2):91–110.

Qi, C. R., L. Yi, H. Su and L. J. Guibas. 2017. Pointnet++: Deep hierarchical feature learning on point sets in a metric space. *arXiv preprint arXiv:1706.02413*. https://doi.org/10.48550/arXiv.1706.02413.

Raguram, R., O. Chum, M. Pollefeys, J. Matas and J. Frahm. 2013. USAC: A universal framework for random sample consensus. *IEEE Transactions on Pattern Analysis Machine Intelligence* 35(8):2022–2038.

Rusinkiewicz, S. and M. Levoy. 2001. Efficient variants of the ICP algorithm. Pages 145–152 in *Proceedings of the Third International Conference on 3-D Digital Imaging and Modeling*. https://doi.org/10.1109/IM.2001.924423.

Rusu, R. B., N. Blodow and M. Beetz. Fast point feature histograms (FPFH) for 3D registration. 2009. Pages 3212–3217 in *Proceedings of the IEEE International Conference on Robotics and Automation*. https://doi.org/10.1109/ROBOT.2009.5152473.

Salti, S., F. Tombari and L. D. Stefano. 2014. SHOT: Unique signatures of histograms for surface and texture description. *Computer Vision Image Understanding* 125(AUG.):251–264.

Shijie, L., T. Xiaohua, C. Jie, L. Xiangfeng, S. Wenzheng, X. Huan, C. Peng, J. Yanmin and Y. Zhen. 2016. A linear feature-based approach for the registration of unmanned aerial vehicle remotely-sensed images and airborne LiDAR data. *Remote Sensing* 8(2):82.

Stamos, I. and M. Leordeanu. 2003. Automated feature-based range registration of urban scenes of large scale. Pages II-Ii in *Proceedings of the IEEE Internal Conference of Computer Vision and Pattern Recognition*. https://doi.org/10.1109/CVPR.2003.1211516.

Theiler, P. W., J. D. Wegner and K. Schindler. 2014. Keypoint-based 4-points congruent sets–Automated marker-less registration of laser scans. *ISPRS Journal of Photogrammetry and Remote Sensing* 96(Oct.):149–163.

Vo, A.-V., L. Truong-Hong, D. F. Laefer and M. Bertolotto. 2015. Octree-based region growing for point cloud segmentation. *ISPRS Journal of Photogrammetry Remote Sensing* 104(Jun.):88–100.

Von Hansen, W. 2006. Robust automatic marker-free registration of terrestrial scan data. *Proceedings of Photogrammetry and Computer Vision* 36:105–110.

Wang, Y. and J. Solomon. 2015. Deep closest point: Learning representations for point cloud registration. *Proceedings of the International Conference on Computer Vision.* https://doi.org/10.48550/arXiv.1905.03304.

Wang, Y., Y. Ma, A. X. Zhu, H. Zhao and L. Liao. 2018. Accurate facade feature extraction method for buildings from three-dimensional point cloud data considering structural information. *ISPRS Journal of Photogrammetry Remote Sensing* 139:146–153.

Yang, B., Z. Dong, F. Liang and Y.J.I.J.o.P. Liu. 2016. Automatic registration of large-scale urban scene point clouds based on semantic feature points. *ISPRS Journal of Photogrammetry and Remote Sensing* 113(Mar.):43–58.

Yuan, W., B. Eckart, K. Kim, V. Jampani, D. Fox and J. Kautz. 2020. Deepgmr: Learning latent gaussian mixture models for registration. Pages 733–750 in *Proceedings of the European Conference on Computer Vision*, Cham: Springer. https://doi.org/10.1007/978-3-030-58558-7_43.

Zolanvari, S., D. F. Laefer and A. S. Natanzi. 2018. Three-dimensional building faade segmentation and opening area detection from point clouds. *ISPRS Journal of Photogrammetry Remote Sensing* 143(SEP.):134–149.

The Simulation and Prediction of Land Surface Temperature Based on SCP and CA-ANN Models Using Remote Sensing Data: A Case Study of Lahore

Muhammad Nasar Ahmad, Shao Zhengfeng, Andaleeb Yaseen, Muhammad Nabeel Khalid, and Akib Javed

Abstract

Over the last two decades, urban growth has become a major issue in Lahore, accelerating land surface temperature (LST) rise. The present study focused on estimating the current situation and simulating the future LST patterns in Lahore using remote sensing data and machine learning models. The semi-automated classification model was applied for the estimation of LST from 2000 to 2020. Then, the cellular automata-artificial neural networks (CA-ANN) module was implemented to predict future LST patterns for 2030 and 2040, respectively. Our research findings revealed that an average of 2.8 °C of land surface temperature has increased, with a mean LST value from 37.25 °C to 40.10 °C in Lahore during the last two decades from 2000 to 2020. Moreover, keeping CA-ANN simulations for land surface temperature, an increase of 2.2 °C is projected through 2040, and mean LST values will be increased from 40.1 °C to 42.31 °C by 2040. The CA-ANN model was validated for future LST simulation with an overall Kappa value of 0.82 and 86.2% of correctness for the years 2030 and 2040 using modules for land-use change evaluation. The study also indicates that land surface temperature is an important factor in environmental changes. Therefore, it is suggested that future urban planning should focus on urban rooftop plantations and vegetation conservation to minimize land surface temperature increases in Lahore.

Introduction

The land surface temperature has increased globally as a result of increasing urbanization and substantial land-use change. Land surface temperature (LST) is accelerated due to both natural and artificial events and overstresses our environmental system (Girma *et al.* 2022; Zhu *et al.* 2022). Due to rapid urbanization and infrastructure development, most of the vegetation and farmland have been converted into urban centers, escalating the land surface temperature (Naikoo *et al.* 2022; Zhou *et al.* 2021). According to El-Hattab *et al.* (2018) as a result of the expansion of metropolitan regions, LST will increase and more greenery will be converted into man-made infrastructure in the future.

The LST patterns give useful information about the environment and help in understanding climate change (Cai *et al.*, 2018; Sadiq Khan *et al.* 2020). The land surface temperature has an impact on the oceans, weather patterns, plants, and animals that cause ecological uncertainties (Nath *et al.* 2021). But an increase in land surface temperature, especially in urban centers, has a more severe effect on humans and our ecosystem. An increase in LST causes more droughts, melting glaciers, rising sea levels, and changes in snow patterns. Over the previous few decades, megacities have become urban heat islands (UHI) rapidly because of commercial activities, deforestation, and greenhouse gas emission (Rehman *et al.* 2021).

The importance of land surface temperature is rapidly being recognized, and there is growing interest in developing approaches for retrieving LST from satellite remote sensing data. Remote sensing data and GIS technology have provided a wide range of computational modelling for researchers to perform LST development research. Remote sensing technology advancements combined with machine learning and artificial intelligence technologies (Abbas *et al.* 2021; Hamedianfar *et al.* 2020; Talukdar *et al.* 2020) provided prompt and valuable results. Researchers have used a wide range of prediction models (Ghalehteimouri *et al.* 2022; Zhang *et al.* 2022) to predict future LST; for example, Markov Chain, Artificial Neural Network (ANN), cellular automata (CA), and FBprophet. However, CA is a popular and widely used artificial intelligence model and was found to be more reliable in simulating future LST patterns (Al-Darwish *et al.* 2018; Guidigan *et al.* 2019). The cellular automata model works by automatically computing cells based on transitional rules, and algorithmic equations to simulate complex systems such as LST change dynamics in cities (Khan *et al.* 2022; Shafizadeh-Moghadam *et al.* 2021; Zhang and Wang 2021).

This study implemented semi-automatic classification (SCP) and ANN algorithm-based CA models in Quantum Geographic Information System (QGIS) to estimate and predict the LST in the study area. Lahore's surface temperature has risen significantly in recent years (Imran and Mehmood 2020; Mumtaz *et al.* 2020) which has resulted in major environmental issues. As Lahore is Pakistan's fast-rising economic capital, it is confronted with various environmental and socioeconomic complications (Anjum *et al.* 2021). Many studies have been undertaken in the past by researchers for better environmental planning and development (Hussain and Nadeem 2021) in Lahore.

Lahore has significant vegetation loss as a result of urbanization and population growth, resulting in environmental deterioration and a regional rise in temperature. Although the city faces many challenges, including a lack of urban development policies, an increasing population, and rising LST. This study aims to estimate current LST for the years 2000, 2010, and 2020, as well as to model LST trends for the years 2030 and 2040, respectively. This research work has two main goals: (i) assessment of land surface temperature and future projections and (ii) implementation of SCP and CA-ANN models to evaluate LST patterns. This study is noteworthy since no one has before implemented the SCP-machine learning and modules for land-use change evaluation (MOLUSCE) models to predict the land surface temperature in Lahore.

Muhammad Nasar Ahmad, Shao Zhengfeng, Andaleeb Yaseen, and Akib Javed are with the State Key Laboratory of Information Engineering in Surveying, Mapping and Remote Sensing, Wuhan University, Wuhan 430079, China (mnasarahmad@whu.edu.cn).

Muhammad Nabeel Khalid is with the College of Earth and Environmental Sciences, University of the Punjab, Lahore 54900, Pakistan.

Contributed by Hongyan Zhang, April 18, 2022 (sent for review July 4, 2022; reviewed by Russell G. Congalton, Hongping Zhang).

Photogrammetric Engineering & Remote Sensing
Vol. 88, No. 12, December 2022, pp. 783–790.
0099-1112/22/783–790

doi: 10.14358/PERS.22-00071R2

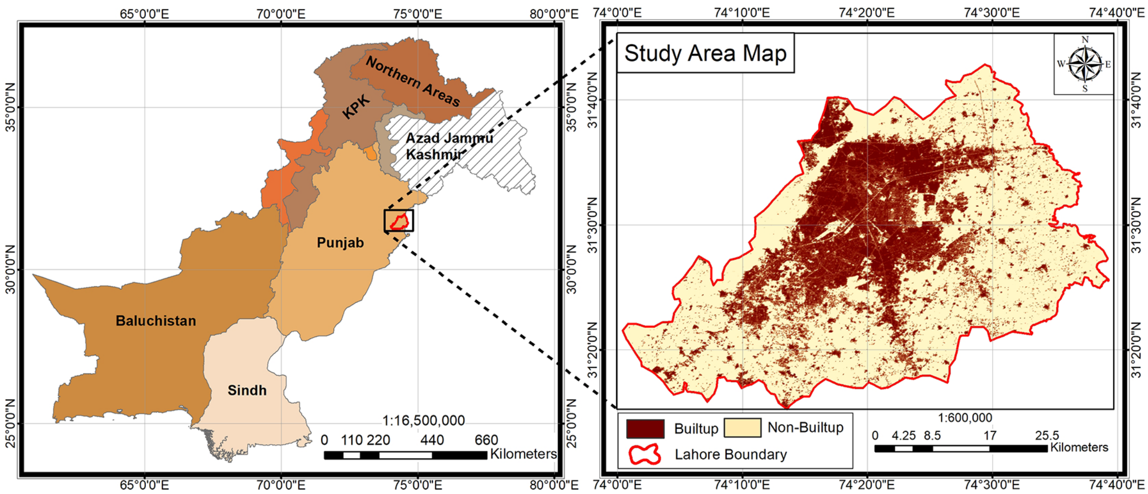

Figure 1. Location of the study area on the map.

Study Area

Lahore is the capital of Punjab province and the second-largest city in terms of population. Lahore is located in the northeast area of Punjab, Pakistan, and has a population of around 12 642 000 people. It is situated at 31° 34' 55.36" N latitude and 74° 19' 45.75" E longitude. Lahore has an area of around 1772 square kilometers and is located at an elevation of 217 m above mean sea level. Figure 1 shows the extent of the study area on the map. Lahore has hot and humid weather conditions with a mean maximum temperature of 40.4 °C and the mean lowest temperature is 27.4 °C in June. The city has transformed into a technology hub, with substantial economic, industrial, and trade opportunities.

In terms of weather, Lahore experiences extreme temperatures during the summer season and low temperatures during the winters. In the summer season, the highest temperatures were recorded in the months of May, June, and July. The lowest temperatures are usually recorded in December and January. The monthly rainfall and mean temperature indices are further explained in Figure 2. Generally, humidity and rainfall were found to be key components of climate change. And because rainfall is the most basic component of the climate, its occurrence primarily lowers the general temperature, while its absence for an extended period of time raises the temperature.

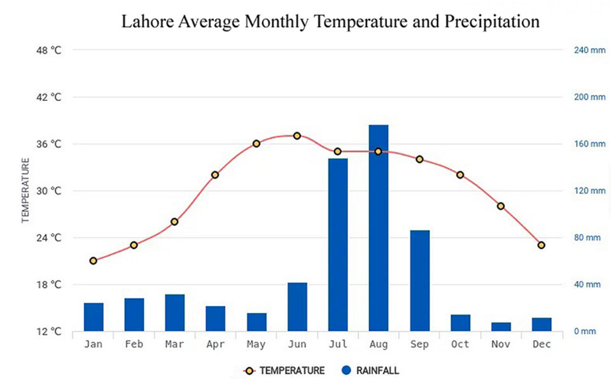

Figure 2. Lahore average monthly temperature and precipitation.

Materials and Methodology

Data Set and Workflow Diagram

To accomplish the research objectives, multispectral satellite images and vector data sets were downloaded and processed to perform analysis work. Table 1 and Table 2 show the details of the data sets used in this study. *Landsat 5* has a thermal band-6 and has a spatial resolution of 120 meters, although United States Geological Survey (USGS) down samples the resolution to 30-meter pixels. Similarly, *Landsat 8* has two thermal bands (band-10, and band-11) with a spatial resolution of 100 meters.

Data Flow Diagram and Methodology

The EarthExplorer platform was used to retrieve multi-temporal Landsat satellite data from the USGS website; characteristics of the data sets, such as scene ID, sensors, and path/row, are presented in Table 1., Landsat data for the Lahore district was obtained from 2000 to 2020. *Landsat 5* Thematic Mapper was used for the years 2000 and 2010, which were acquired in March, while *Landsat 8* Operational Land Imager was used for the year 2020, which was acquired in January. For each Landsat product, cloud coverage was reduced to less than 10% to increase data precision for more accurate LST change detection. The Shuttle Radar Topography Mission Digital Elevation Model (SRTM *DEM*) (version 3) was also obtained from the USGS website and used as an independent variable. Below, Figure 3 shows the overall workflow diagram for this research.

Table 1. Satellite data set used in this study.

No.	Sensor ID	Sensor Type	Acquisition Date	Row/ Path	Spatial Resolution
1	LT05149038200003110IT1	TM	11 March 2000	149/038	30 m
2	LT05149038201003060IT1 Band 6 (Thermal)	TM	07 March 2010	149/038	30 m 120 (30) m
3	LC08149038202002150IRT Band 10, Band 11 (Thermal)	OLI/TIRS	15 February 2020	149/038	30 m 100 m
4	SRTM DEM	ASTER-V3	23 September 2014	N31/E074	30 m

Source: NASA/USGS-Earth Explorer (https://earthexplorer.usgs.gov/).
TM = Thematic Mapper; OLI = Operational Land Imager; TIRS = Thermal Infrared Sensor;
SRTM DEM = Shuttle Radar Topography Mission Digital Elevation Model.

Table 2. Details of vector data set used.

No.	Name	Geometry Type	Datum	Coordinate System
1	Country and City Boundary	Polygon	D_WGS_1984	UTM_Zone_43N
2	Roads	Polyline	D_WGS_1984	UTM_Zone_43N
3	Waterways	Polyline	D_WGS_1984	UTM_Zone_43N
4	River	Polygon	D_WGS_1984	UTM_Zone_43N

Source: Lahore Development Authority (https://www.lda.gop.pk).

The satellite data were preprocessed for atmospheric correction and clipping according to the study area boundary. Therefore, the vector boundary of the Lahore district was used to clip both the satellite images and *DEM*. After that, thermal bands for each Landsat product were provided as input to the SCP model, which used Equation 2 to calculate the LST.

Furthermore, a few dependent variables such as roads, waterways, and water bodies have been added to the MOLUSCE simulation model to improve prediction accuracy. Therefore, vector data from the Lahore Development Authority sector was acquired and used as a spatial variable in the cellular automata model.

Semi-Automatic Classification Module

In previous research work, a variety of image processing software such as ERDAS Imagine, ENVI, Catalyst, GEOMATICA, and ArcGIS were used. In this study, a semi-automatic classification (SCP) tool in QGIS was used for LST estimation. Then, satellite data from 2000 to 2020 was used, and thermal bands from each Landsat product were used to estimate LST. The Semi-Automatic Categorization Plugin is a free and open-source QGIS application that allows users to classify remote sensing data in both supervised and unsupervised modules.

The SCP is a robust approach, particularly for estimating LST (Dhar *et al.* 2019) and Land Use/Land Cover (LULC). SCP permits the use of

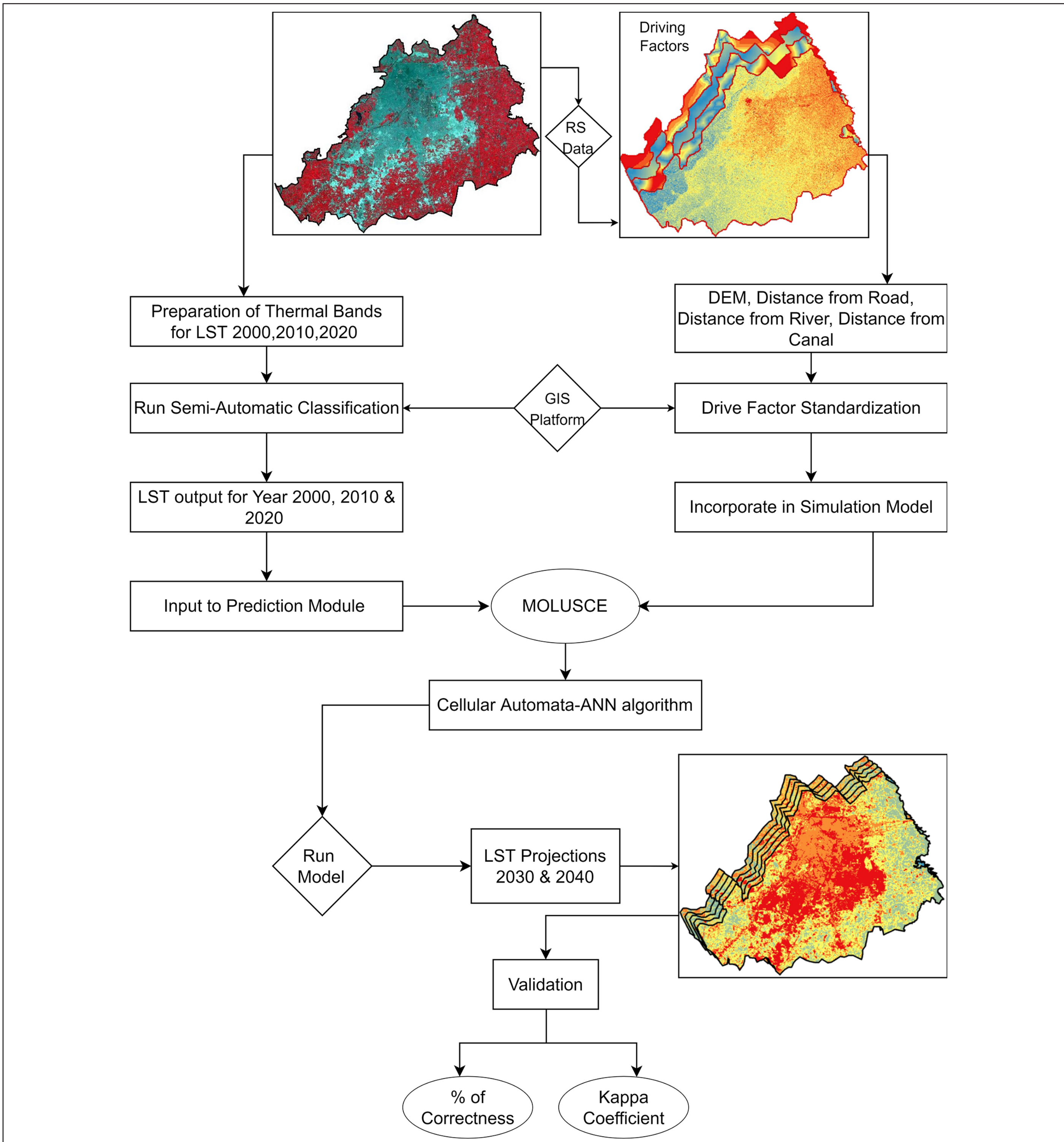

Figure 3. Overall data flow diagram.

a variety of classification methods based on satellite images such as MODIS, Landsat, and S2 (*Sentinel-I*, *Sentinel-II*). It also includes several tools for image preprocessing, such as satellite data download and radiometric corrections (Islam *et al.* 2021; Maung and Sasaki 2021; Riad *et al.* 2020). SCP also supports postprocessing operations such as class merging, accuracy assessment, and conversion from a classified raster to a vector.

The semi-automatic processing tool provides preprocessing of satellite data; it transforms the satellite band's digital numeric values into reflectance values. It also has an automated Dark Object Subtraction machine-learning technique for determining the darkest pixel value in each band for atmospheric adjustments. The SCP image processing method distinguishes image components based on their spectral signatures and uses a Region Growing Algorithm (RGA) for training area selection. The RGA chooses pixels that were spectrally equivalent to a seed one, taking into consideration spectral similarity, i.e., the spectral distance of surrounding pixels.

SCP includes numerous classification algorithms, such as (i) Minimum Distance, (ii) Maximum Likelihood, (iii) Spectral Angle Mapper, (iv) Parallelepiped Classification, (v) Land Cover Signature Classification, and (vi) Algorithm Raster. However, the Spectral Angle Mapper (SAM) method is the most widely used for LULC and LST estimation, and it also processes hyperspectral data. The SAM classifier works by determining the spectral value of a pixel using angular information (Hoque *et al.* 2022; Nappo *et al.* 2021). It calculates the angle between pixel spectral signatures and training signatures.

Conversion of DN to Reflectance

The Landsat products have thermal bands; for example, *Landsat 5* has band-6 and for *Landsat 8*, band-10 and band-11 are thermal bands. There was a need to convert their digital number (DN) value to reflectance. Following Equation 1 (Dong *et al.* 2022; John *et al.* 2021; Lan *et al.* 2021) was used for this conversion. In addition, the Planck curve equation has been used to calculate the brightness temperature in Kelvin acquired from spectral radiance (Equation 1).

$$TB = K2/[(K1/\ L\lambda) + 1] \tag{1}$$

where $K1$ (in watts/meter squared), $K2$ (in Kelvin) were the constants and $L\lambda$ was the Spectral Radiance (Congedo 2016). The $K1$ and $K2$ constants for each Landsat sensor were presented in Table 3; all these constant values were available in the satellite image metadata (MTL) file.

Table 3. Constants for Landsat products regarding thermal bands.

		Landsat 8	
Constants	Landsat 5	Band 10	Band 11
*K*1	607.76	774.89	1321.08
*K*2	1260.56	480.89	1201.14

Estimation of Land Surface Temperature

The LST has a vast expression that refers to the combined temperature of all objects on Earth. In recent research, it has been shown that the estimation of land surface temperature can be calculated using the following Equation 2 (Gohain *et al.* 2021; S. Hussain and Karuppannan 2021; Sekertekin and Zadbagher 2021). We have used Equation 1 and Equation 2 for estimating LST based on pre-defined values explained in Table 3 for all the Landsat thermal bands. The SCP tool can perform these computations automatically. Figure 4 shows the step-by-step procedure of calculating LST using a semi-automatic classification model in QGIS.

$$T = TB/[1 + (\lambda * TB/c2)*(e)] \tag{2}$$

where
λ = wavelength of emitted radiance
$c2 = h * c/s$ = 1.4388 * 10 − 2 m K
h = Planck's constant = 6.626 * 10 − 34 J s
s = Boltzmann constant = 1.38 * 10 − 23 J/K
c = velocity of light = 2.998 * 108 m/s

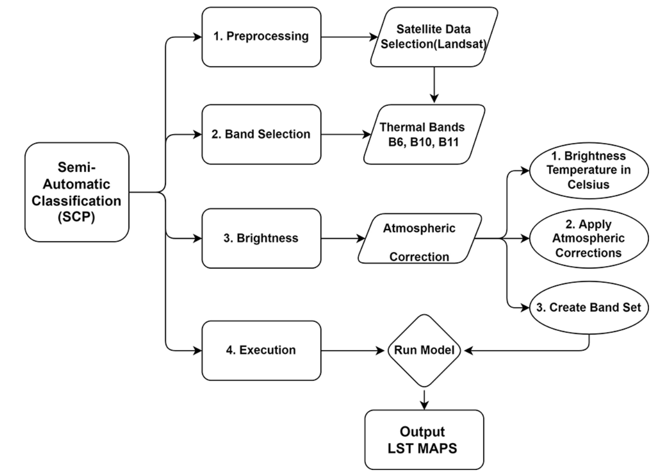

Figure 4. Land surface temperature assessment using semi-automated classification (SCP).

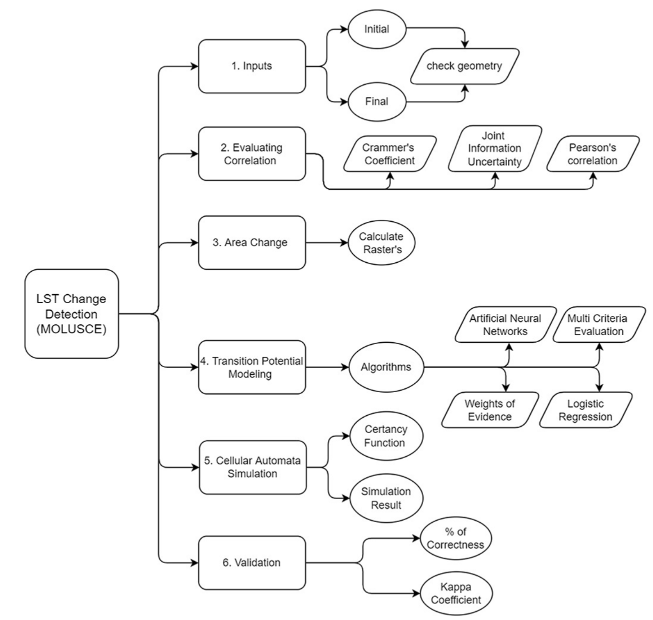

Figure 5. (a) Artificial Neural Network (ANN) model for Land Surface Temperature (LST) future simulations. (b) Model design and steps for future LST projections.

Methods of Land-Use Change Evaluation (MOLUSCE) Simulations

The MOLUSE simulation model was used in this study to evaluate LST for 2030 and 2040 in Lahore. MOLUSCE has an open-source plugin for simulating future trends. It comprises well-known approaches that may be used to analyze the increase in LST. MOLUSCE includes numerous methods for generating transition potential maps (Baig *et al.* 2022; Rehman *et al.* 2022), such as CA-ANN, weights of evidence, logistic regression, and multi-criteria evaluation. Many researchers have described that artificial neural networks (CA-ANN) algorithms can produce more efficient outputs for LULC/LST variations (Abdullah *et al.* 2022; Kafy *et al.* 2022; Mohammad *et al.* 2022; Tolentino and Galo 2021). In this study, we have implemented the CA-ANN model (MOLUSCE) for the future prediction of LST in 2030 and 2040. Figure 5a and 5b show the CA-ANN model constructed for LST estimation.

Dependent Variables Integration in LST Scenarios

Furthermore, some dependent variables were integrated into the MOLUSCE for future LST simulations, such as *DEM*, distance from roads, distance from waterways, and distance from water bodies, respectively. These spatial variable maps shown in (Figure 6) were created in

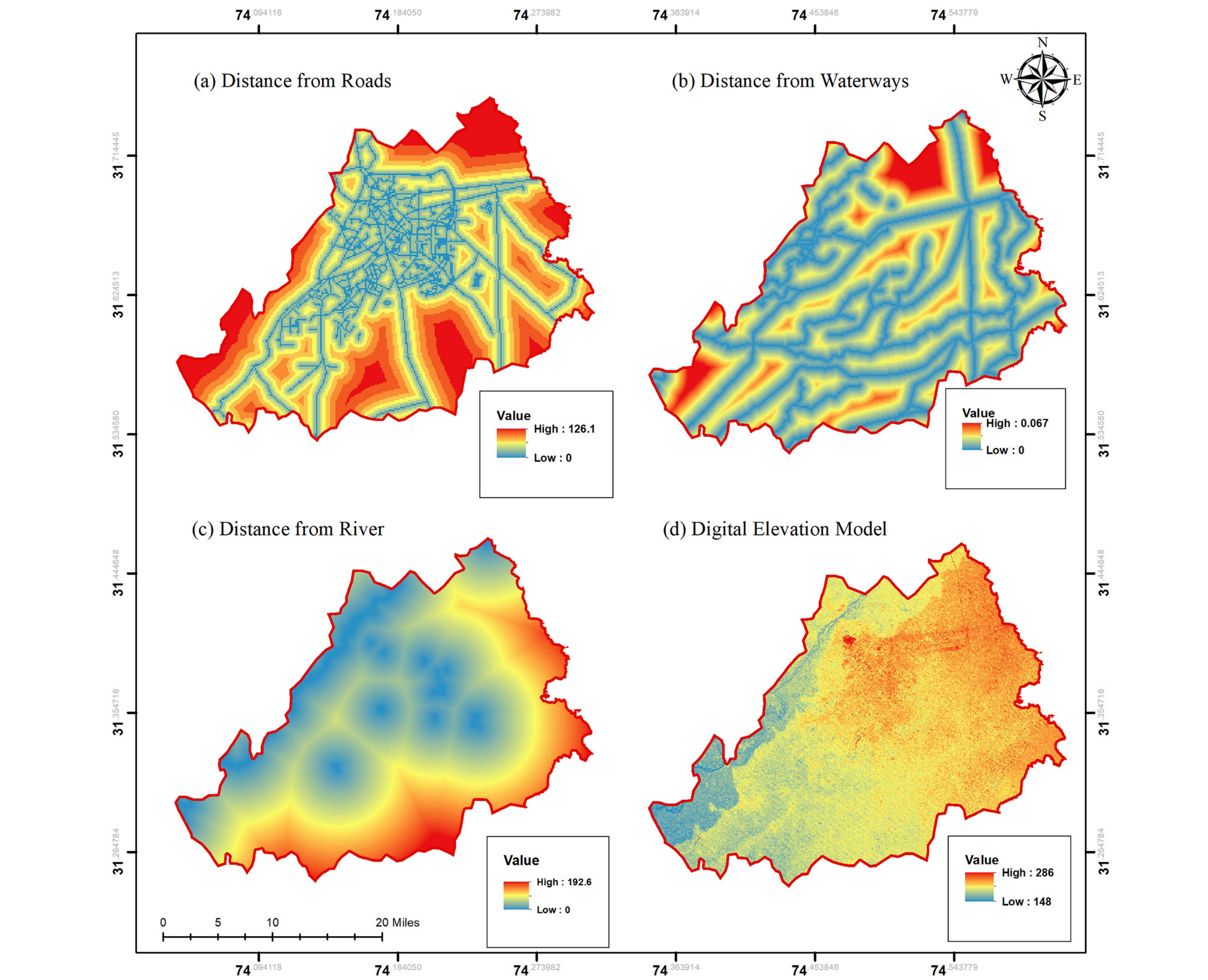

Figure 6. Dependent variables used for future prediction of Land Surface Temperature (LST).

ArcMap using spatial analyst tool extension including Euclidian distance, extract by mask, and reclassify tools. These distance maps have a significant influence on the predicted results using CA-ANN for LST.

Results

This part describes the findings and conclusions for LST historical modelling and future prediction using the methodologies and procedures outlined in the "Materials and Methodology" section. Results revealed that the land surface temperature has increased in Lahore and will rise more in the coming future. The LST's current and future trends were derived using the SAM technique in SCP-QGIS from 2000 to 2040, respectively. According to Gazi *et al.* (2021), SAM can provide more prompt results as compared to maximum likelihood and minimum distance using SCP. Moreover, in CA-ANN, neural network learning curves were constructed between train and validation data for future prediction. These curves can be under-fit, over-fit, and good-fit (Cohen *et al.* 2021; Loureiro *et al.* 2021) which shows the prediction's accuracy (correctness). As one of the artificial intelligence methodologies, CA was found to be a significant model (Hu *et al.* 2022; Mwabumba *et al.* 2022). In this research, the CA-ANN model has accurately forecasted future LST trends in Lahore. The current study revealed that LST has changed significantly over time (2000–2020). LST was calculated first for the years 2000, 2010, and 2020 using the SCP method as used in LULC classification using a combination of remote sensing data and prediction models. Additionally, the CA-ANN model was used for LST prediction modelling for 2030 and 2040, respectively. The LST output maps in Figure 7 and Figure 8 indicate an overall change in land surface temperature from 2000 to 2040. From the results, it can be observed that 2.8 °C land surface temperature has increased in Lahore during the last two decades, and mean LST values have increased from 37.25 °C to 40.10 °C. Similarly, in terms of future perspectives of LST, a change of 2.2 °C from 2020 to 2040 has been projected, and mean LST values will increase from 40.1 °C to 42.31 °C.

It can be noticed from the results that LST has increased in Lahore due to changes in built-up area and degradation in vegetation cover. The MOLUSCE model also provided the overall accuracy and kappa values, indicating a kappa value of 0.82 for projected LST with an 86.2 % correctness rate, as shown in Table 4.

Results obtained using CA-ANN for LST prediction were significant as neural network curves for both 2030 and 2040 showed a good fit. According to Liu *et al.* (2022), best-fit neural network curves have minor gaps for both training and validation data. From the results, it can be validated that LST neural curves have a significant fitting pattern. Furthermore, both the training and validation learning curves were a good fit, as shown in Figure 9 and Figure 10 for 2030 and 2040 respectively.

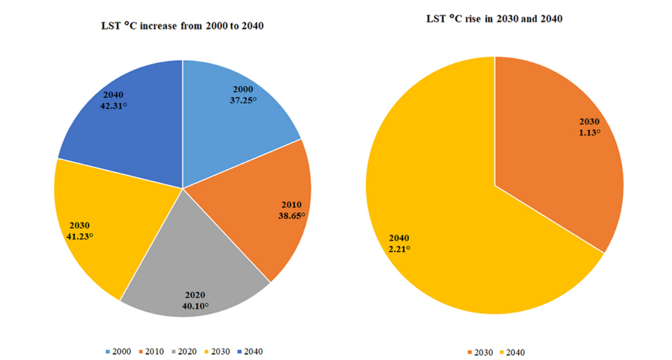

Figure 7. Land Surface Temperature (LST) variation 2000–2020 and future prediction of 2030 and 2040.

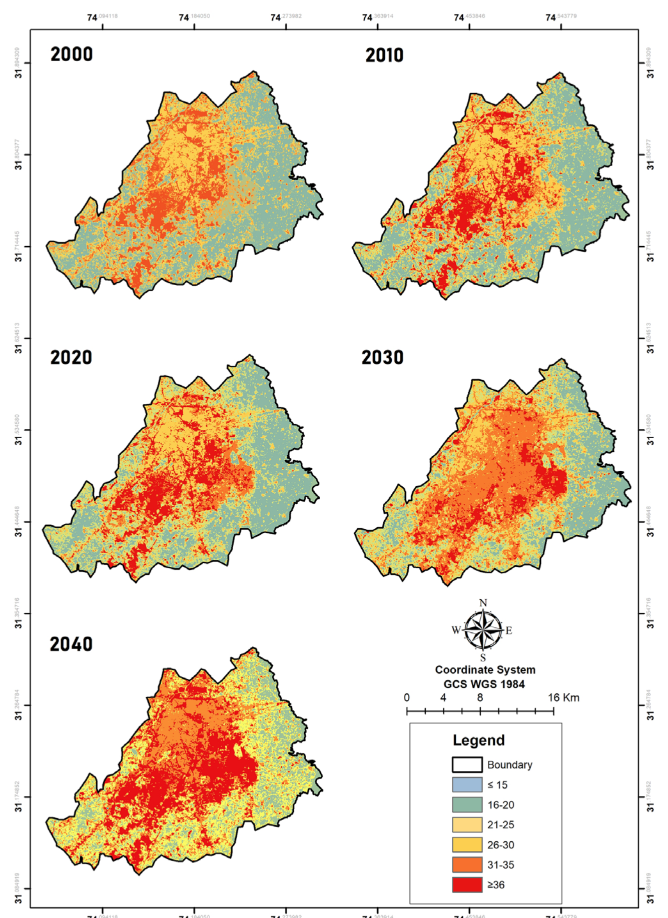

Figure 8. Historical Land Surface Temperature (LST) and simulated LST for 2030 and 2040 using cellular automata-artificial neural networks (CA-ANN).

Table 4. Land Surface Temperature (LST) simulation overall accuracy and Kappa coefficient in 2030 and 2040, respectively.

Year	2030	2040	Average (%)
% of Correctness	84.16	88.31	86.2
Kappa (Overall)	0.79	0.85	0.82
Kappa (histogram)	0.90	0.91	0.90
Kappa (location)	0.85	0.87	0.86

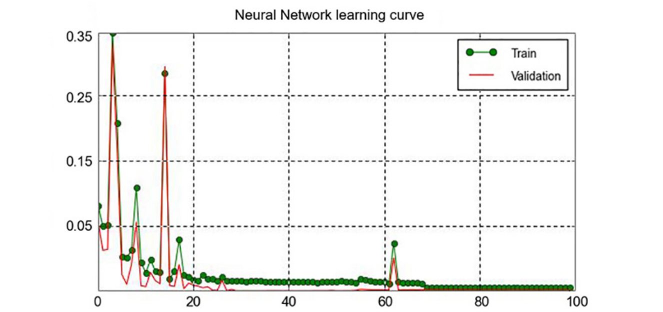

Figure 9. Neural network curve for Land Surface Temperature (LST) prediction 2030 (Good-fit).

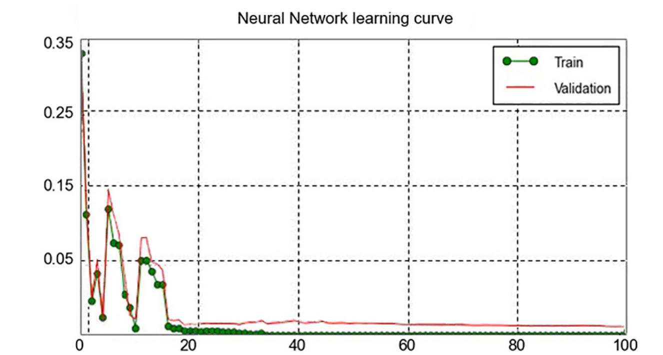

Figure 10. Neural network curve for Land Surface Temperature (LST) prediction 2040 (Good-fit).

Discussion

The foremost reason for this significant increase in LST was the conversion of vegetative land into built-up areas, and also construction through concrete and asphalt material. According to our findings, LST was impacted owing to the deterioration of vegetation and water supplies, which might lead to further socio-economic complications in the coming years. Furthermore, the growth of the Lahore metropolitan region increased in high-temperature zones, and if this trend continues, the city will become a UHI in the future. This study suggested that effective land management plans and policies must be developed and implemented to manage future LST scenarios. According to the analysis of the multi-temporal LST maps, both biophysical and socio-economic parameters were found to have a greater impact on surface temperature in the study area. Moreover, this study also recommends that recent infrastructure developments, housing societies, and industrial zones demolish the natural vegetation cover and also increase the land surface temperature in Lahore. Moreover, extreme land surface temperature was observed on impervious surfaces that have a high capacity for heat absorption and radiation. The principal causes of high temperatures (Ahmad *et al.* 2022) in Lahore were heat emissions from industries and vehicles due to more rapid urbanization in recent decades. Although, Lahore confronted multiple challenges including energy consumption crises, clean water scarcity, urbanization, population growth, and smog. But this research mainly aims to monitor LST from 2000 to 2040. These outcomes and findings can assist city planners in land-use planning, vegetation and agricultural land conservation, and environmental sustainability.

Conclusions

The core objective of this research work was to analyze the historical LST rise and then simulate the future LST scenarios in Lahore using remote sensing data. We have implemented the CA-ANN algorithm using the MOLUSCE tool for future prediction, and a machine learning-based model SCP was adopted for the LST estimation. Our research findings revealed that 2.8 °C of land surface temperature has been increased, with a mean LST value from 37.25 °C to 40.10 °C, in Lahore during the last two decades from 2000 to 2020. It is also concluded that, keeping CA-ANN predictions for LST, an increase of 2.2 °C is projected for 2040, with mean LST values (40.1 °C to 42.31 °C). The CA-ANN model was validated for future LST simulation with an overall Kappa value of 0.82 and 86.2 % of correctness for the years 2030 and 2040 using MOLUSCE. According to the simulation results, the conversion of vegetation into built-up areas and LST will continues to rise more in the coming years. It can be concluded that this study can help in better preparedness for land-use planning of Lahore, and rooftop plantations and conservation of existing greenery can help in controlling LST in the future. Government sectors can also achieve regulated urban expansion and controlled LST in Lahore by maintaining ecological and agricultural land in the study area.

Acknowledgments

The authors would like to express their gratitude to the municipal and provincial governments for supplying the statistics data. Satellite imagery is publicly available for researchers, in addition to the USGS and NASA. The authors would like to thank the anonymous reviewers for their insightful remarks and manuscript improvement recommendations.

All individuals who fit the criteria for authorship were identified as authors, and all authors confirm that they have contributed sufficiently to the work to assume public responsibility for the content, including participation in the concept, design, analysis, writing, or modification of the publication. In addition, each author swears that this or comparable content has not been submitted to or published in any other journal.

References

Abbas, Z., G. Yang, Y. Zhong and Y. Zhao. 2021. Spatiotemporal change analysis and future scenario of LULC using the CA-ANN approach: A case study of the greater bay area, China. *Land* 10(6):584.

Abdullah, S., D. Barua, S. Abdullah, M. Abubakar and Y. W. Rabby. 2022. Investigating the impact of land use/land cover change on present and future land surface temperature (LST) of Chittagong, Bangladesh. *Earth Systems and Environment* 1–15.

Ahmad, M. N., Q. Cheng and F. Luo. 2022. dynamic linkage between urbanization, electrical power consumption, and suitability analysis using remote sensing and GIS techniques. *Photogrammetric Engineering & Remote Sensing* 88(3):171–179.

Al-Darwish, Y., H. Ayad, D. Taha and D. Saadallah. 2018. Predicting the future urban growth and it's impacts on the surrounding environment using urban simulation models: Case study of Ibb city–Yemen. *Alexandria Engineering Journal* 57(4):2887–2895.

Anjum, M. S., S. M. Ali, M. A. Subhani, M. N. Anwar, A.-S. Nizami, U. Ashraf and M. F. Khokhar. 2021. An emerged challenge of air pollution and ever-increasing particulate matter in Pakistan; a critical review. *Journal of Hazardous Materials* 402:123943.

Baig, M. F., M. R. U. Mustafa, I. Baig, H. B. Takaijudin and M. T. Zeshan. 2022. Assessment of land use land cover changes and future predictions using CA-ANN simulation for Selangor, Malaysia. *Water* 14(3):402.

Cai, M., C. Ren, Y. Xu, K. K.-L. Lau and R. Wang. 2018. Investigating the relationship between local climate zone and land surface temperature using an improved WUDAPT methodology–A case study of Yangtze River Delta, China. *Urban Climate* 24, 485–502.

Cohen, O., O. Malka and Z. Ringel. 2021. Learning curves for overparametrized deep neural networks: A field theory perspective. *Physical Review Research* 3(2):23034.

Congedo, L. 2016. Semi-automatic classification plugin documentation. *Release* 4(0.1):29.

Dhar, R. B., S. Chakraborty, R. Chattopadhyay and P. K. Sikdar. 2019. Impact of land-use/land-cover change on land surface temperature using satellite data: A case study of Rajarhat Block, North 24-Parganas District, West Bengal. *Journal of the Indian Society of Remote Sensing* 47(2):331–348.

Dong, Y., Z. Ren, Y. Fu, N. Hu, Y. Guo, G. Jia and X. He. 2022. Decrease in the residents' accessibility of summer cooling services due to green space loss in Chinese cities. *Environment International* 158:107002.

El-Hattab, M., S. M. Amany and G. E. Lamia. 2018. Monitoring and assessment of urban heat islands over the Southern region of Cairo Governorate, Egypt. *The Egyptian Journal of Remote Sensing and Space Science* 21(3):311–323.

Gazi, M., M. Rahman, M. Uddin and F. M. Rahman. 2021. Spatio-temporal dynamic land cover changes and their impacts on the urban thermal environment in the Chittagong metropolitan area, Bangladesh. *GeoJournal* 86(5):2119–2134.

Ghalehteimouri, K. J., A. Shamsoddini, M. N. Mousavi, F.B.C. Ros and A. Khedmatzadeh. 2022. Predicting spatial and decadal of land use and land cover change using integrated cellular automata Markov chain model based scenarios (2019–2049) Zarriné-Rūd river basin in Iran. *Environmental Challenges* 6:100399.

Girma, R., C. Fürst and A. Moges. 2022. Land use land cover change modeling by integrating artificial neural network with cellular Automata-Markov chain model in Gidabo river basin, main Ethiopian rift. *Environmental Challenges* 6:100419.

Gohain, K. J., P. Mohammad and A. Goswami. 2021. Assessing the impact of land use land cover changes on land surface temperature over Pune city, India. *Quaternary International* 575:259–269.

Guidigan, M.L.G., C. L. Sanou, D. S. Ragatoa, C. O. Fafa and V. N. Mishra. 2019. Assessing land use/land cover dynamic and its impact in Benin Republic using land change model and CCI-LC products. *Earth Systems and Environment* 3(1):127–137.

Hamedianfar, A., M.B.A. Gibril, M. Hosseinpoor and P.K.E. Pellikka. 2020. Synergistic use of particle swarm optimization, artificial neural network, and extreme gradient boosting algorithms for urban LULC mapping from WorldView-3 images. *Geocarto International*:1–19.

Hoque, M. Z., I. Islam, M. Ahmed, S. S. Hasan and F. A. Prodhan. 2022. Spatio-temporal changes of land use land cover and ecosystem service values in coastal Bangladesh. *The Egyptian Journal of Remote Sensing and Space Science* 25(1):173–180.

Hu, X., F. Liu, X. Li, Y. Qi and J. Zhang. 2022. A novel strategy to assimilate category variables in land-use models based on Dirichlet distribution. *Environmental Modelling & Software*:105324.

Hussain, S. and S. Karuppannan. 2021. Land use/land cover changes and their impact on land surface temperature using remote sensing technique in district Khanewal, Punjab Pakistan. *Geology, Ecology, and Landscapes*:1–13.

Hussain, Z. and O. Nadeem. 2021. The nexus between growth strategies of master plans and spatial dynamics of a metropolitan city: The case of Lahore, Pakistan. *Land Use Policy* 109:105609.

Imran, M. and A. Mehmood. 2020. Analysis and mapping of present and future drivers of local urban climate using remote sensing: A case of Lahore, Pakistan. *Arabian Journal of Geosciences* 13(6):1–14.

Islam, M. R., M.N.I. Khan, M. Z. Khan and B. Roy. 2021. A three decade assessment of forest cover changes in Nijhum dwip national park using remote sensing and GIS. *Environmental Challenges* 4:100162.

John, J., N. R. Chithra and S. G. Thampi. 2021. Assessment of land surface temperature dynamics over the Bharathapuzha River Basin, India. *Acta Geophysica* 69(3):855–876.

Kafy, A.-A., A. Al Rakib, M. A. Fattah, Z. A. Rahaman and G. S. Sattar. 2022. Impact of vegetation cover loss on surface temperature and carbon emission in a fastest-growing city, Cumilla, Bangladesh. *Building and Environment* 208:108573.

Khan, F., B. Das and P. Mohammad. 2022. Urban growth modeling and prediction of land use land cover change over Nagpur City, India using cellular automata approach. In *Geospatial Technology for Landscape and Environmental Management*, 261–282. Singapore: Springer.

Lan, X., E. Zhao, P. Leng, Z.-L. Li, J. Labed, F. Nerry, X. Zhang and G. Shang. 2021. Alternative physical method for retrieving land surface temperatures from hyperspectral thermal infrared data: Application to IASI observations. *IEEE Transactions on Geoscience and Remote Sensing* 60:1–12.

Liu, R., X. Yang, C. Xu, L. Wei and X. Zeng. 2022. Comparative study of convolutional neural network and conventional machine learning methods for landslide susceptibility mapping. *Remote Sensing* 14(2):321.

Loureiro, B., C. Gerbelot, H. Cui, S. Goldt, F. Krzakala, M. Mézard and L. Zdeborová. 2021. Learning curves of generic features maps for realistic datasets with a teacher-student model. *Advances in Neural Information Processing Systems*:34.

Maung, W. S. and J. Sasaki. 2021. Assessing the natural recovery of mangroves after human disturbance using neural network classification and Sentinel-2 imagery in Wunbaik Mangrove Forest, Myanmar. *Remote Sensing* 13(1):52.

Mohammad, P., A. Goswami, S. Chauhan and S. Nayak. 2022. Machine learning algorithm based prediction of land use land cover and land surface temperature changes to characterize the surface urban heat island phenomena over Ahmedabad city, India. *Urban Climate* 42:101116.

Mumtaz, F., Y. Tao, G. de Leeuw, L. Zhao, C. Fan, A. Elnashar, B. Bashir, G. Wang, L. Li and S. Naeem. 2020. Modeling spatio-temporal land transformation and its associated impacts on land surface temperature (LST). *Remote Sensing* 12(18):2987.

Mwabumba, M., B. K. Yadav, M. J. Rwiza, I. Larbi and S. Twisa. 2022. Analysis of land use and land-cover pattern to monitor dynamics of Ngorongoro world heritage site (Tanzania) using hybrid cellular automata-Markov model. *Current Research in Environmental Sustainability* 4:100126.

Naikoo, M. W., A.R.M.T. Islam, J. Mallick and A. Rahman. 2022. Land use/land cover change and its impact on surface urban heat island and urban thermal comfort in a metropolitan city. *Urban Climate* 41:101052.

Nappo, N., O. Mavrouli, F. Nex, C. van Westen, R. Gambillara and A. M. Michetti. 2021. Use of UAV-based photogrammetry products for semi-automatic detection and classification of asphalt road damage in landslide-affected areas. *Engineering Geology* 294:106363.

Nath, B., W. Ni-Meister and R. Choudhury. 2021. Impact of urbanization on land use and land cover change in Guwahati city, India and its implication on declining groundwater level. *Groundwater for Sustainable Development* 12:100500.

Rehman, A., J. Qin, A. Pervez, M. S. Khan, S. Ullah, K. Ahmad and N. U. Rehman. 2022. Land-use/land cover changes contribute to land surface temperature: A case study of the Upper Indus Basin of Pakistan. *Sustainability* 14(2):934.

Rehman, E., M. Ikram, S. Rehman and M. T. Feng. 2021. Growing green? Sectoral-based prediction of GHG emission in Pakistan: A novel NDGM and doubling time model approach. *Environment, Development and Sustainability* 23(8):12169–12191.

Riad, P., S. Graefe, H. Hussein and A. Buerkert. 2020. Landscape transformation processes in two large and two small cities in Egypt and Jordan over the last five decades using remote sensing data. *Landscape and Urban Planning* 197:103766.

Sadiq Khan, M., S. Ullah, T. Sun, A.U.R. Rehman and L. Chen. 2020. Land-use/land-cover changes and its contribution to urban heat Island: A case study of Islamabad, Pakistan. *Sustainability* 12(9):3861.

Sekertekin, A. and E. Zadbagher. 2021. Simulation of future land surface temperature distribution and evaluating surface urban heat island based on impervious surface area. *Ecological Indicators* 122:107230.

Shafizadeh-Moghadam, H., M. Minaei, R. G. Pontius Jr, A. Asghari and H. Dadashpoor. 2021. Integrating a forward feature selection algorithm, random forest, and cellular automata to extrapolate urban growth in the Tehran-Karaj Region of Iran. *Computers, Environment and Urban Systems* 87:101595.

Talukdar, S., P. Singha, S. Mahato, S. Pal, Y.-A. Liou and A. Rahman. 2020. Land-use land-cover classification by machine learning classifiers for satellite observations—A review. *Remote Sensing* 12(7):1135.

Tolentino, F. M. and M. de L.B.T. Galo. 2021. Selecting features for LULC simultaneous classification of ambiguous classes by artificial neural network. *Remote Sensing Applications: Society and Environment* 24:100616.

Zhang, B. and H. Wang. 2021. A new type of dual-scale neighborhood based on vectorization for cellular automata models. *GIScience & Remote Sensing* 58(3):386–404.

Zhang, M., C. Zhang, A.-A. Kafy and S. Tan. 2022. Simulating the relationship between land use/cover change and urban thermal environment using machine learning algorithms in Wuhan City, China. *Land* 11(1):14.

Zhou, Y., M. Chen, Z. Tang and Z. Mei. 2021. Urbanization, land use change, and carbon emissions: Quantitative assessments for city-level carbon emissions in Beijing-Tianjin-Hebei region. *Sustainable Cities and Society* 66:102701.

Zhu, Q., X. Guo, W. Deng, Q. Guan, Y. Zhong, L. Zhang and D. Li. 2022. Land-use/land-cover change detection based on a Siamese global learning framework for high spatial resolution remote sensing imagery. *ISPRS Journal of Photogrammetry and Remote Sensing* 184:63–78.

IN-PRESS ARTICLES

Clement Akumu, Sam Dennis. Exploring the Addition of Airborne Lidar-DEM and Derived TPI for Urban Land Cover and Land Use Classification and Mapping.

Zhigang Deng, Xiwei Fan, Jian Chen. A machine learning method for building height estimation based on Sentinel-2 bi-temporal images.

Ji Won Suh, William B Ouimet. Generation of High-Resolution Orthomosaics from Historical Aerial Photographs using Structure-from-Motion (SfM) and Lidar data.

Muhammad Nasar Ahmad, Zhenfeng Shao, Akib Javed, Fakhrul Islam, Hafiz Haroon Ahmad, Rana Waqar Aslam. The Cellular Automata approach in dynamic modelling of land use change detection and future simulations based on Remote Sensing Data in Lahore Pakistan.

Jordan Bowman, Lexie Yang, Orrin Thomas, Jerry Kirk, Andrew Duncan, David Hughes, and Shannon Meade. UAS Edge Computing of Energy Infrastructure Damage Assessment.

Firat Erdem, Nuri Erkin Ocer, Dilek Kucuk Matci, Gordana Kaplan, and Ugur Avdan. Apricot Tree Detection from UAV-Images Using Mask R-CNN and U-Net.

Batuhan Sariturk, Damla Kumbasar, and Dursun Zafer Seker. Comparative Analysis of Different CNN Models for Building Segmentation from Satellite and UAV Images.

Rabi N. Sahoo, Shalini Gakhar, R.G. Rejith, Rajeev Ranjan, Mahesh C. Meena, Abir Dey, Joydeep Mukherjee, Rajkumar Dhakar, Sunny Arya, Anchal Daas, Subhash Babu, Pravin K. Upadhyay, Kapila Sekhawat, Sudhir Kumar, Mahesh Kumar, Viswanathan Chinnusamy, and Manoj Khanna. Unmanned Aerial Vehicle (UAV)–Based Imaging Spectroscopy for Predicting Wheat Leaf Nitrogen.

Yunus Kaya, Halil İbrahim Şenol, Abdurahman Yasin Yiğit, and Murat Yakar. Car Detection from Very High-Resolution UAV Images Using Deep Learning Algorithms.

Xin Jia, Qing Zhu, Xuming Ge, Ruifeng Ma, Daiwei Zhang, and Tao Liu. Robust Guardrail Instantiation and Trajectory Optimization of Complex Highways Based on Mobile Laser Scanning Point Clouds.

Permanganate Index Variations and Factors in Hongze Lake from Landsat-8 Images Based on Machine Learning

Yan Lv, Hongwei Guo, Shuanggen Jin, Lu Wang, Haiyi Bian, and Haijian Liu

Abstract

The permanganate index (COD_{Mn}), defined as a comprehensive index to measure the degree of surface water pollution by organic matter and reducing inorganic matter, plays an important role in indicating water pollution and evaluating aquatic ecological health. However, remote sensing monitoring of water quality is presently focused mainly on phytoplankton, suspended particulate matter, and yellow substance, while there is still great uncertainty in the retrieval of COD_{Mn}. In this study, the Landsat-8 surface reflectance data set from Google Earth Engine and in situ COD_{Mn} measurements were matched. The support vector regression (SVR) machine learning model was calibrated using the matchups. With the SVR model, this study estimates the COD_{Mn} in Hongze Lake, presents the historical spatiotemporal COD_{Mn} distributions, and discusses the affecting factors of the change trend of the COD_{Mn} in Hongze Lake. The results showed that the SVR model adequately estimated COD_{Mn}, with a sum squared error of 1.49 mg^2/L^2, a coefficient of determination (R^2) of 0.95, and a root mean square error of 0.15 mg/L. CODMn in Hongze Lake was high in general and showed a decreasing trend in the past decade. Huai River, Xinsu River, and Huaihongxin River were still the main sources of oxygen-consuming pollutants in Hongze Lake. The wetland natural reserve near Yugou had a significant effect on reducing COD_{Mn}. This study provides not only a scientific reference for the management of COD_{Mn} in Hongze Lake, but also a feasible scheme for remote sensing monitoring of COD_{Mn} in inland water.

Introduction

With global warming and the intensification human activities, eutrophication has become a worldwide environmental problem. The deterioration of water quality seriously damages the stability of aquatic ecosystem and threatens the safety of domestic and production water. On the global scale, water quality monitoring of rivers and lakes is usually operated by measuring water temperature, pH, dissolved oxygen, chemical oxygen demand (COD_{Mn}), biochemical oxygen demand, ammonia nitrogen, volatile phenol, cyanide, arsenic, copper, lead, zinc, cadmium, mercury, hexavalent chromium, total nitrogen (TN), total phosphorus (TP), fluoride, transparency, chlorophyll a (Chl *a*), and other indicators on-site for water quality evaluation and management (Liu 1985).

At present, the water quality indicators in China are generally determined by sampling on sites in accordance with the national environmental protection standards (GB 3838-2002; Ministry of Ecology and Environment of the People's Republic of China, 2002). COD_{Mn} effectively indicates the pollution of oxidizable substances in water, and the accurate detection of its spatial distribution is of great significance for aquaculture, aquatic environmental health, and ecological early warning. Therefore, COD_{Mn} is an important indicator for water quality (Li *et al.* 2017). Shang *et al.* (2016) studied the temporal and spatial variation of water environmental factors and found that the main environmental influencing factor of benthic functional feeding groups was total nitrogen in spring and summer, and COD_{Mn} was the main environmental influencing factor in autumn. At the same time, COD_{Mn} was also the main environmental factor of temporal and spatial variation of zooplankton (Shang *et al.* 2016; Shang *et al.* 2021). Rao (2015) measured and obtained high-precision and highly sensitive COD_{Mn} in surface water based on spectrophotometry. A comparative study was conducted on the COD_{Mn} load in the Three Gorges Reservoir area of the Yangtze River between the wet and dry seasons (Huang *et al.* 2021) using in situ measurements. The higher the COD_{Mn} was, the more serious the pollution by organic matter and oxidizable inorganic matter was in water, found by mapping the COD_{Mn} distribution in the Tokyo Bay (Kawabe and Kawabe 1997). Jun *et al.* (2017) found that the main pollution factors in the Hailar River were COD_{Mn} and COD by studying the water quality of the river. All the above studies adopted traditional water quality monitoring methods, namely, field water sample collection and laboratory water quality parameters measurement. Such methods are time consuming and laborious. Meanwhile, these methods are difficult for large-scale water quality monitoring due to the limitation of manpower, material resources, weather, and hydrological conditions.

With the development of remote sensing technology, it is possible to realize water quality monitoring at a large-scale using satellite remote sensing. Compared with the traditional methods, remote sensing provides large-scale, quick-access, and dynamic water quality monitoring. Although the Landsat series of satellites were originally designed for land monitoring, their high spatial resolution (30 m) provides a unique opportunity for monitoring inland water environments with strong spatial heterogeneity and thus have become one of the mostly widely used multi-spectral remote sensing data sources for inland water quality monitoring. Tan *et al.* (2015) constructed empirical models of Chl *a* and

Yan Lv is with the School of Remote Sensing and Geomatics Engineering, Nanjing University of Information Science and Technology, Nanjing, China, and the Faculty of Electronic Information Engineering, Huaiyin Institute of Technology, Huaian, China.

Hongwei Guo is with the School of Surveying and Land Information Engineering, Henan Polytechnic University, Jiaozuo, China.

Shuanggen Jin is with the School of Remote Sensing and Geomatics Engineering, Nanjing University of Information Science and Technology, Nanjing, China; the School of Surveying and Land Information Engineering, Henan Polytechnic University, Jiaozuo, China; and the Shanghai Astronomical Observatory, Chinese Academy of Sciences, Shanghai, China (sgjin@shao.ac.cn, sg.jin@yahoo.com).

Lu Wang is with the Jiangsu Hongze Lake Management Office, Huaian, China.

Haiyi Bian is with the Faculty of Electronic Information Engineering, Huaiyin Institute of Technology, Huaian, China.

Haijian Liu is with the Faculty of Humanities, Huaiyin Institute of Technology, Huaian, China.

Contributed by Zhenfeng Shao, June 1, 2022 (sent for review July 28, 2022; reviewed by Md. Enamul Huq, Bin Hu).

Photogrammetric Engineering & Remote Sensing
Vol. 88, No. 12, December 2022, pp. 791–802.
0099-1112/22/791–802

doi: 10.14358/PERS.22-00091R2

total suspended solids concentrations using the *in situ* measured water quality data and spectral data synchronously collected by a handheld spectrometer in the Wabash River and its tributaries in Indiana. Specifically, they estimated Chl *a* concentration using the ratio of the reflection peak in the red-edge band (704 nm) to the absorption valley (677 nm) (coefficient of determination [R^2] = 0.95). The concentration of the total suspended solids was estimated by the logarithm model established using the reflectance of 704 nm and 752 nm ($R^2 = 0.83$) (Tan *et al.* 2015). Yang (2020) used *Landsat-8* images to invert the Chl *a*, COD, total nitrogen, and total phosphorus of the rivers around Hefei City, Anhui, China, and further evaluated the eutrophication of the rivers. By using 30 Landsat images from 1984 to 2015, Ye *et al.* (2019) mapped the interannual variation of the maximum turbidity zone in Hangzhou Bay, China. Keith *et al.* (2018) studied the algal blooms in the Jordan Lake Reservoir with *Landsat-8* images. Lei *et al.* (2020) used Geostationary Ocean Color Imager images to invert the suspended particulate matter concentration in Hongze Lake. Xiong *et al.* (2019) conducted an inversion study on total phosphorus in Hongze Lake by using the images of a moderate-resolution imaging spectroradiometer. He *et al.* (2021) used *Landsat-8* images to invert the total nitrogen, total phosphorus, and Chl *a* in the main stream of the Yangtze River and analyzed the dynamics of the three water quality parameters from 2014 to 2020. Yang *et al.* (2013) mapped the spatial distribution of concentrations of Chl *a*, total nitrogen, total phosphorus, and other nutrients in the Chaohu Lake, China, and analyzed the seasonal variation characteristics of the water quality parameters, which showed that the biomass of algae in Chaohu Lake was first decreased and then increased. The difference in algal biomass between the east and the west of Chaohu Lake was obvious. The concentration of nutrients and Chl *a* in the west of the lake was higher than that in the east due to the influence of upstream catchment (Jiang *et al.* 2010; Yang *et al.* 2013). However, the existing water quality parameters of remote sensing studies were mainly focused on Chl *a*, suspended matter, and yellow substance. There are only a few studies on TN and TP, while the existing studies have rarely studied COD_{Mn}. Therefore, quantifying the spatial and temporal distribution characteristics of COD_{Mn} in the lake is of great importance for the water management department to timely identify water quality disaster.

The remote sensing inversion of water quality based on different concentrations of optically active constituents (OACs) has different inherent optical properties (IOPs), and IOPs determine the apparent optical properties (AOPs) of a water body. Through simulating the relationship between the OACs and the IOPs and AOPs captured by satellite sensors, the concentration of OACs in water can be inverted by remote sensing images. Meanwhile, indirect remote sensing inversion of non-OACs can be realized by using the correlation between OACs and non-OACs. The common methods for remote sensing water quality inversion include mainly the analytical method, empirical method/semiempirical method, and machine learning (Yang 2020; Guo *et al.* 2021). The analytical method is based on bio-optical models, which have strict physical significance and high inversion accuracy. However, in the analytical method, a large number of model parameters need to be input in the modeling process (Yang 2020). Although the empirical method/semiempirical method has better prediction accuracy and faster modeling speed, the models need to be calibrated by a large amount of measured data and are seriously limited by region and time, so the model generalization is poor (Shen *et al.* 2020; Yang 2020). In recent years, with the development of artificial intelligence, more and more studies have applied machine learning for water quality remote sensing monitoring, achieved adequate model performance, and obtained reliable results (Zhang *et al.* 2009; Mountrakis *et al.* 2011; Guo *et al.* 2011; Guo *et al.* 2011; Xu *et al.* 2013; Jindal *et al.* 2014; Tomar and Agarwal 2015; Jing *et al.* 2015; Xu *et al.* 2019; Chen *et al.* 2020; Chen *et al.* 2021; Mohammad 2021). Based on machine learning, Sagan *et al.* (2020) studied the blue-green algae phycocyanin, Chl *a*, dissolved oxygen, specific conductivity, fluorescent dissolved organic matter, turbidity, and pollution/sediments from 2016 to 2018, utilizing over 200 sets of water quality data in eight lakes and rivers in the midwestern United States. The concentrations of TP and TN were predicted by the artificial neural network (ANN) model and the linear regression model based on the OLI data in the Geshlagh reservoir (Vakili and Amanollahi 2020). The support vector regression (SVR) model outperformed random forest and Cubist for coastal water quality estimation, yielding a calibration R^2 of 0.91 and a coefficient of variation (CV) root mean square error (RMSE) of 1.74 mg/m3 (40.7%) for Chl *a* and a calibration R^2 of 0.98 and CV RMSE of 11.42 g/m^3 (63.1%) (Kim *et al.* 2014). The SVM has a good performance for information prediction, especially for small samples (Duan *et al.* 2015; Liang and Yang 2016; Hou *et al.* 2021; Zhou *et al.* 2022).

In this study, the spatial distribution of COD_{Mn} in Hongze Lake is investigated by field sampling. Then *Landsat-8* multispectral image data are obtained from Google Earth Engine (GEE) and matched up with the in situ measured water quality data. The matchups are used to train, compare, and verify the machine learning model for the remote sensing inversion of COD_{Mn} in Hongze Lake. Subsequently, the monthly spatial distributions of COD_{Mn} in 2015 are mapped for analyzing the intra-annual COD_{Mn} variation and the influencing factors. Finally, the spatial and temporal distributions of COD_{Mn} in Hongze Lake from 2013 to 2021 are estimated and the potential influencing factors of the interannual COD_{Mn} variation are systematically analyzed.

Study Area

Hongze Lake is the fourth-largest freshwater lake in China, located between 118°10′–118°52′E and 33°06′–33°40′N. The lake covers an area of 6,853 km^2 and is shallow (with an average depth of 1.35 m and a maximum depth of 4.75 m) (Li *et al.* 2021) (Figure 1). The lake has a transitional climate between the north subtropical zone and the south temperate zone, with an average annual temperature of 16.3°C and an average annual precipitation of 925.5 mm. The rivers entering the lake include Huai River, Xinbian River, Laobian River, Xinsui River, Laosui River, Xuhong River, Huaihongxin River, and Andong River (Qiao *et al.* 2016), among which the Huai River accounts for more than 70% of the total lake inflow (Xun *et al.* 2003). Hongze Lake is not only an important water source for agricultural and industrial activities in northern Jiangsu Province but also an important water transmission line and regulation and storage lake for the eastern route of the South-to-North Water Diversion Project (Gao and Jiang 2012). The safety of its water quality is crucial for the diversion project and the sustainable economic development along the river, the lake, and even the whole Huai River basin (Guo *et al.* 2021). In recent years, affected by silt and lake reclamation, the area of Hongze Lake has been shrinking, and the water quality problem has been prominent (Xun *et al.* 2003; Wu 2018; Fu and Yue 2019; Cai *et al.* 2020). According to the reply to proposal No. 0435 of the fourth session of the twelfth Jiangsu provincial political consultative congress (Suggestions on adjusting and improving the water environmental quality evaluation system of Hongze Lake and other aquifer shallow lakes), Jiangsu Provincial Department of Ecology and Environment 2021, China (http://www.jiangsu.gov.cn/art/2021/6/15/art_59167_9849985.html), the current COD_{Mn} in Hongze Lake is Class III, with the annual average concentration increase of 9.8% year on year. In December 2021, it was mentioned in the Environmental Monthly Bulletin of the Huaian Ecological Environment Bureau that the COD_{Mn} of Hongze Lake was 3.8 mg/L, up 7.5% year on year and down 15.4% from the previous month (Yang 2021).

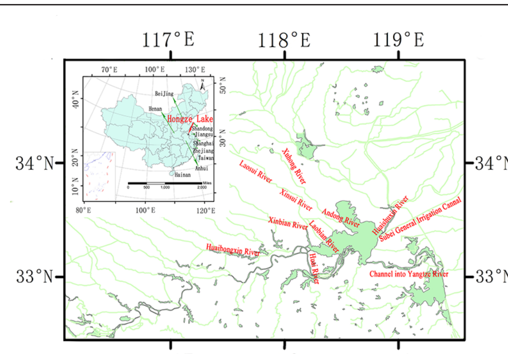

Figure 1. Distribution of the outflow and inflow rivers in Hongze Lake.

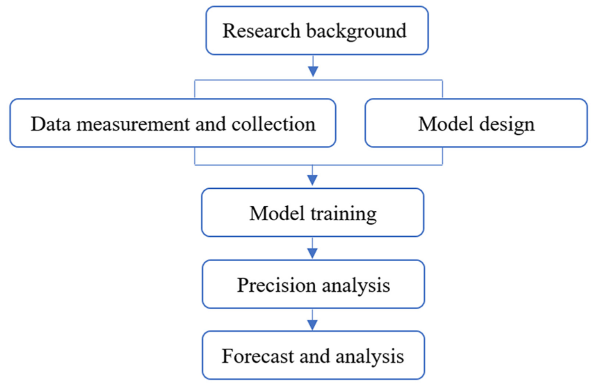

Figure 2. Framework of this study.

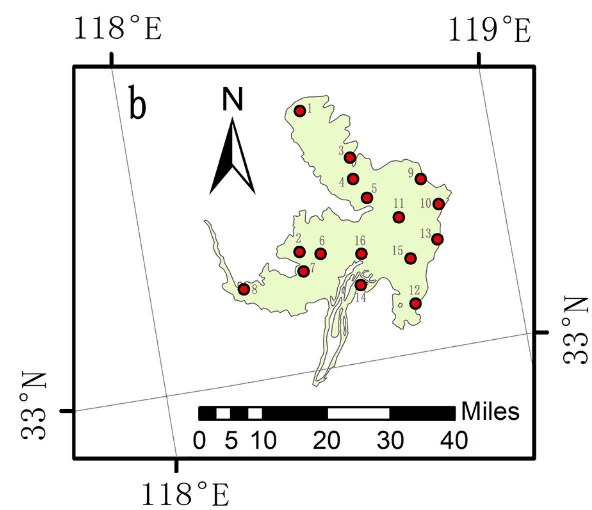

Figure 3. Location of sampling points in Hongze Lake.

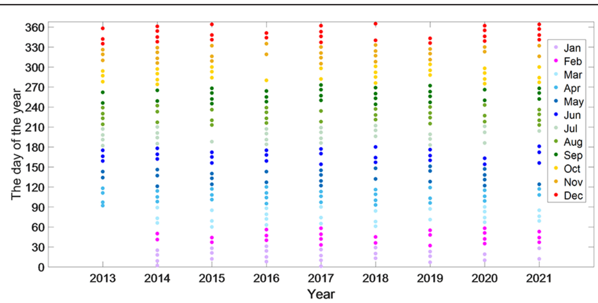

Figure 4. Statistics of satellite transit in the study area from 2013 to 2021.

Table 1. *Landsat-8* image information.

Basic Information		Bands	Bandwidth (μm)	Spatial Resolution (m)
Time horizon	11 April 2013–18 October 2021	Ultrablue	0.435–0.451	30
		Blue	0.452–0.512	30
		Green	0.533–0.590	30
		Red	0.636–0.673	30
Data provider	USGS	Near infrared	0.851–0.879	30
Google Earth Engine ID	LANDSAT/LC08/C02/T1_L2	Shortwave infrared 1	1.566–1.651	30
		Shortwave infrared 2	2.107–2.294	30

Data and Methods

In this study, *Landsat-8* multispectral image data and in situ measured water quality data were collected and then matched up. The matchups were used to build machine learning models and then the permanganate index variations and factors in Hongze Lake were investigated.

In Situ Water Quality Measurements

A total of 16 sampling points were evenly set up over the lake considering lake morphology, hydrodynamics, human activities, and other factors (Figure 3). The water samples were collected in the middle of each month in 2015 with the consistency of the transit time of *Landsat-8*. After being collected, the water samples were quickly stored in amber glass bottles to avoid the sunlight and sent to the laboratory for testing within six hours. The COD_{Mn} testing method followed the standard of the determination of COD_{Mn} of water quality (GB 11892-89, Ministry of Environmental Protection, China, 1990), and the main processing steps were as follows:

1. Sample conservation and delivery: Adding sulfuric acid to the sample to make the pH = 1 to 2 and control the test time within six hours. If the test time exceeds six hours, the test should be kept in a dark place at 0°C to 5°C for no more than two days.
2. Determination of actual samples: Adding a known amount of sulfuric acid (5 ± 0.5 ml) and potassium permanganate solution (10 ml) into the test tube containing the water sample, shake, and place the test tube in a boiling water bath for 30 minutes until the solution is fully reacted. The excess sodium oxalate (10 ml) is added until the solution becomes colorless, and then dropped with the potassium permanganate calibration solution while it is hot until it just appears pink with holding for 30 seconds. The volume of potassium permanganate solution consumed is recorded. Blank test: replacing the sample with 100 ml of water, repeating the steps described above, and recording the volume of potassium permanganate solution consumed.
3. Calculation of concentration: According to Equation 1, the COD_{Mn} concentration of the water sample was finally calculated, represented by mg/L of oxygen, acting as a comprehensive index of the organic pollution degree of the water body:

$$I_{Mn} = \frac{[(10+V_1)\frac{10}{V_2} - 10] * C * 8 * 1000}{100} \quad (1)$$

where V_1 is the volume of potassium permanganate solution consumed during sample titration (ml), V_2 is the volume of potassium permanganate solution consumed during calibration (ml), and C is sodium oxalate standard solution, that is, 0.01 mol/L.

Acquisition and Preprocessing of Remote Sensing Images

Landsat satellite data were used in remote sensing water quality monitoring of inland water (He *et al.* 2021). In this study, the surface reflectance (SR) data set of *Landsat-8* Operational Land Imager (OLI) images from 2013 to 2021 was selected as the data source. *Landsat-8* OLI images consist of five visible and near-infrared bands and two short-wave infrared bands that provide sufficient spectral information to monitor ocean color. The high spatial (30 m) and temporal (16 days) resolutions of the *Landsat-8* OLI satellite support periodic and cost-effective water quality monitoring. The SR data sets of *Landsat-8* OLI were obtained from the GEE platform, which is an immensely powerful and free tool for processing satellite images. The *Landsat-8* OLI SR products in GEE have been atmospherically corrected following the Land Surface Reflectance Code. The satellite transit in the study area is shown in Figure 4. The basis of satellite–earth synchronous screening was that the measured data corresponding to satellite images with cloud coverage of more than 20% or scattered cloud distribution were not used. Through eliminating the outliers of 128 satellite–earth synchronization data, 80 groups of satellite–earth synchronization data were selected for statistical analysis of COD_{Mn} (Figure 5).

Data Analysis

First, by the method of mean value, the overall situation and the monthly variation of the permanganate index in the lake were obtained. According to the match between the *Landsat-8* multispectral image

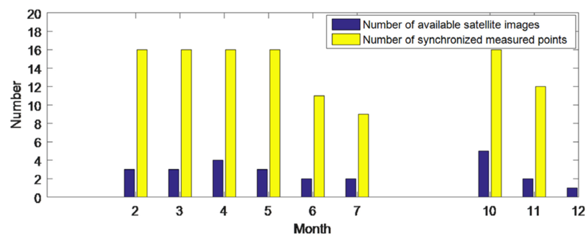

Figure 5. Number of available satellite images and measured data.

data and the in situ measured water quality data, the statistical analysis was carried out month by month and point by point. Finally, data cleaning was performed.

Model Development and Validation

Support Vector Regression

In this study, a machine learning algorithm, namely, the SVR model, was employed to retrieve COD_{Mn} concentrations in Hongze Lake. The SVR algorithm was first proposed by Cortes and Vapnik (1995), mapping x in low-dimensional space to a higher-dimensional characteristic space $\varphi(x)$ to identify a linear regression hyperplane in high-dimensional space that best fits the data (Xu *et al.* 2013; Yu *et al.* 2015). Rooted in statistical learning theory and the structural risk minimization principle, the SVR algorithm was proved to have good performance for handling nonlinear problems (Zhang *et al.* 2009; Andrew 2001). The linear function in the high-dimensional feature space can be expressed as

$$y = w\varphi(x) + b \tag{2}$$

where y is the output, $w\varphi(x)$ is the inner product of the feature space, and $\varphi(x)$ is a nonlinear mapping function. The weight vector w and the bias constant b can be obtained by minimizing the risk function

$$\min\left(\frac{w^2}{2} + \mathrm{C}\sum_{i=1}^{N} L_\mu\left(x_i, y_i, f\right)\right) \tag{3}$$

where w is the Euclidean norm calculation. $L_\varepsilon(xi, yi, f)$ was calculated by the following formula:

$$L_\mu\left(xi, yi, f\right) = \begin{cases} \left|y_i - f\left(x_i\right)\right| - \mu, \left|y_i - f\left(x_i\right)\right| \geq \mu \\ 0, \text{otherwise} \end{cases} \tag{4}$$

where C is the penalty factor and ε is the deviation between the predicted values and the *in-situ* values. To transform the solution of Equation 3 by introducing the relaxation variable ξ_i and ξ_i^* into

$$\min\left(\frac{w^2}{2} + C\sum_{i=1}^{N}\left(\xi_i + \xi_i^*\right)\right) \tag{5}$$

The constraint condition was set as follows:

$$\begin{gathered} y_i - [(w \times x_i) + \mathrm{b}] \leq \varepsilon + \xi_i \\ [(w \times x_i) + \mathrm{b}] - y_i \leq \varepsilon + \xi_i^* \\ \xi_i^*, \xi_i \geq 0 \end{gathered} \tag{6}$$

The Lagrange function was then established to solve the dual problem of the original problem. Based on Equations 5 and 6, the regression function of the optimal hyperplane was finally identified as

$$f\left(\mathrm{x}\right) = \sum_{i=1}^{N}\left(\alpha_i - \alpha_i^*\right)K\left(x_i, x\right) + b \tag{7}$$

where $K(x_i, x)$ is the kernel function. The formula can be expressed as

$$K(x_i, x) = \varphi x_i, x = \varphi(x_i)^T\varphi(x) \tag{8}$$

The common kernel functions include the sigmoid kernel, linear kernel, radial basis function kernel, and polynomial kernel. The calculation formula of each kernel function is

$$\begin{gathered} \text{linear: } K(x_i, x_j) = x_i^T x_j \\ \text{polynomial: } K(x_i, x_j) = (\gamma x_i^T x_j + r)^d, \gamma \succ 0 \\ \text{radial basis function: } K(x_i, x_j) = \exp(-\gamma \| x_i - x_j \|^2), \gamma \succ 0 \\ \text{sigmoid: } K(x_i, x_j) = \tanh(\gamma x_i^T x_j + r) \end{gathered} \tag{9}$$

where γ, r, and d represent the kernel function parameters, respectively. The radial basis function was chosen as the kernel function because it can map to infinite dimensions, the decision boundaries are much more diverse, and it has only one parameter. But the linear kernel is only for linearly separable problems, the polynomial kernel refers to the kernel function expressed in polynomial form. It is a nonstandard kernel function suitable for orthogonal normalized data, and the sigmoid kernel is always used for making a multilayer perceptron neural network.

In this study, the SVR algorithm was implemented by the Libsvm program package of Matlab2016. The modeling parameters are shown in Table 2.

Table 2. Modeling parameters of support vector regression.

Modeling Parameters	C	γ
COD_{Mn}	1.4142	5.65690

Grid Search and k-Fold Cross Validation

According to the SVR principle, penalty coefficient C and kernel function parameter γ play an important role in the performance of the model, and adjusting the two parameters separately may not make the model achieve optimal global effect. Therefore, the grid search method is introduced in this study. Its advantage is that only the range of each hyperparameter needs to be set, and the algorithm will automatically find the optimal solution in the designated hyperparameter grid range. Since grid search is a discretized search for hyperparameters, C and γ are searched in the grid with an exponential range of 2 in this article. Meanwhile, as a semiempirical algorithm, the model performance is closely related to the sample numbers of the training model. For the same group of hyperparameter (C, γ) combinations, when the training sample size changes, the fitting performance of the model will also change.

A k-fold cross-validation method was employed to evaluate the model generalization ability under different hyperparameter combinations (Emhamed and Shrivastava 2021). The implementation process of the cross validation is first to randomly divide the original data set into k parts, among which $k - 1$ is used as the training set and the remaining one is used as the test set to verify the model's prediction ability. The final predicted values of the SVR algorithm were obtained by averaging the above k times results (Fu and Yue 2019). A schematic diagram of k-fold cross validation is shown in Figure 6.

Evaluation Indicators of the Model

The results of the SVR model were assessed using the sum of squared error (SSE), the coefficient of determination (R^2), and the RMSE. SSE is the sum of the squares of the errors between the predicted values and the in situ data. An SEE value closer to 0 indicates that model performance is better. R^2 is used to reflect the proportion of a predicted value explained by independent variables through the model. An R^2 closer to 1 indicates that model performance is better. RMSE represents the root mean square of the error between the predicted values and the *in situ* data. An RMSE closer to 0 means that the model has better performance. The calculation formula of each index is as follows:

$$\mathrm{SSE} = \sum_{i=1}^{n} w_i(y_i - y_i^*)^2 \tag{10}$$

$$R^2 = 1 - \frac{\sum_{i=1}^{n} w_i (y_i^* - y_i)^2}{\sum_{i=1}^{n} w_i (\overline{y_i} - y_i)^2} \tag{11}$$

$$\mathrm{RMSE} = \sqrt{\frac{\sum_{i=1}^{n} w_i (y_i - y_i^*)^2}{n}} \tag{12}$$

In the formula, y_i, y_i^*, and $\overline{y_i}$ are the *in situ* values, predicted value, and mean value of COD_{Mn}, respectively, and w_i and n represent the weight and the number of training samples, respectively.

The technical flowchart of COD_{Mn} retrieval in Hongze Lake based on *Landsat-8* images is shown in Figure 7.

Comparison of Different Machine Learning Modelings

In this study, a back-propagation artificial neural network (BPANN) was employed to compare the performance with the SVR algorithm (Xu *et al.* 2013). Structurally, BPANN is a typical multi-layered forward neural network with one input layer, several hidden layers (either one layer or multiple layers), and one output layer. Full connection is adopted between layers, and there is no mutual connection between neurons in the same layer. It has been proved theoretically that a three-layer network with a hidden layer can approximate any nonlinear function (Yu *et al.* 2015). Neurons in the hidden layer adopted a mostly S-type no-linear transfer function; a Relu activation function was added in each hidden layer. The output layer included two parts: the internal structure and the output result. The BPANN model was built in Matlab, and the structure of the model is shown in Figure 8.

BPNN, also known as BP neural network, is an entry classic neural network model, which can be divided into forward and backward propagation (Yu *et al.* 2015). The idea is to learn a certain number of samples (input and expected output); the sample of each input is sent to the network input layer neurons after being calculated by the hidden layer and the output layer, and each neuron outputs the corresponding predicted value by output the layer (Yu *et al.* 2015). In order to further evaluated the fitting performance of the SVR regression model, this study used a feedforward neural network in the BPANN toolbox of Matlab to conduct a modeling comparison between the training set and the test set. The reflectivity of seven bands was taken as the input layer, the measured value of COD_{Mn} was taken as the output layer, and the hidden layer was set to 1. The BPANN model training results were linearly fitted, and the optimal BPANN model was selected according to the comparison of the R^2, RMSE, and SSE of the fitting function. The optimal modeling results were obtained by setting the number of neurons for testing.

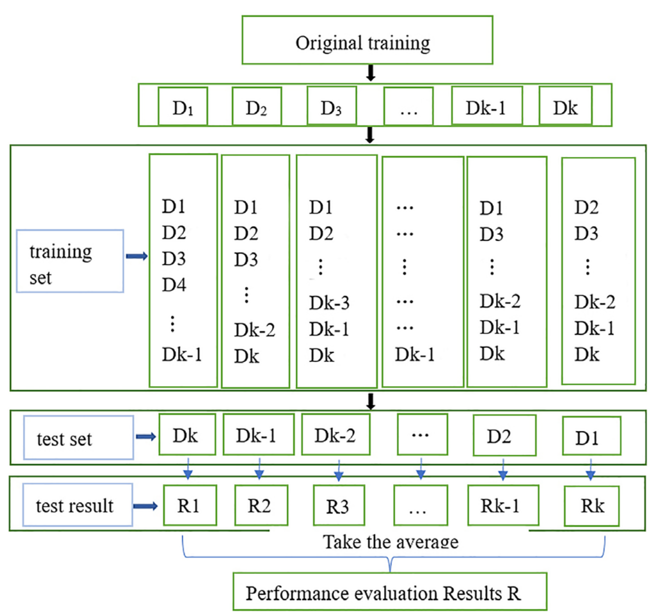

Figure 6. Schematic diagram of *k*-fold cross validation.

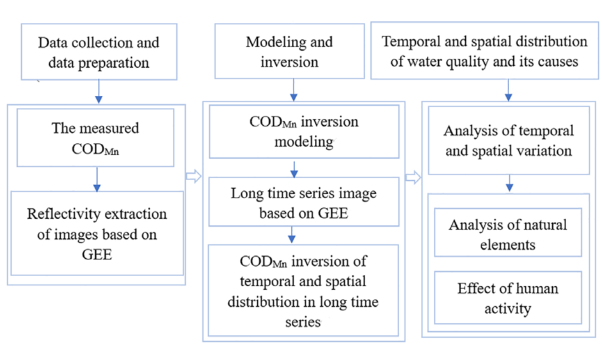

Figure 7. Flowchart of COD_{Mn} retrieval.

Results and Analysis

Analysis of Measured Data

Statistical analysis of COD_{Mn} was conducted at 16 measurement points (Figures 9–11). In general, the distribution of the COD_{Mn} concentrations was uniform. All the sites except Suqian North (the fourth point) have high COD_{Mn} concentrations. COD_{Mn} concentrations were relatively stable in each month of the year. The high values occurred in January and July, and lower values occurred in May and June.

Based on the preliminary data analysis, 128 groups of data were statistically analyzed by SVR, and the data were cleaned according to the deviation between the predicted value and the measured value. Finally, 80 groups of data were selected for SVR statistical regression modeling to improve the modeling accuracy. Analysis of the unselected data shows that the spectral values of all seven bands were on the high side, and the image query found that a small amount of thin cloud existed in the image location corresponding to the measured points. Through the analysis of COD_{Mn} variation with the spectral band, it was found that some unselected points were inconsistent with selected points, which might have been caused by the collection error of measured data. The results show that SVR is suitable for data cleaning.

Optimization of Model Parameters

A grid optimization method was applied to seek the optimal combination of regularization constant and kernel function parameter; the results are shown in Table 3. The model performance was much better in threefold, sixfold, and sevenfold, cross validation than in other folds. Therefore, sixfold cross validation was finally employed for testing the model performance, where the hyperparameters C and γ in the SVR model were obtained as 1.4142 and 5.6569, respectively. The data set was divided

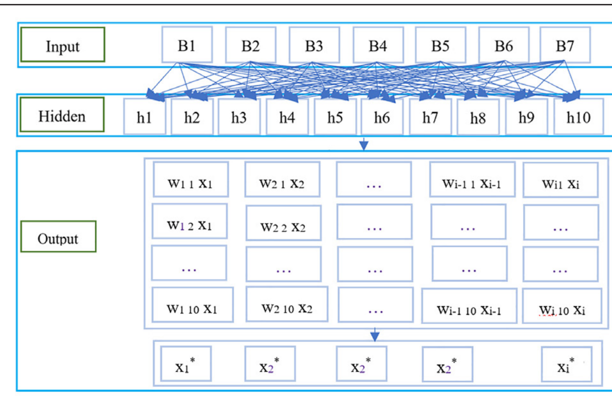

Figure 8. Structure of the BPANN model; the number represents the number of neurons in each layer.

Table 3. Evaluation of support vector regression modeling for different training sets.[a]

k-Folds	SSE	R^2	RMSE	C	γ	*k*-Folds	SSE	R^2	RMSE	C	γ
2	10.49	0.25	0.39	1024	0.002	**7**	**1.10**	**0.97**	**0.13**	**1**	**8**
3	**2.09**	**0.94**	**0.18**	**2**	**4**	8	11.20	0.22	0.41	512	9.7656e-04
4	11	0.23	0.40	724.0773	9.7656e-04	9	5.18	0.84	0.28	2.8284	2
5	8.24	0.71	0.35	1.4142	1.4142	10	5.99	0.81	0.30	2	2
6	**1.49**	**0.95**	**0.15**	**1.4142**	**5.6569**						

SSE = sum of squared error; RMSE = root mean square error.
[a]Bold indicates the setting of the optimal modeling fold for parameters in the test set evaluation.

Table 4. Validation set evaluation of cross-validation attempts to model.[a]

k-Folds	SSE	R^2	RMSE	C	γ
3	0.07	0.88	0.09	2	4
6	**0.06**	**0.88**	**0.09**	**1.4142**	**5.6569**
7	0.13	0.73	0.13	1	8

SSE = sum of squared error; RMSE = root mean square error.
[a]Bold indicates the setting of the optimal modeling fold for parameters in the test set evaluation.

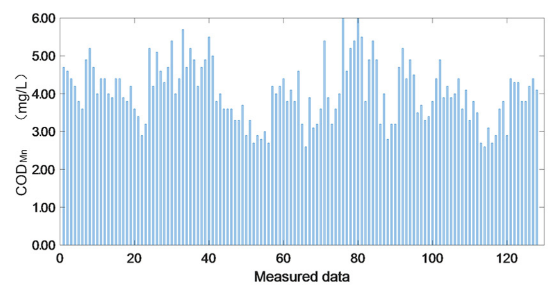

Figure 9. Measured data statistics of COD_{Mn}.

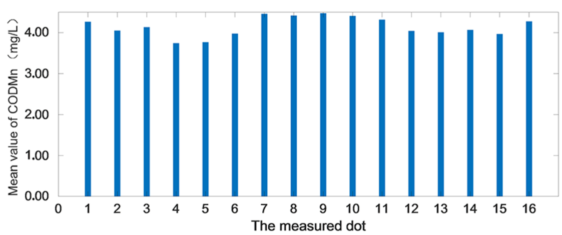

Figure 10. Statistics of COD_{Mn} at each station.

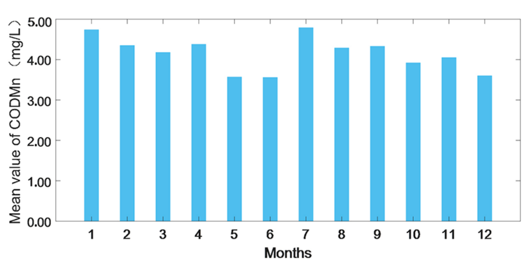

Figure 11. Statistics of COD_{Mn} at each month.

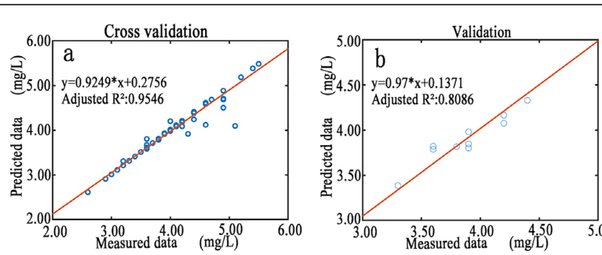

Figure 12. Support vector regression modeling of COD_{Mn} and spectral data on the training set (a) and the test set (b).

into six parts, five of which were trained and one verified in turn; the average value of the results repeated six times was used as the performance indicator of the model under the current sixfold cross validation.

The data set was divided into two parts; 80% were trained, and 20% were verified in turn, and the average of the results of the six runnings was used as the performance indicator of the model under the current sixfold cross validation. Sixfold cross validation was finally employed for testing the model performance, where the hyperparameters C and γ in the SVR model were obtained as 1.4142, and 5.6569, respectively.

Model Performance Evaluation

In the training stage of the SVR model, 70 training data sets were selected. The linear fitting coefficient of measured values and predicted values was $R^2 = 0.95$, the RMSE was 0.15 mg/L, and the SEE was 1.49 mg^2/L^2. Linear regression validation (Equation 12) was used to test the model on the remaining 10 groups of data. The measured value and predicted value had a good linear relationship, with slope a = 0.97, validation determination coefficient $R^2 = 0.88$, RMSE = 0.09 mg/L, and SEE = 0.11mg^2/L^2. The SVR model training and validation results showed that the regression model has good generalization ability, and it was feasible to use the spectral data for COD_{Mn} inversion,

$$y_i^* = ay_i + b \tag{13}$$

where y_i and y_i^* are the measured and predicted values of COD_{Mn}, respectively; a is the slope; and b is the regression constant.

BPANN modeling was also conducted by using satellite–earth synchronization data. After multi-testing, the model was optimized when the number of hidden-layer neurons was 10. The SSE, R^2, and RMSE of the fitting function between the measured and predicted values are shown in Table 5. R^2 performed well, while SSE was generally poor. The linear regression verification analysis of BPANN modeling is shown in Figure 13, in which the slope of linear regression of the training set and the validation set differed greatly. According to Table 5 and Figure 13, the modeling performance of BPANN was poor. Compared with BPANN, the SVR regression model had obvious advantages.

Table 5. Evaluation metrics of the model on the test set.

Test Serial Number	SSE	R^2	RMSE
8	5.41	0.54	0.74
13	5.31	0.53	0.73
21	8.21	0.82	0.91
27	6.35	0.63	0.80
38	5.96	0.60	0.77
43	9.66	0.97	0.98
56	8.93	0.89	0.95

SSE = sum of squared error; RMSE = root mean square error.

COD_{Mn} Estimation from *Landsat-8*

Based on the GEE remote sensing cloud platform, the *Landsat-8* image quality of Hongze Lake was analyzed, and the images of February, March, April, May, August, September, October, and December 2015 were selected to analyze the spatial variation rule of annual COD_{Mn}. By analyzing the image quality of each month in the past ten years, we found that there were more clouds in summer and winter, so year-over-year and month-over-month analysis could not be carried out. The image quality of spring and autumn (April and October) was better. Therefore, April and October of each year since 2013 were selected as representatives to study the long-term spatial distribution change rule of COD_{Mn}. The established SVR model was used to reconstruct the temporal and spatial distribution of COD_{Mn} in Hongze Lake (Figures 14 and 15). COD_{Mn} in January, June, July, and November 2015, as well as April 2017, April 2019, and April 2021, could not be effectively estimated due to high cloud cover in the images. Since the climatic conditions of Hongze Lake in March and May were similar to those in April in terms of rainfall, temperature, and other conditions, there was little difference in the influence of human activities near the lake from March to May. In order to facilitate the long-term time-series study, on the premise of analyzing the image data quality in March and May, the images in March of the current year were selected as the replacement in 2017 and 2021, and the image in May of the current year was selected for replacement in 2019. In addition, in order to improve the efficiency of model inversion, the prediction initial assignment was set within the range of 2.5 to 5.5 mg/L according to the measured COD_{Mn} data in 2015. The predicted values were normalized to facilitate the comparison and analysis of different concentration distributions and proportions.

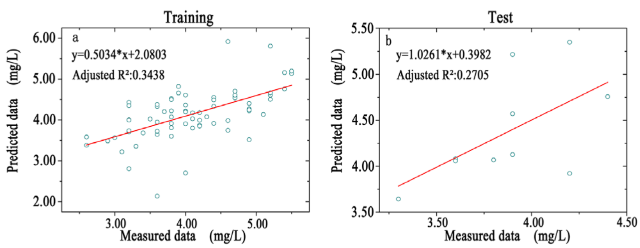

Figure 13. Back-propagation artificial neural network modeling of COD_{Mn} and spectral data on (a) the training set and (b) the test set.

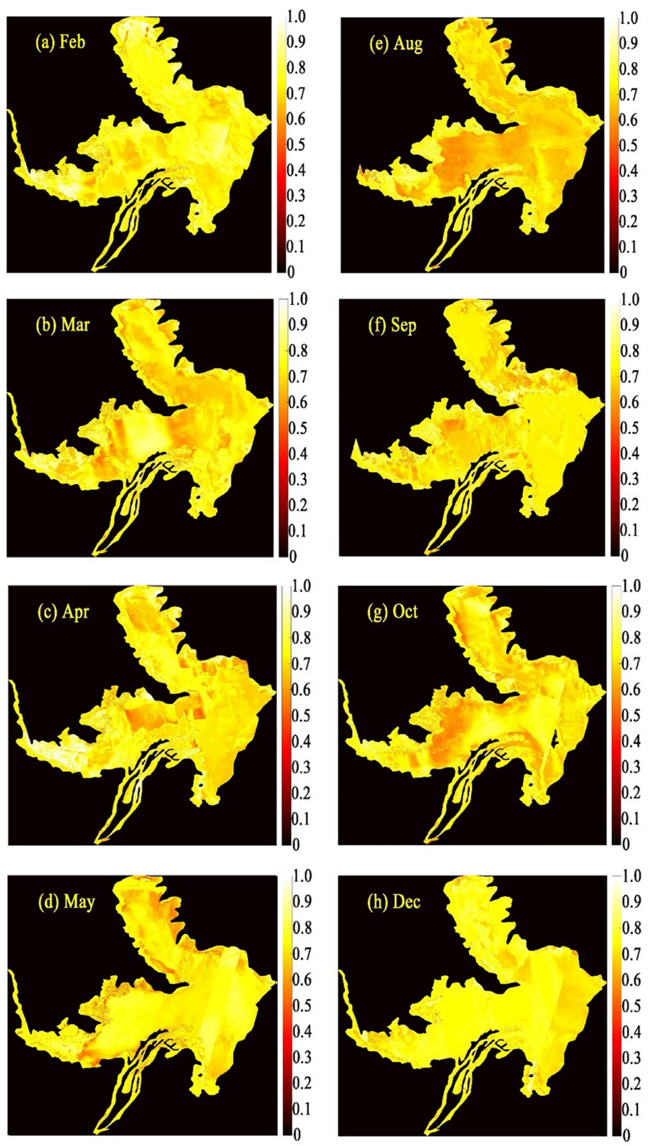

Figure 14. Monthly spatial distribution of COD_{Mn} in Hongze Lake in 2015 (a–h).

According to Figure 14, COD_{Mn} in 2015 was generally high, with the annual COD_{Mn} range of 3 to 6 mg/L in the lake. COD_{Mn} near Yugou (No. 2) in the western part of the lake was generally low throughout the year. Compared with February and December, COD_{Mn} from March to October was especially low. This might be related to the ecological interception of nearby wetlands, dilution of the lake, shallow water depth, and relatively developed aquatic vegetation in coastal waters (Xun *et al.* 2003). Among the inversion results for each month, December and February were relatively high, March and April were slightly higher than September and October, and April and May were obviously higher than other months, which may be related to the low water level of Hongze Lake from April to July (Xun *et al.* 2003). The distribution of COD_{Mn} in February was relatively high, which was consistent with the distribution of the measured data. In December, the COD_{Mn} has generally a certain predicted phenomenon of high relative to the measured data, which might be related to the spectral information of a little thin-ice interference in some regions (Xun *et al.* 2003). COD_{Mn} was relatively low in August, which might be related to more precipitation. The spatial distribution of COD_{Mn} in Chengzi Lake (Nos. 1, 3, and 4) was consistent in each month, which might be related to the relatively closed lake and low flow rate. The COD_{Mn} of Lihewa (No. 8) and Linhuai (No. 7) was higher in every month, which might be related to the organic pollutants discharged into the lake at the inflow of the lake. Suqian North (No. 4), Suqian South (No. 6) and Chenghe (No. 5) were located in the west-central part of the lake, which was consistent with the overall variation law. The COD_{Mn} was relatively low, which might be related to the open water and relatively high lake bottom elevation, significant wind effect, and short water changing cycle caused by wind-generated current (Xun *et al.* 2003). The COD_{Mn} was relatively high in Hanqiao (No. 9) and Xishunhe (No. 10). In Huaian North (No. 11), Huaian South (No. 15), Huaian East (No. 13), Huaian West (No. 16), Jiangba (No. 12), and Xishunhe (No. 10) near the artificial levee of Hongze Lake, the COD_{Mn} was generally lower than that of central and western Hongze Lake and with little change throughout the year. It might be related to the relatively stable annual discharge of domestic sewage from the nearby towns. According to the measured data, COD_{Mn} in Laozi Mountain (No. 14) was low in February, April, and October, but the predicted distribution was high throughout the year, which might be related to the acquisition of the surrounding land disturbance spectral information.

According to Figure 15, COD_{Mn} in Hongze Lake was high in general and has shown a decreasing trend in the past decade. This might be related to the management and control of catering vessels in the lake, wetland restoration, special regulation of river channels into the lake, sewage outlets into the lake, and agricultural non–point source pollution since 2013. Near the artificial levee of Hongze Lake, the decrease trend of COD_{Mn} was more obvious, which might be related to the effective promotion of relocation and reinforcement along the levee. In terms of time, COD_{Mn} was relatively high in spring. Comparative analysis of COD_{Mn} spatial distribution in the whole lake in two months showed that, except for 2017 and 2021, COD_{Mn} in April was generally higher than October, which was consistent with the measured results and might be related to the low water level from April to July (Xun *et al.* 2003). Since 2019, COD_{Mn} decreased significantly, especially in Chengzi Lake (Nos. 1 to 3), Yugou (No. 2), and Suqian North (No. 6). Among these, the cycle of Chengzi Lake was relatively slow, and this area was surrounded by the development zone of Suqian City. The decreasing of COD_{Mn} fully demonstrated that the control of industrial wastewater pollution had achieved remarkable results (Li *et al.* 2021). The spatial heterogeneity of organic pollution content in Hongze Lake was small and at the inflow of the lake was obviously higher, which might be related to the injection of organic pollutants and other factors. As the main inlet of the lake, the COD_{Mn} of Huai River continued to be high, which was consistent with the research results that Huai River, as the main inflow source (Wang *et al.* 2013), was the main contributor to the pollution load of Hongze Lake, and its pollution into the lake accounted for more than 51% of the total pollution (Vapnik 1995; Ge and Wang 2008).

The COD_{Mn} in Yanwei (No. 1) and Gaohu (No. 3) was high in April but low in October 2016 and 2019. This water was relatively closed, with a slow flow rate and long water exchange cycle, which might be related to the discharge of pollution from the surrounding aquaculture. COD_{Mn} was relatively high in Suqian North (No. 4), Suqian South (No. 6), Chenghe (No. 5), and Hanqiao (No. 9) and was significantly higher in April than October, which might be related to the inflow of rivers into the lake, agricultural production and aquaculture waste discharge, and urban domestic sewage discharge. The COD_{Mn} of Xishunhe (No. 10) and Huaian North (No. 11) was relatively high, but it was lower in April than October because the area was close to Zhouyu Village and was affected by rural sewage and living habits (Ye *et al.* 2011).

The COD_{Mn} of Huaian East (No. 13), Huaian South (No. 15), Huaian West (No. 16), and Jiangba (No. 12) was relatively low, which might be due to its being located in the main water crossing area of Hongze Lake and water exchange being faster. In addition, the pollution discharge adjacent to the artificial levee of Hongze Lake was relatively well controlled. The COD_{Mn} of Yugou (No. 2) and Linhuai

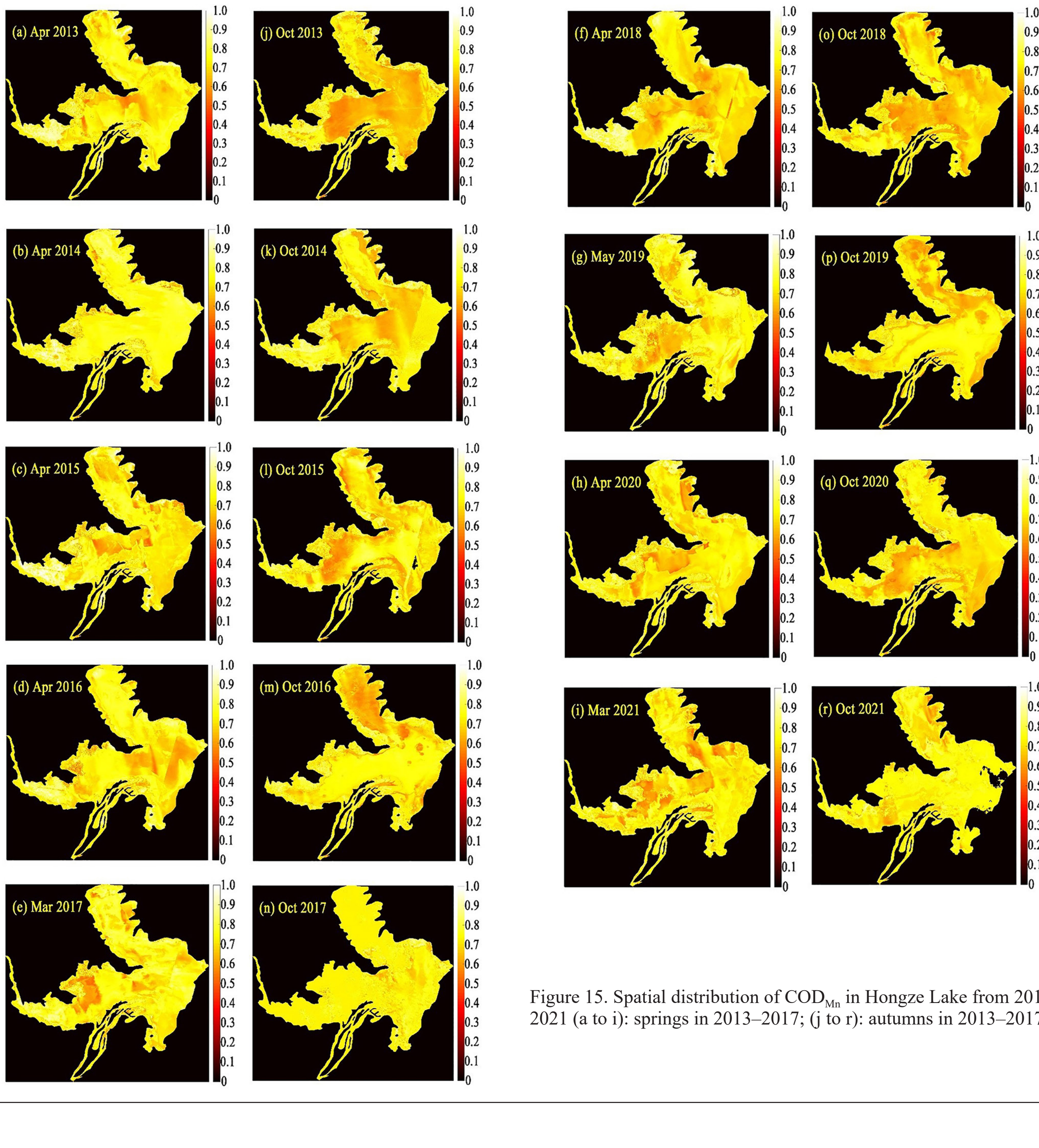

Figure 15. Spatial distribution of COD_{Mn} in Hongze Lake from 2013 to 2021 (a to i): springs in 2013–2017; (j to r): autumns in 2013–2017.

(No. 7) was located near the Hongze Lake Wetland National Nature Reserve. Compared with the adjacent Lihewa (No. 8), the COD_{Mn} of Yugou (No. 2) and Linhuai (No. 7) was significantly lower, which might be related to the comprehensive improvement of the rural environment. According to the measured values, the COD_{Mn} of Laozi Mountain (No. 14) was relatively low, which might be related to the good local natural environment and high green space coverage. However, the comparison between the predicted and measured values in this region showed that the predicted values were overestimated, which might be related to the influence of adjacent land pixels.

Spatial Distribution and Influencing Factors of COD_{Mn} in Hongze Lake

According to the surface water environmental quality standard of China (GB 3838-2002; Cui *et al.* 2021; Li *et al.* 2021), the surface water can be divided into five water quality classes according to their functions: Class I applies mainly to source water and national nature reserves. Class II applies mainly to the centralized drinking water surface water source level 1 protection zone, the habitat of rare aquatic organisms, the spawning grounds of fish and shrimp, the feeding grounds of young fish, and so on. Class III applies mainly to the centralized drinking water surface water source secondary protection area, fish and shrimp wintering grounds, migration channels, aquaculture areas, and other fishery waters and swimming areas. Class IV applies mainly to general industrial water areas and recreational water areas with no direct contact with the human body. Class V applies mainly to agricultural water use areas and general landscape water areas. Among these, the upper limit of COD_{Mn} in a Class II water body is 4 mg/L, and that in a Class III water body is 6 mg/L. The COD_{Mn} in the whole of Hongze Lake was generally between 3.0 and 6.0 mg/L, and the high value of COD_{Mn} had a wide distribution, showing non–point source characteristics. From the comparison of different months and years, COD_{Mn} in the lake was generally high, and the area of Class III water in each month was large, while COD_{Mn} in August was relatively low. From 2013 to 2021, the water quality was classified as Classes II to III, especially in winter. In terms of spatial distribution, the inlet area was significantly higher than the center area. COD_{Mn} is an index to characterize the degree of organic pollution and reductive inorganic substances in water and can be used to measure the content of oxygen-consuming substances in water. The higher COD_{Mn} is, the less dissolved oxygen in water is. Hypoxia seriously affects the growth of fish and crabs in the water and even leads to the death of a large number of fish and crabs. For example, from 25 to 26 August 2018, the water pollution incident of Hongze Lake caused by sewage being carried by upstream flood discharge resulted in the whole river turning black and a large number of fish and crabs dying. The overall distribution of COD_{Mn} along the lakeshore was relatively uniform, showing a slightly higher distribution of bay than non-bay areas and no obvious over-distribution of point sources. According to the high value present the characteristics of the non–point source distribution and the influencing factors for the spatial distribution of COD_{Mn} in Hongze Lake, it can be concluded that in recent years, Hongze Lake's surrounding industrial wastewater emissions regulation was productive. Due to that "water pollution prevention and control law," "a three-year work plan for Hongze Lake governance and protection" and other policies were promoted, and since 2019, COD_{Mn} in Chengzi Lake has been significantly reduced (Nos. 1 to 3), which showed that industrial wastewater pollution has been effectively controlled in recent years (Cui *et al.* 2021).

Exogenous pollution in the inflow of Hongze Lake was still the main reason for the relatively high COD_{Mn}. The COD_{Mn} values of Huai River, Xinsu River, and Huaihongxin River were above 4.4 mg/L. The mean value of COD_{Mn} measured near the Linhuai station was 4.5 mg/L. Hongze Lake was a waterborne lake, and the inflow of Huai River took up 70% of the total inflow of the lake (Xun *et al.* 2003). The Huai River pass through Huainan and Bengbu, Xinsu River pass through Xuzhou, Huaibei and Suzhou, and Huaihongxin River pass through Fuyang, respectively. The discharge of industrial sewage and domestic water from the cities causes serious pollution in the rivers. Strengthening the management of wastewater discharge in the upper reaches of rivers into the lake still played an important role in reducing the exogenous input of oxygen-consuming substances in Hongze Lake. In addition, compared with the adjacent Linhuai (No. 7) and Lihewa (No. 8), the COD_{Mn} of Yugou was obviously low throughout the year, with an average of 4.0 mg/L, indicating that the orderly construction of wetland nature reserve was conducive to the retention of organic pollutants and the improvement of water quality.

The main sources of pollution in the lake were agricultural production and domestic sewage. According to the survey, there were relatively few large enterprises around Hongze Lake, but there were phenomena such as land reclamation, illegal construction of docks, illegal cultivation, illegal construction of factories, fishermen's villages, catering boats, and so on. Due to the long shoreline and the large arbitrariness in the sale, transfer, and alteration of ships, it was difficult to make clear the facts and the situation, which also increased the difficulty of control. In addition, a considerable amount of garbage and pollutants was produced by the scattered domestic boats and their fishermen, transport ships, and the people in production and living nearby water bodies, and they were not collected and treated in a centralized manner. The biological and environmental pollution caused to the Hongze Lake system cannot be underestimated.

Some fishermen illegally catch aquatic products at night during the closed fishing season or in closed fishing areas or illegally hunt in remote waters, bringing uncontrollable human factors to the environmental protection of the river system. At present, the area of Seine farming in Hongze Lake is more than 200 km^2, and the output is as high as two times the fishing amount, of which more than 90% is from crab farming. Excessive feeding and discharge sedimentation produced a lot of endogenous pollution. In addition, the phenomenon of fencing and land reclamation is common in the south, west, and north of the lake, especially in the south of Sihong County and the north of Xuyi County. As a result, the free water surface reduced, which seriously affected the growth of vegetation along the lake and also reduced the interception and degradation of organic pollutants. The circle fencing phenomenon was particularly prominent near Linhuai (No. 7) and Laozi Mountain (in No. 14). In the eastern part of Hongze Lake, there was less circle fencing, but the population density was high. Under the strong interference of human activities, COD_{Mn} was also high. The discharge of pesticide and fertilizer, fishery tail water, and domestic sewage were the main causes of the endogenous pollution of Hongze Lake. Therefore, orderly promotion of wetland protection, returning farmland to the lake, ecological agriculture, illegal supervision, fishermen ashore, and other measures could help to reduce the pollution of Hongze Lake.

Discussion

In this study, the *Landsat-8* images were used to investigate the spatial and temporal distributions of COD_{Mn} in Hongze Lake, and the influencing factors were analyzed. With the help of the established inversion SVR model, the distributions of the monthly COD_{Mn} in 2015 and the interannual COD_{Mn} during the past decade in the whole lake were investigated. The approach proposed in this study provides reference for remote sensing monitoring of inland water quality but also has some limitations.

Approach Effectiveness

The evaluating metrics of the SVR model established in this study indicated that the modeling effect was good and outperformed the BPANN, with $R^2 = 0.95$, RMSE = 0.15 mg/L, and SSE = 1.49 mg^2/L^2. Xu *et al.* (2013) analyzed from the perspective of principle and believed that SVR conducts model training by seeking a way of minimizing structural risk, aiming at controlling the overall error, while the BPANN aims at continuously fitting the local truth value, without controlling the overall error, leading to poor model generalization in model prediction. The conclusion in this study further explained the predictive advantage of the SVR model in Hongze Lake.

The distribution of COD_{Mn} obtained from the *Landsat-8* images was consistent with the results obtained from traditional monitoring, and only a few points showed relatively large deviation, such as Laozi Mountain, which suffered from the influence of adjacent land pixels.

The distribution of COD_{Mn} and the spatiotemporal variation at nonsampling sites were in sync with the characteristics of local natural factors and human activities. The interannual variation of COD_{Mn} was consistent with the spatiotemporal variation of results during 2012–2018 (Li *et al.* 2021). The seasonal variation of COD_{Mn} was consistent with the variation in the inflow rivers of Hongze Lake proposed by (Cui *et al.* 2021). These results indicated that the proposed approach was effective in the investigation of COD_{Mn} distribution in Hongze Lake. Table 6 shows the comparison with other techniques.

Table 6. Final comparison of the model on test set.

Methods	R^2	RMSE (mg/L)	SSE (mg²/L²)	Index
Proposed (SVR)	0.95	0.15	1.49	COD_{Mn}
Kim et al. (2014) (SVR)	0.91	1.74		Chl *a*
	0.98	11.42		SPM
Vakili and Amanollahi (2020) (ANN)	0.64	0.04	0.03	TP
	0.86	0.06	0.05	TN
Xu et al. (2013) (RF)	0.95	2.784	—	Chl *a*

RMSE = root mean square error; SSE = sum of squared error; SVR = support vector regression; ANN = artificial neural network; RF = random forest.

Approach Limitations

In data preparation, after the screening of data, such as image cloud coverage without exceeding 20%, no scattered cloud blocking of the sampling points, and abnormal point elimination, only 80 groups of data met the requirements, and the sample size was relatively insufficient. The in situ measured data were obtained from 16 sampling points in the whole lake in monthly batches. The amount of modeling data in a single batch was insufficient, while the measured data in different batches had certain differences in imaging conditions, affecting the accuracy of the modeling. In the future research, more sample data in the same batch should be collected to study the applicable boundary of the model. In the process of the SVR modeling, the grid search was used to optimize the hyperparameters of the model, which lacks of physical basis, so it is impossible to carry out specific physical explanation. But from the evaluations of SVR modeling for the training set and the test set (R^2 = 0.95, RMSE = 0.15, SSE = 1.49; R^2 = 0.88, RMSE = 0.09, SSE = 0.06, respectively), the result is very beneficial for the management of COD_{Mn} in Hongze Lake and provides a feasible scheme for remote sensing monitoring of COD_{Mn} in inland water.

Due to the low temporal resolution of *Landsat-8* images and the influence of clouds, the monthly dynamic monitoring could not be satisfied. In this study, when studying the monthly distribution of COD_{Mn} in 2015, the images of some months were missing, and the detailed spatial distribution of COD_{Mn} in each month of the year could not be mapped. Similarly, due to the influence of clouds and other factors, although April and October were selected as representatives for the distribution of COD_{Mn} in the past decade, there were still missing data in some months, which would inevitably lead to certain errors if the images of the adjacent months were selected. Sentinel-2 images have higher temporal resolution and more bands than those of the *Landsat-8*, so it is suggested that the Sentinel-2 images could be used to investigate the distribution of COD_{Mn} in the future.

During the analysis of the influencing factors related to COD_{Mn} distribution, a comprehensive survey was carried out mainly in the lakefront and the lake area. But the surveys along the river were not included, especially the characteristics and laws of non–point source pollution. In the future research, land use in the western watersheds of Hongze Lake, such as the watersheds of Huai River, Xinsu River, Xinbian River, and others, should be investigated to find out the correlation between land use and the dynamics of COD_{Mn} distribution.

Conclusion

With the help of the GEE remote sensing cloud computing platform, the spatial and temporal distributions of COD_{Mn} in Hongze Lake were modeled by the SVR model, established on the basis of *Landsat-8* images and the synchronal in situ water quality measurements. Through analysis of the monthly spatiotemporal variation of COD_{Mn} in 2015 and the interannual spatiotemporal variation in the past decade, the potential influencing factors of COD_{Mn} distribution were explored. The main conclusions are as follows:

1. The SVR model accurately fits the spectral data of *Landsat-8* images and the measured COD_{Mn}, with R^2 = 0.95, RMSE = 0.15 mg/L, and SSE = 1.49 mg²/L². The slope associated with the linear regression between the validating set and the measured data was 0.97, R^2 reached 0.88, and RMSE and SSE were 0.09 mg/L and 0.11 mg²/L², respectively. Meanwhile, the model comparison showed that the SVR model performed better than the BPANN model for the COD_{Mn} remote sensing inversion in Hongze Lake.
2. Huai River, Xinsu River, and Huaihongxin River were still the main sources of oxygen-consuming pollutants in Hongze Lake. The wetland natural reserve near Yugou had a significant effect on reducing COD_{Mn}. According to the annual and interannual variations of COD_{Mn}, the COD_{Mn} in the whole lake was generally high and thus long-term control of endogenous pollution and fishermen's villages and wetland ecological restoration should be carried out from the perspective of overall ecological factor recovery.
3. The COD_{Mn} in the lake was high, and the COD_{Mn} at the eastern inlet of the lake was higher, indicating that the rivers into the lake were the main source of organic pollutants. The agricultural non–point source pollution in the basin and the overall management of river channels were necessary measures for the exogenous management of Hongze Lake. However, COD_{Mn} in August was significantly lower, which might be due to the large precipitation with a significant dilution effect on pollutants. In the coastal urban agglomeration areas within the jurisdiction of Siyang County, Hongze District, Xuyi County, and Sihong County, the COD_{Mn} had little change from year to year and did not change significantly throughout the year. It indicated that the main sources of organic pollutants were urban industrial wastewater and domestic water. It is necessary to further improve the treatment and management system of industrial and domestic wastewater, strengthen the promotion of rainwater and sewage diversion projects, and improve the efficiency of sewage treatment.
4. According to the change rule of COD_{Mn} in the past decade, the measures related to Hongze Lake governance in recent years have achieved certain results, but the results are not significant. It is necessary to further refine and promote the measures based on local conditions and ensure long-term effect. The water level of Hongze Lake is controlled by humans. The water level is higher in spring and lower in summer, which is contrary to the seasonal water level variation in dry, abundant, and normal periods in the Huai River basin. In the comprehensive treatment, it is necessary to combine the characteristics of water level control management, water resources development, utilization scenarios, spatial distribution of water quality pollution, and other factors to formulate a governance mode of integrated "one place, one policy, overall planning, and coordination" management, control, and governance.

Due to the limitation of field sampling and the low temporal resolution of the *Landsat-8* images, this study still has the problems of insufficient COD_{Mn} model training samples and a single sampling area. In the future research, higher temporal-resolution multispectral images and more in situ COD_{Mn} measurements are expected to further improve the model performance. In addition, multi-region sampling can also validate the model and improve the generalization performance of the SVR model.

Acknowledgments

This work was supported by the Strategic Priority Research Program Project of the Chinese Academy of Sciences (grant no. XDA23040100) and the Jiangsu Marine Science and Technology Innovation Project (Grant No.: JSZRHYKJ202202, and JSZRHYKJ202002). We thank the USGS for providing *Landsat-8* data and the Jiangsu Hongze Lake Management Office for providing the in situ measurements.

References

Andrew, A. M. 2001. An introduction to support vector machines and other kernel-based learning methods by Nello Christianini and John Shawe-Taylor, Cambridge University Press, Cambridge, 2000, 189pp, Robotica, 18(06): 687-689.

Cai, Y., Z. Zhang, R. Tang, Y. Chen, W. Huang, Z Gong. 2020. Health evaluation and protection of Hongze Lake ecosystem. *Jiangsu Water Conservancy* 7:2–7.

Chen, S., M. Ren, W. Sun. 2021. Combining two-stage decomposition based on machine learning methods for annual runoff forecasting. *Journal of Hydrology* 603:126945.

Chen, Y., S. Liu, K. Wang, S. Song, P. Liang, F. Chen. 2020. Remote sensing inversion of water quality and nutrient status evaluation of Caohai Sea based on Landsat satellite images. *Journal of Hydroecology* 5(41):25–27.

Cortes, C. and V, Vapnik. 1995. Support-vector networks. *Machine Learning* 20(3):273–297.

Cui, C., Z. Dong, J. Tong, Q. Shi, T. Zhang, X. Chen. 2021. Water quality evaluation and variation law of main inflow channels of Hongze Lake. *Jiangsu Water Conservancy* 9:27–33.

Duan, Q., L. Meng, Z. Fan, W. Hu, W. Xie. 2015. Research on the applicability of water information extraction method from GF-1 satellite images. *Remote Sensing for Natural Resources* 27(4):79–84.

Emhamed, A. and J. Shrivastava. 2021. Electrical load distribution forecasting utilizing support vector model (SVM). *Materials Today: Proceedings* 47(1):41–46.

Fu, D. and J. Yue. 2019. Analysis of Hongze Lake surface area and its change based on Landsat image. *Journal of Gansu Sciences* 31(2):36–38.

Gao, J. and Z. Jiang. 2012. *Conservation and Development of Five Major Freshwater Lakes in China*. Beijing: Science Press.

Ge, X. and G. Wang. 2008. Ecological and environmental problems faced by Hongze Lake and their causes. *The People of the Yangtze River* 39(1):27–29.

Guo, H., J. Huang, B. Chen, X. Guo, V. Singh. 2021. A machine learning-based strategy for estimating non-optically active water quality parameters using Sentinel-2 imagery. *International Journal of Remote Sensing* 42(5):1841–1862.

Guo, J., Y. Chen, Z. Li, F. Fang, Z. Sun, Y. Chen. 2011. Seasonal variation of chlorophyll A and its relationship with major algae in Xiaojiang Backwater of the Three Gorges. *Environmental Science* 32(4):976–981.

He, Y., S. Jin and W. Shang. 2021. Water quality variability and related factors along the Yangtze River using Landsat-8. *Remote Sensing* 13(2241):2–17.

Hou, W. J. Wang and X. He. 2021. Heavy mineral oil spectral pattern recognition based on support vector machine modeling. *Laser and Optoelectronics Progress* 58(6):630001.

Huang, Y., Z. Huang, W. Xiao, L. Zeng, H. Li. 2021. Study on ammonia nitrogen and COD_{Mn} load in inlet and outlet sections of the Yangtze River in the Three Gorges Reservoir Area. *Journal of Zhejiang A&F University* 6:1221–1230.

Jiang, X., S. Wang, L. Zhong, X. Jin, S. Sun. 2010. Seasonal variation of algae biomass in Chaohu Lake. *Environmental Science* 31(9):2056–2062.

Jindal, R., R. Thakur, U. Singh, A. Ahluwalia. 2014. Ahluwalia phytoplankton dynamics and water quality of Prashar Lake, Himachal Pradesh, India. *Sustainability of Water Quality and Ecology* 3(4):101–113.

Jun, S., K. Bai, K. Li, T. Wang. 2017. Study on the application of comprehensive water quality identification index method in Hailar River water quality evaluation. *Environmental Science and Management* 4:171–176.

Kawabe, M. and M. Kawabe. 1997. Factors determining chemical oxygen demand in Tokyo Bay. *Journal of Oceanography* 53:443–453.

Keith, D., J. Rover, J. Green, B. Zalewsky, M. Charpentier, G. Thursby, J. Bishop. 2018. Monitoring algal blooms in drinking water reservoirs using the Landsat-8 Operational Land Imager. *International Journal of Remote Sensing*. 39(9):2189–2842.

Kim, Y., J. Im, H. Ha, J. Choi, S. Ha. 2014. Machine learning approaches to coastal water quality monitoring using GOCI satellite data. *GIScience & Remote Sensing* 51(2):158–174.

Lei, S., J. Xu, Y. Li, C. Du, L. Li. 2020. An approach for retrieval of horizontal and vertical distribution of total suspended matter concentration from GOCI data over Lake Hongze. *Science of the Total Environment* 700:2–14.

Li, B., G. Yang, R. Wan, B. Liu, X. Dai, X. Chen. 2017. Temporal variability of water quality in Poyang Lake outlet and the associated water level fluctuations: A water quality sampling revelation. *Resources and Environment in the Yangtze Basin* 26(2):289–296.

Li, Y., Z. Zhang, J. Cheng, L. Zou, Q. Zhang, M. Zhang, Z. Gong, S. Xie, Y. Cai. 2021. Temporal and spatial variation of water quality in Hongze Lake from 2012 to 2018 and its causes. *Lake Science* 33(3):715–726.

Liang, K. and H. Yang. 2016. Spectral data correction method for the online detection of total nitrogen in water quality. *Chinese Journal of Environmental Engineering* 10(12):7397–7399.

Ministry of Ecology and Environment of the People's Republic of China. 2002. *GB 3838-2002. Environmental Quality Standards for Surface Water*. Beijing: Department of Science and Technology Standards, State Environmental Protection Administration.

Ministry of Environmental Protection. 1990. *GB 11892-89. Determination of Permanganate Index in Water Quality*. Beijing: Ministry of Environmental Protection.

Mohammad, H. 2021. Land–lake linkage and remote sensing application in water quality monitoring in Lake Okeechobee. Florida, USA. *Land* 10(147):1–3.

Mountrakis, G., J. Im and C. Ogole. 2011. Support vector machines in remote sensing: A review. *ISPRS Journal of Photogrammetry and Remote Sensing* 66(3):247–259.

Naddeo, V., T. Zarra and V. Belgiorno. 2007. Optimization of sampling frequency for river water quality assessment according to Italian implementation of the EU Water Framework Directive. *Environmental Science & Policy* 10(3):243–249.

Qiao, L., J. Huang, J. Gao, Q. Huang, Y. Zhou, W. Tian. 2016. Spatial-temporal variation characteristics of chlorophyll-a concentration in Lake Hongze. *Lake Science* 28(3):583–591.

Rao, H. 2015. Determination of permanganate index in surface water by spectrophotometry. *Exchange of Scientific Papers and Cases* 7:48.

Sagan, V., K. Peterson, M. Maimaitijiang, P. Sidike, J. Sloan, B. Greeling, S. Maalouf, C. Adams. 2020. Monitoring inland water quality using remote sensing: Potential and limitations of spectral indices, bio-optical simulations, machine learning, and cloud computing. *Earth-Science Reviews* 205:103187.

Shang, S., D. Feng, L. Tan, P. Liu, W. Guo. 2016. Temporal and spatial variation analysis of main driving factors of water ecosystem evolution in Jinan City. *Water Ecological Protection* 12:36–37.

Shang, S., X. Xiang, W. Guo, X. Yin, Z. Xu. 2021. Relationship between benthic functional feeding groups and environmental factors. *The People of the Yellow River* 6:77–79.

Shen, J., Z. Liu, X. Yang. 2020. *Limnology*. Beijing: Higher Education Press.

Tomar, D. and S. Agarwal. 2015. Twin support vector machine: A review from 2007 to 2014. *Egyptian Informatics Journal* 16(1):55–69.

Liu Y. 1985. UN issues new water quality standards and testing methods. *Environmental Engineering* 03:37-45.

Tan J., A. Keith and C. Indrajeet. 2015. Using hyperspectral data to quantify water quality parameters in the Wabash River and its tributaries, Indiana. *International Journal of Remote Sensing* 11(16):5467–5482.

Vakili, T. and J. Amanollahi. 2020. Determination of optically inactive water quality variables using Landsat 8 data: A case study in Geshlagh reservoir affected by agricultural land use. *Journal of Cleaner Production* 247:119134.

Vapnik, N. V. 1995. Adaptive and learning systems for signal processing, communications and control. In *The Nature of Statistical Learning Theory*, 138–167. New York: Springer-Verlag.

Wang, X., F. Shi, L. Yu, Y. Li. 2013. *MATLAB Neural Network Analysis of 43 Cases*. Beijing: Beihang University Press. 125-133.

Wu, C. 2018. *Remote Sensing Diagnosis of Ecological Health of Important Lakes and Wetlands in the Middle and Lower Reaches of Yangtze River*. Nanjing: Institute of Remote Sensing and Digital Earth, Chinese Academy of Sciences.

Xiong, J., C. Lin, R. Ma, Z. Cao. 2019. Remote sensing estimation of lake total phosphorus concentration based on MODIS: A case study of Lake Hongze. *Remote Sensing* 11(2068):2–17.

Xu Y., X. Dong and J. Wang. 2019. Comparison of chlorophyll-a concentration retrieval from four machine learning models in Taihu Lake. *Journal of Hydroecology* 7:1321–1326.

Xu, Y., C. Ma, S. Huo, B. Xi, G. Qian. 2013. Taking Cheng Hai as an example, support vector machine regression algorithm was used to predict chlorophyll A concentration. *Journal of Environmental Engineering Technology* 3:207–210.

Xun, D., D. Zhang. 2003. *Hongze Lake Volunteers*. Beijing: Local Chronicle Press.

Yang, C. 2020. *Water Quality Parameters Inversion and Eutrophication Evaluation of Hefei Huancheng River Based on Landsat-8 Satellite Image Data*. Hefei: Anhui Jianzhu University.

Yang, K. 2021. *Huai 'an City Ecological Environment Status Bulletin, Huai'an Ecological Environment Bureau, Huai'an, China*

Yang, L., K. Lei, M. Wei, F. Guo, W. Yan. 2013. Temporal and spatial changes in nutrients and chlorophyll-a in a shallow lake, Lake Chaohu, China: An 11-year investigation. *Journal of Environmental Sciences* 25(6):1117–1123.

Ye, C., C. Li, B. Wang, J. Zhang, L. zhang. 2011. Discussion on construction scheme of healthy water ecosystem in Hongze Lake. *Lake Science* 23(5):724–730.

Ye, T., L. Li, Y. Yao, L. Xia, W. Guan. 2019. Interannual variation of maximum turbidity zone in Hangzhou Bay based on Landsat images. *Journal of Wuhan University* 9:1377–1382.

Yu, L., F. Shi, H. Wang. 2015. *Intelligent Algorithm*. Beijing: Beihang University Press.

Zhang, Y., X. Qian, Y. Qian, J. Liu, F. Kong. 2009. Quantitative remote sensing of chlorophyll a in Taihu Lake based on machine learning method. *Environmental Science* 30(5):48–55.

Zhou, T., J. Zou, Y. Cui, X. Wang, C. Xie, P. Xia. 2022. Method and application of water extraction from remote sensing images based on principal component analysis and support vector machine. *Water Resources Protection* 1836(006) (in press).

Exploring Spatiotemporal Variations and Driving Factors of Urban Comprehensive Carrying Capacity in the Yangtze River Delta Urban Agglomeration

Songjing Guo, Xueling Wu, Ruiqing Niu, and Wenfu Wu

Abstract

The Yangtze River Delta urban agglomeration (YRDUA) is one of the most active economic development regions in China. However, the YRDUA is facing the severe test of sustainable development. Therefore, this study evaluates the urban comprehensive carrying capacity (UCCC) of cities in the YRDUA from 2009 to 2019 from natural, social, and economic perspectives, and uses the Geographically and Temporally Weighted Regression model to analyze driving factors of spatiotemporal variations of the UCCC. Besides, this study divides the UCCC into three levels: high, medium, and low. The results indicate that: 1) there is a significant spatial heterogeneity of the UCCC in the YRDUA; 2) the UCCC in the YRDUA is generally at medium level and presents a gradually increasing trend; 3) 10 driving factors significantly affect the UCCC, and the influence intensity is non-stationary in time and space. These findings can provide references for improving the UCCC in the YRDUA.

Introduction

With the rapid development of economy, the population is rapidly aggregating from rural to urban areas, and 68% of people are expected to live in cities by 2050. During the process of rapid urbanization, land covers have changed significantly (Tran 2016; Beck 1992), bringing a series of ecological and environmental problems, such as natural disasters (Allouhi *et al.* 2015), air pollution (Zhang *et al.* 2019), ecological degradation, and resource shortage (Chen *et al.* 2017). Cities are facing the threat of unhealthy development, and the urban carrying capacity is gradually overloaded (Yang and Li 2011). Scholars have been committed to find a sustainable development way that takes into account eco-environmental protection, economic development, and social progress (Tian *et al.* 2021). And comprehensive evaluation of urban carrying capacity is an important link to achieve sustainable urban development.

Up to now, there is no unified concept of the sustainable development (Walz 2000); most views believe that sustainable development should be committed to the coordinated development between human social activities and the ecosystem (Li *et al.* 2011). Under such a background, the concept of ecological carrying capacity was proposed (Fan 2009; Wang *et al.* 2018), which is an objective reflection of the natural system's regulation capacity (Zhang *et al.* 2018). Besides, ecological carrying capacity also reflects the degree of human activities to the use of resources and damage to the ecological environment. With the acceleration of urbanization, urban population expansion, resource and environmental constraints, and serious traffic congestion are becoming increasingly prominent. Many scholars began to study urban adaptation from the urban comprehensive carrying capacity (UCCC) (Zhou *et al.* 2018). The concept of UCCC provides a specific evaluation method and measurable index for the urban sustainable development capacity, and also provides guidance for urban managers to better deploy urban resources (Liu *et al.* 2020; Pandit *et al.* 2017; Wang *et al.* 2019).

Urban agglomeration is a high-level urbanization development pattern. In China, urban agglomerations concentrate 45% of urban population, 50% of Gross Domestic Product (GDP), and 60% of foreign capital (Fang 2015). With the continuous aggregation of urban space, urban diseases such as the depletion of natural resources, ecosystem degradation, and environmental pollution are also highly concentrated in the urban agglomeration (Heikkila and Xu 2013). The Yangtze River Delta Urban Agglomeration (YRDUA) is a typical representative of Chinese urban agglomeration. Although it occupies only 2.1% of China's national area, it accounts for 20% of the GDP and is considered an important engine of China's economic development. At present, the YRDUA is facing the severe test of sustainable development. Therefore, it is of great significance to evaluate the UCCC in the YRDUA and explore the spatiotemporal variations and driving factors of UCCC for the sustainable development of the YRDUA.

Previous carrying capacity studies followed the rule of minimum limiting factors, emphasizing that a single factor has a decisive impact on UCCC, and analyzed from a single key factor such as land cover, population, and transportation (Edmonds 2005). For example, Zhang *et al.* (2019) used the principal component analysis method to analyze the water resources carrying capacity of Huhhot and found that there were great differences in the water resources use capacity of various districts (Liu *et al.* 2019). And Guo and Liu (2011) studied the land carrying capacity of 11 cities in Hebei Province and found that land carrying capacity is positively correlated with the land economy. Besides, Shan and Wang selected three indicators including climate natural capacity, urban climate pressure, and urban coordinated development capacity were selected to evaluate the climate carrying capacity, indicating that improving energy efficiency and reducing undesirable outputs of power were the main ways to improve regional climate carrying capacity (Shan and Wang 2021).

Different regions have different ecological conditions and development patterns. The impact of the same factor on UCCC varies from region to region. In addition, UCCC is affected by various dynamic factors, such as human activities, energy consumption, and climate change, especially in rapidly developing regions like the YRDUA. In the analysis of the driving factors in UCCC, the characteristics of factors including the temporal dynamics, spatiotemporal coupling, and spatial interactions should be taken into account. The least square and

Songjing Guo, Xueling Wu, and Ruiqing Niu are with the Institute of Geophysics and Geomatics, China University of Geosciences, Wuhan 430074, China (rqniu@163.com).

Wenfu Wu is with the School of Remote Sensing Information and Engineering, Wuhan University, Wuhan 430079 China.

Contributed by Zhenfeng Shao, July 7, 2022 (sent for review July 28, 2022; reviewed by Md. Enamul Huq, Bin Hu).

Photogrammetric Engineering & Remote Sensing
Vol. 88, No. 12, December 2022, pp. 803–812.
0099-1112/22/803–812

doi: 10.14358/PERS.22-00097R2

geographically weighted regression (GWR) methods are usually used to estimate the driving factors of UCCC, but they ignore the spatiotemporal heterogeneity of factors. Huang *et al.* (2010) proposed the geographically and temporally weighted regression (GTWR) model, which better explained the relationship between factors from the perspective of spatiotemporal heterogeneity, and significantly improved the simulation accuracy of the model. Nowadays, it has been widely used in economics, geography, and other fields (Wang *et al.* 2020; Yuan 2020).

In viewing this, this study contributes the following: (1) this study selects 15 indicators from three perspectives of nature, society, and economy to evaluate the UCCC by entropy method in the YRDUA; (2) the UCCC of the YRDUA from 2009 to 2019 is analyzed from multiple perspectives and levels, and the spatiotemporal evolution of the UCCC among cities in the YRDUA is discussed; (3) this study analyzes the driving factors of the UCCC from spatiotemporal perspective using GTWR model, clarifies the development stages and constraints of the UCCC among cities in the YRDUA, and then puts forward some suggestions to improve the UCCC. This study has important reference value for guiding the sustainable development of the YRDUA.

Study Area and Data Sets

Study Area

The YRDUA is one of the regions with the most active economic development and the highest degree of urban agglomeration in China. With Shanghai as the center, it is closely connected with Jiangsu, Zhejiang, and Anhui provinces, covering 26 cities, as shown in Figure 1. The study area covers approximately 212 700 km² and has a population of about 150 million. Due to the prominent geographical location and economy, the study area has an important strategic position in the national modernization.

However, the YRDUA is experiencing the development mode of "spreading cakes", which puts increasing pressure on the ecological environment and economic growth. Therefore, it is necessary to analysis UCCC in the YRDUA and explore its spatiotemporal trend and driving factors, so as to construct a high-quality development economic region.

Data Sets

This study collects meteorological, population, land cover, and statistical data of 26 cities in the YRDUA from 2009 to 2019, and then extracts 15 indicators from natural, social, and economic perspectives for evaluating UCCC. The meteorological data is from the National Oceanic and Atmospheric Administration physical sciences laboratory (https://www.esrl.noaa.gov/psd/data/gridded), including the annual average temperature and annual total precipitation. The population data is collected from the website of WordPop (https://www.worldpop.org/). The proportions of agricultural land and construction land are derived from the data set of "MCD12Q1.006 MODIS Land Cover Type Yearly Global 500m". And the vegetation coverage data used is the data set of "MOD44B.006 Terra Vegetation Continuous Fields Yearly Global 250m". The two data sets are provided by the Google Earth Engine. The remaining data is collected from "China Urban Statistical Yearbook". All data used are multi-source spatial data generated based on urban administrative divisions and unified in WGS-84 coordinate system. Table 1 shows the details of the finally extracted 15 indicators.

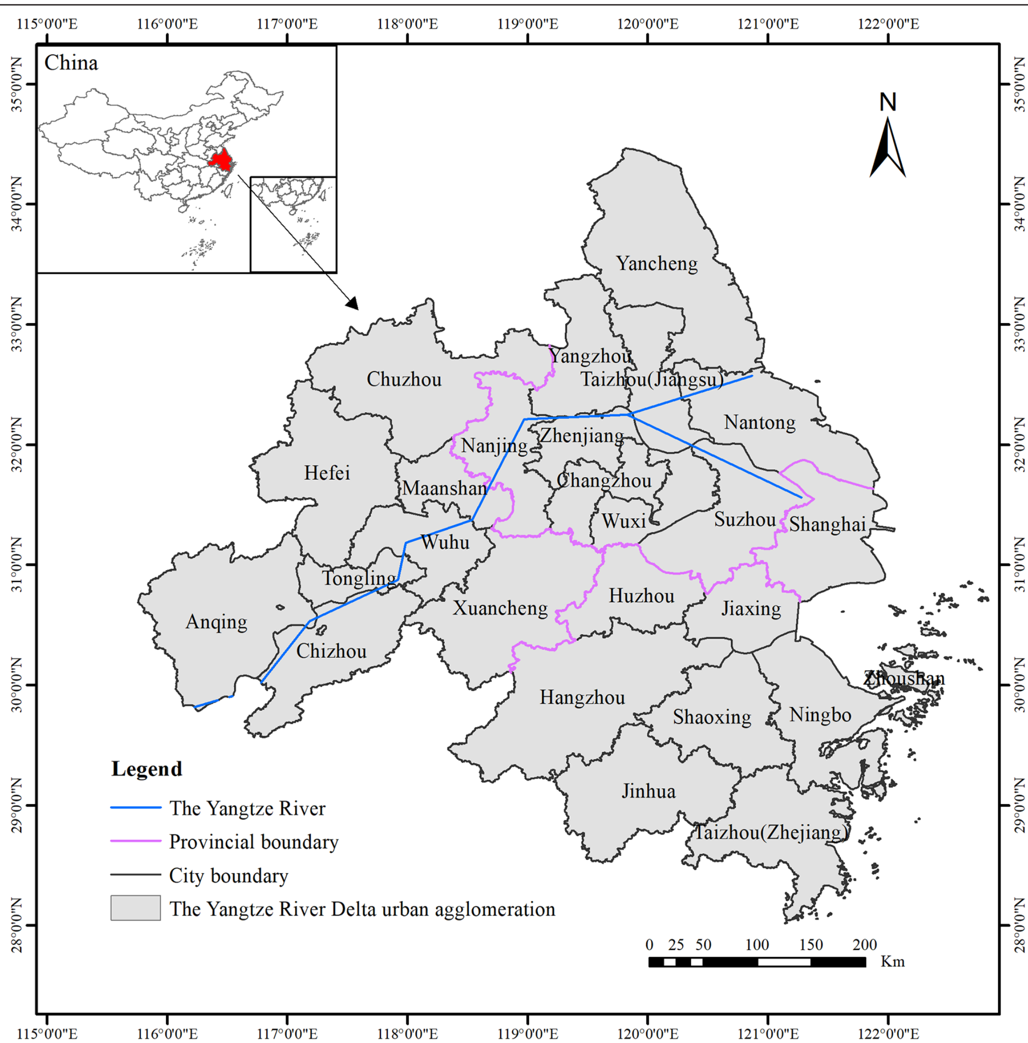

Figure 1. Geographical location of the study area.

Table 1. The description and weight of 15 indicators used in this study.

Evaluative areas	No.	Indicators	Units	Weights
Nature	X_1	Annual total rainfall (−)	mm	0.0032
	X_2	Annual mean temperature (−)	°C	0.0006
	X_3	Vegetation coverage (+)	%	0.1088
Society-Economy	X_4	The proportion of tertiary industry in GDP (+)	%	0.0431
	X_5	Education expenditure (+)	RMB/	0.2096
	X_6	Harmless treatment rate of domestic garbage (+)	%	0.0387
	X_7	Proportion of construction land (+)	%	0.0127
	X_8	Average wage (+)	RMB/	0.0650
	X_9	Comprehensive use rate of industrial solid (+)	%	0.0101
	X_{10}	Total emission of industrial wastewater (−)	Ton	0.1424
	X_{11}	Total emission of industrial SO_2 (−)	Ton	0.0062
	X_{12}	Gross Domestic Product per capita (−)	RMB/	0.0649
	X_{13}	Population density (+)	km²/person	0.0120
	X_{14}	Number of urban unemployed persons registered at the end of the year (−)	person	0.1050
	X_{15}	Proportion of agricultural land (+)	%	0.1777

Note: (+) indicates positive index and (−) indicates negative index.

Methods

The overall workflow of this study is illustrated in Figure 2, mainly including the following steps: (1) data normalization, (2) evaluating UCCC of the cities in the YRDUA by entropy method, and (3) analyzing the spatiotemporal variation and driving factors of UCCC from 2009 to 2019 using GTWR model.

Data Normalization

In this study, there are differences in data dimension, value range, and attribute among each indicator. To make these data comparable, we must first convert the 15 indicators into the same value range through the data normalization method (Wei *et al.* 2016). The specific method is defined by the following equations.

For positive indicators, the data normalization can be expressed as follows:

$$x'_{ijk} = \frac{x_{ijk} - \min(x_j)}{\max(x_j) - \min(x_j)} \tag{1}$$

For negative indicators, the data normalization process is as follows:

$$x'_{ijk} = \frac{\max(x_j) - x_{ijk}}{\max(x_j) - \min(x_j)} \tag{2}$$

where i denotes the year (i = 2009, 2010, ……, 2019), j represents the indicator (*j* = 1, 2, ……15), and *k* demonstrates the city (*k* = 1, 2, ……26). x'_{ijk} and x_{ijk} represent the normalized and initial data, respectively. $\max(x_j)$ and $\min(x_j)$ stand for the largest and the smallest value of the *j*th indicator, respectively. After data normalization, the values of indicators range from 0 to 1.

Besides, there are some outliers in the indicators. Therefore, it is necessary to revise the normalized data to eliminate the influence of outliers (Chen *et al.* 2015). The correction method can be presented as follows:

$$x''_{ijk} = \alpha + x'_{ijk} \tag{3}$$

where α is a fixed coefficient. In this study, α is set as 0.0000001. x''_{ijk} is the revised normalized data.

Evaluating UCCC by Entropy Method

The weight of indicators is determined by entropy method, and then UCCC of each city is calculated. The basic principle of entropy method

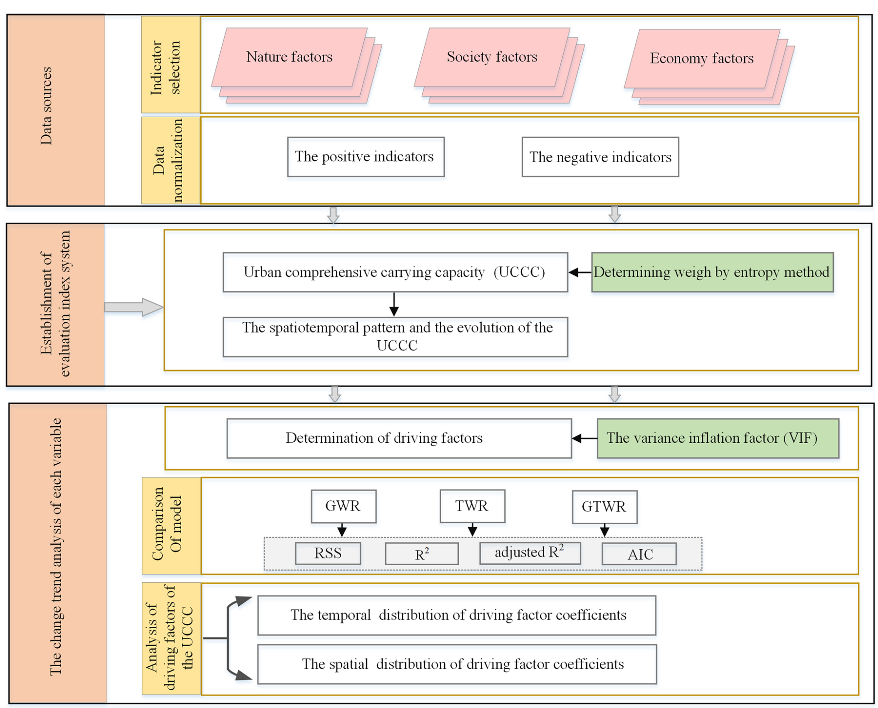

Figure 2. The overall workflow of this study.

is to calculate the weight according to the variability of indicators. Generally, the smaller the entropy is, the greater the variation degree of the indicator is, and the greater its weight is, that is, the greater the role it plays in UCCC evaluation, and vice versa. The specific calculation procedure of entropy method is as follows:

$$P_{ijk} = \frac{x'_{ijk}}{\sum_{i=1}^{11}\sum_{k=1}^{26} x'_{ijk}} \tag{4}$$

$$e_j = -\frac{1}{\ln(N)}\sum_{i=1}^{11}\sum_{k=1}^{26} P_{ijk} \times \ln(P_{ijk}) \tag{5}$$

$$\alpha_j = \frac{1-e_j}{\sum_{j=1}^{15}(1-e_j)} \tag{6}$$

where P_{ijk} is the proportion of indicator j of the city k in year i to the summation value of the indicator j, and e_j represents the entropy value of indicator j. N is the number of indicator j. α_j represents the weight of indicator j.

Based on Equations 4–6, the UCCC S_{ik} of city k in year i can be calculated:

$$S_{ik} = \sum_{j=1}^{15}\alpha_j \times P_{ijk} \tag{7}$$

Analyzing the Spatiotemporal Variation and Driving Factors of UCCC

Selection of Driving Factors

When factors have the same information, it indicates that there is multi-collinearity between factors, which will affect the stability of the model and lead to unreliable results. Therefore, a multi-collinearity test of variables is needed to select the key factors that have a significant impact on the dependent variables before building the model. This study uses the variance inflation factor (VIF) to analyze the multicollinearity between different factors. When VIF < 10, there is no multi-collinearity. When VIF ≥ 10, there is multi-collinearity.

Geographically and Temporally Weighted Regression Model

The GTWR model, proposed by Huang *et al.* (2010), can better reflect the spatiotemporal heterogeneity of different regions, which is a temporal extension of GWR model. It not only solves the problem of the limited number of cross-section data, but also considers the non-stationarity of time and space and can effectively estimate the regression coefficients of the factor. Therefore, this study takes UCCC as the dependent variable and use the GTWR model to reveal the spatiotemporal heterogeneity of each factor. Their formulas are as follows:

$$y_k = \beta_0(\mu_k, \upsilon_k, t_k) + \sum_{j=1}^{10}\beta_j(\mu_k, \upsilon_k, t_k)x_{kj} + \mu_i \tag{8}$$

Where y_k stands for the UCCC of the city k, (μ_k, υ_k, t_k) refers to the spatiotemporal coordinates of the observation point, $\beta_0(\mu_k, \upsilon_k, t_k)$ stands for the intercept term, $\beta_j(\mu_k, \upsilon_k, t_k)$ expresses the regression coefficients of the jth factor, x_{kj} denotes the factor, ε_i represents the random error.

The regression coefficients of the GTWR model are estimated using the weight function as follows:

$$\hat{\beta}(\mu_k, \upsilon_k, t_k) = [X^T W(\mu_k, \upsilon_k, t_k)X]^{-1} X^T W(\mu_k, \upsilon_k, t_k)Y \tag{9}$$

where $W(\mu_k, \upsilon_k, t_k) = diag(a_{k1}, a_{k2},\ldots, a_{kn})$ represents the weight of spatiotemporal distance of nth order, and it is a diagonal matrix.

The spatiotemporal distance is calculated:

$$d_{mn} = \sqrt{\alpha[(\mu_m - \mu_n)^2 + (\upsilon_m - \upsilon_n)^2] + \beta(t_m - t_n)^2} \tag{10}$$

If $\alpha = 0$, only the time distance is considered, the GTWR model is simplified as temporally weighted regression (TWR) model. If $\beta = 0$, only spatial distance is considered, the GTWR model is simplified as GWR model.

The spatiotemporal weight can be expressed as:

$$w_{mn} = exp\{-\frac{\alpha[(\mu_m - \mu_n)^2 + (\upsilon_m - \upsilon_n)^2] + \beta(t_m - t_n)^2}{h^2}\} \tag{11}$$

And the cross-validation method is used to select the optimal bandwidth h to minimize the sum of squares errors:

$$\min CV = [y_k - \hat{y}_{\neq k}(h)]^2 \tag{12}$$

Results

Evaluation Results of the UCCC

The UCCC of Cities in the YRDUA

The value of UCCC can be obtained according to Equation 7, and the results are shown in Table 2. From 2009 to 2019, the results of UCCC in the YRDUA are between 0.1745 and 0.7224, and the UCCC in each city shows a trend of gradual increase. Among these cities, Shanghai has the best performance of UCCC, whilst Huzhou, Zhoushan, Maanshan, Wuhu, and Xuancheng have the worst UCCC performance. Therefore, there are significant spatial differences in UCCC between cities in the YRDUA.

The Performance Level of UCCC for Cities in the YRDUA

Previous studies have confirmed that the natural breaks method is an effective way to analyze the variation trend (Li *et al.* 2019). Therefore, this study uses the natural breaks method to divide the UCCC performance into three levels, namely low (L), medium (M), and high (H) level. The levels of UCCC of each city in the YRDUA during 2009–2019 is shown in Table 3. From 2009 to 2019, the UCCC level of Shanghai is H, which meets the balanced development of society, economy, and ecology. Wuxi, Suzhou, Nantong, Yancheng, Taizhou (Jiangsu), and Hefei present a stable level of M. And Huzhou, Zhoushan, Maanshan, Wuhu, Xuancheng, Chizhou, and Anqing show constant evolution of L. The performance levels of UCCC in Nanjing, Changzhou, Yangzhou, Zhenjiang, Hangzhou, Ningbo, Jiaxing, Shaoxing, Jinhua, and Chuzhou are transited from L to M. Besides, the UCCC of Taizhou (Zhejiang) presents a fluctuation trend.

The UCCC Performance for Zhejiang, Anhui, Jiangsu, and Shanghai

The average scores of UCCC in the three provinces and Shanghai are shown in Figure 3. We can find that UCCC in the YRDUA presents the upward trend during the study period. However, UCCC in Shanghai, Jiangsu, Zhejiang, and Anhui have obvious spatial difference, which can be divided into three stages, and UCCC of Shanghai lies in the highest level. The UCCC levels of Zhejiang and Anhui rank lowest, which are classified into the third stage. The maximum UCCC value in the first stage is almost four times as much as the minimum UCCC value in the third stage. The average UCCC of Jiangsu is around three from 2009 to 2019, so it is categorized as the second stage.

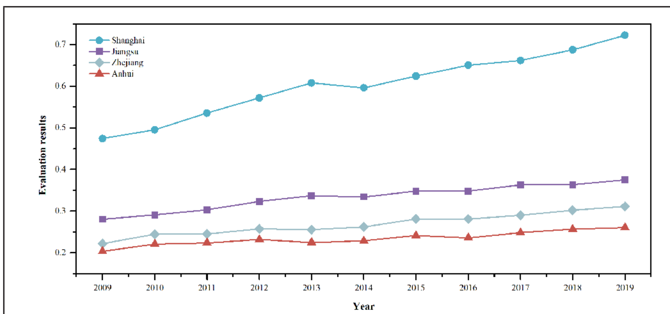

Figure 3. Average score of UCCC in Shanghai, Zhejiang, Anhui, and Jiangsu.

Table 2. The evaluation results of UCCC in the YRDUA from 2009 to 2019.

Province	City	2009	2010	2011	2012	2013	2014	2015	2016	2017	2018	2019
Shanghai	Shanghai	0.4744	0.4956	0.5356	0.5722	0.6080	0.5963	0.6245	0.6506	0.6621	0.6876	0.7224
Jiangsu	Nanjing	0.2681	0.2792	0.2949	0.3238	0.3366	0.3341	0.3556	0.3572	0.3759	0.3857	0.4038
	Wuxi	0.3056	0.3141	0.3288	0.3700	0.3934	0.3757	0.3956	0.3942	0.4126	0.4183	0.4312
	Changzhou	0.2468	0.2556	0.2720	0.3032	0.3181	0.3157	0.3319	0.3283	0.3428	0.3443	0.3548
	Suzhou	0.2871	0.2842	0.2960	0.3464	0.3896	0.3648	0.3848	0.3881	0.4125	0.4165	0.4406
	Nantong	0.3214	0.3328	0.3441	0.3506	0.3559	0.3480	0.3578	0.3589	0.3757	0.3664	0.3810
	Yancheng	0.2903	0.2969	0.3057	0.3073	0.3110	0.3199	0.3332	0.3334	0.3402	0.3417	0.3507
	Yangzhou	0.2722	0.2888	0.3058	0.3123	0.3193	0.3292	0.3370	0.3399	0.3507	0.3508	0.3571
	Zhenjiang	0.2410	0.2526	0.2630	0.2760	0.2860	0.2876	0.2965	0.2965	0.3090	0.3047	0.3111
	Taizhou	0.2918	0.3147	0.3179	0.3204	0.3235	0.3314	0.3408	0.3374	0.3504	0.3432	0.3469
Zhejiang	Hangzhou	0.2403	0.2689	0.2853	0.3035	0.3025	0.3028	0.3411	0.3493	0.3571	0.3817	0.4036
	Ningbo	0.2531	0.2768	0.2760	0.2865	0.2976	0.3007	0.3161	0.3229	0.3396	0.3502	0.3620
	Jiaxing	0.2518	0.2677	0.2716	0.2876	0.2957	0.2958	0.3029	0.3018	0.3168	0.3261	0.3357
	Huzhou	0.1818	0.1968	0.2027	0.2128	0.2074	0.2161	0.2320	0.2296	0.2383	0.2429	0.2492
	Shaoxing	0.2160	0.2484	0.2452	0.2514	0.2441	0.2537	0.2742	0.2690	0.2733	0.2879	0.2971
	Jinhua	0.2115	0.2388	0.2395	0.2445	0.2408	0.2449	0.2735	0.2614	0.2685	0.2830	0.2877
	Zhoushan	0.1887	0.2090	0.1954	0.2167	0.2107	0.2213	0.2277	0.2412	0.2418	0.2530	0.2532
	Taizhou	0.2315	0.2532	0.2446	0.2554	0.2483	0.2617	0.2836	0.2722	0.2874	0.2934	0.3037
Anhui	Hefei	0.2935	0.3151	0.3173	0.3329	0.3209	0.3210	0.3295	0.3160	0.3392	0.3681	0.3729
	Maanshan	0.1779	0.2280	0.2266	0.2348	0.2263	0.2281	0.2472	0.2357	0.2567	0.2661	0.2690
	Wuhu	0.1885	0.2015	0.1980	0.2091	0.2135	0.2156	0.2361	0.2287	0.2454	0.2634	0.2666
	Xuancheng	0.1732	0.1834	0.1882	0.1784	0.1709	0.1735	0.1964	0.1901	0.1994	0.1979	0.2098
	Tongling	0.1760	0.1915	0.2048	0.2164	0.2096	0.2180	0.2122	0.2076	0.2186	0.2239	0.2231
	Chizhou	0.1745	0.1820	0.1795	0.1907	0.1817	0.1816	0.2049	0.2051	0.2102	0.2187	0.2091
	Anqing	0.1799	0.1916	0.1879	0.2003	0.1877	0.1986	0.2102	0.2124	0.2155	0.2159	0.2216
	Chuzhou	0.2639	0.2764	0.2884	0.2927	0.2876	0.2935	0.2950	0.2920	0.3022	0.2995	

Table 3. The performance levels of UCCC in each city.

Province	City	2009	2010	2011	2012	2013	2014	2015	2016	2017	2018	2019
Shanghai	Shanghai	H	H	H	H	H	H	H	H	H	H	H
Jiangsu	Nanjing	L	M	M	M	M	M	M	M	M	M	M
	Wuxi	M	M	M	M	M	M	M	M	M	M	M
	Changzhou	L	L	L	M	M	M	M	M	M	M	M
	Suzhou	M	M	M	M	M	M	M	M	M	M	M
	Nantong	M	M	M	M	M	M	M	M	M	M	M
	Yancheng	M	M	M	M	M	M	M	M	M	M	M
	Yangzhou	L	M	M	M	M	M	M	M	M	M	M
	Zhenjiang	L	L	L	L	M	M	M	M	M	M	M
	Taizhou	M	M	M	M	M	M	M	M	M	M	M
Zhejiang	Hangzhou	L	L	M	M	M	M	M	M	M	M	M
	Ningbo	L	L	L	M	M	M	M	M	M	M	M
	Jiaxing	L	L	L	M	M	M	M	M	M	M	M
	Huzhou	L	L	L	L	L	L	L	L	L	L	L
	Shaoxing	L	L	L	L	L	L	L	L	L	M	M
	Jinhua	L	L	L	L	L	L	L	L	L	M	M
	Zhoushan	L	L	L	L	L	L	L	L	L	L	L
	Taizhou	L	L	L	L	L	L	M	L	M	M	M
Anhui	Hefei	M	M	M	M	M	M	M	M	M	M	M
	Maanshan	L	L	L	L	L	L	L	L	L	L	L
	Wuhu	L	L	L	L	L	L	L	L	L	L	L
	Xuancheng	L	L	L	L	L	L	L	L	L	L	L
	Tongling	L	L	L	L	L	L	L	L	L	L	L
	Chizhou	L	L	L	L	L	L	L	L	L	L	L
	Anqing	L	L	L	L	L	L	L	L	L	L	L
	Chuzhou	L	L	M	M	M	M	M	M	M	M	M

The Selection of Driving Factors

The multi-collinearity tests based on VIF between indicators of UCCC are conducted to select the reasonable driving factors, and the results are shown in Table 4. When the VIF score of a factor is greater than 10, the multi-collinearity between factors should be noticed (Behnke 2006; Krebs 2012). Therefore, the factors of annual total rainfall, annual mean temperature, proportion of construction land, population density, and comprehensive use rate of industrial solid are excluded from the model.

Comparisons of Models

To demonstrate the accuracy and effectiveness of the GTWR model, the panel data are compared with the regression results of GWR, TWR, and GTWR, respectively. The four metrics including R^2, adjusted R^2, the residual sum of squares (RSS), and the Akaike information criterion (AICc) are used to demonstrate the applicability and accuracy of the model. Table 5 shows the comparison results of GWR, TWR, and GTWR models. From Table 5, the R^2 and adjusted R^2 of GTWR are significantly higher than those of GWR and TWR, which indicates that the GTWR has a more satisfactory fitting degree compared with TWR and GWR. The RSS of GTWR is 0.0086, which is smaller than that of GWR and TWR. It is indicated that the GTWR model has the highest accuracy. And the AICc score is reduced from –1464.5500 of TWR and –1625.2700 of GWR to –1763.7900 of GTWR, which also suggests the superiority of GTWR in the model of performance. Therefore, compared with GWR and TWR, the GTWR can better explain the spatiotemporal variation of driving factors on UCCC. Table 6 shows the quartiles of the estimated coefficients using the GTWR model for driving factors. It can be seen that the regression coefficients of each factor have different positive and negative values, and the variation intensity is also extraordinary obvious, which further demonstrates that driving factors of UCCC have significant non-stationarity in time and space.

Table 4. The results of multi-collinearity test for driving factors.

Indicators	VIF
Annual total rainfall	13.4674
Annual mean temperature	14.2432
Vegetation coverage	7.6895
The proportion of tertiary industry in Gross Domestic Product	5.2402
Education expenditure	3.9402
Harmless treatment rate of domestic garbage (pollution)	1.2363
Proportion of construction land	10.8723
Average wage	7.5357
Comprehensive use rate of industrial solid	12.2402
Total emission of industrial wastewater	3.7606
Total emission of industrial SO_2	7.9509
GDP per capita	6.0078
Population density	11.7742
Number of urban unemployed persons registered at the end of the year	3.4884
Proportion of agricultural land	5.4331

VIF = variance inflation factor.

Table 5. Comparison of the results of GWR, TWR, and GTWR models.

Model	R^2	Adjusted R^2	RSS	AICc
GWR	0.9936	0.9934	0.0122	–1625.2700
TWR	0.9591	0.9577	0.0809	–1464.5500
GTWR	0.9954	0.9953	0.0086	–1763.7900

GWR = geographically weighted regression; TWR = temporally weighted regression; GTWR = geographically and temporally weighted regression; RSS = residual sum of squares; AICc = Akaike information criterion.

Analysis of Driving Factors of the UCCC in the YRDUA

The Temporal Distribution of Driving Factors

To clarify the variation tendency of the regression coefficients for each driving factor in the GTWR model, this study uses the violin plots to demonstrate the changes in the distribution of the estimated coefficients for each driving factor, as shown in Figure 4. A violin plot combines the characteristics of the kernel density plot and the box plot. The exterior of the plot presents the distribution of driving factor coefficients, while the core of the plot expresses the interquartile range of this factor (Hintze and Nelson 1998). Some interesting findings are as follows:

(1) **Vegetation coverage (X3)**
The regression coefficients of vegetation coverage show slightly decreasing trend. The skewed distribution shows a left-skewed distribution in 2009–2015 and a right bias in 2016–2019. The bodies of violin plots are becoming larger, reflecting the degree of discretization for regression coefficients are higher. The main reason may be that there are significant differences in urbanization process and implementation in the policy of returning farmland to forest for cities in the YRDUA.

(2) The proportion of tertiary industry in GDP (X4)
The estimation coefficients of the proportion of tertiary industry in GDP show a trend of first decreasing and then increasing. The based distribution shows left-skewed distribution in 2009–2018 and right-skewed distribution in 2019. The regression coefficients of this factor are positive in most areas. During the study period, the remarkable characteristics of the violin plot is that the whole body changes very little in 2009–2017, which indicates that the change of this factor is extremely stable.

Table 6. The estimated coefficients of geographically and temporally weighted regression (GTWR).

Quantile	Minimum	Lower Quartile	Median	Upper Quartile	Maximum
Intercept	0.0252	0.1618	0.2486	0.3345	0.5803
The proportion of tertiary industry in Gross Domestic Product	–0.0583	0.0197	0.0654	0.1258	0.2229
Education expenditure	–0.4577	-0.0042	0.2450	0.3613	0.5600
Harmless treatment rate of domestic garbage	–0.1573	–0.0349	0.0177	0.0832	0.2016
Vegetation coverage	–0.0806	0.0233	0.0907	0.1529	0.2231
Comprehensive use rate of industrial solid	–0.0977	–0.0500	-0.0077	0.0302	0.0622
Total emission of industrial wastewater	–0.2492	–0.1149	–0.0368	0.0162	0.0984
Total emission of industrial SO_2	–0.3685	–0.1664	–0.0671	0.0186	0.1344
GDP per capita	0.0475	0.0807	0.1152	0.1505	0.2247
Number of urban unemployed persons registered at the end of the year	–0.3234	–0.1532	–0.0856	-0.0184	0.2210
Proportion of agricultural land	0.0394	0.1339	0.2291	0.3607	0.5237

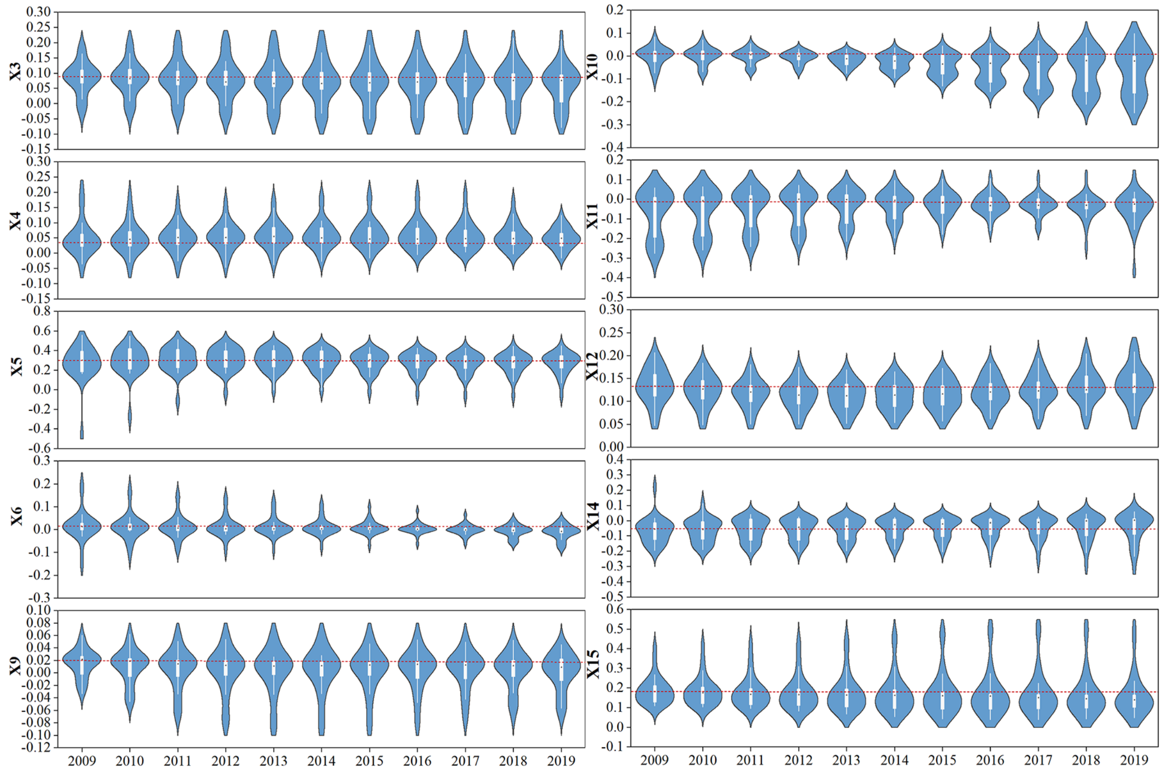

Figure 4. Violin plots of regression coefficients for each driving factor during 2009–2019.

(3) Education expenditure (X5)
The estimated coefficients of education expenditure present a trend of slight increasing first and then decreasing from 2009 to 2019 and show a slight right-skewed trend in 2009–2014. In addition, the effect of this factor on UCCC is positive in almost all areas. The distribution is short-tailed from 2011 to 2019, indicating that the distribution is relatively concentrated.

(4) Harmless treatment rate of domestic garbage (X6)
The regression coefficients of harmless treatment rate of domestic garbage have little variation range. The biased distribution shows a normal distribution in 2009–2013 and a right-biased trend in 2014–2019. The impact of this factor on the UCCC is positive. The shapes of the inner box plot and the outer plot became shorter, indicating the estimated coefficients are increasingly concentrated. The main reason is that with the development of economy, most cities gradually realize the importance of this factor to UCCC.

(5) Comprehensive use rate of industrial solid (X9)
The regression coefficients of comprehensive use rate of industrial solid show a trend of first decreasing in 2009–2014 and then increasing in 2015–2019, and show serious left deviation distribution. Besides, the regression coefficients of comprehensive use rate of industrial solid are positive on the whole, indicating that the impact of this factor on the UCCC is positive in most cities. The violin chart has a long tail, except for 2019, which indicates that the factor estimation coefficients have a very discrete distribution.

(6) Total emission of industrial wastewater (X10)
The estimation coefficients of total emission of industrial wastewater for all the years show a left-offset trend. From the distribution of the factor, the estimated coefficients most are negative in the study area, which indicates that its impact on UCCC is negative. Besides, the estimated coefficients of this factor aggregate slightly from 2009 to 2012 and gradually disperse after 2013. The main reason may lie in the quite different of the number of industrial in each city.

(7) Total emission of industrial SO_2 (X11)
The regression coefficients of total emission of industrial SO_2 present increasing and then decreasing during the study period. The factor shows left deviation trend in 2009–2015 and right deviation trend in 2016–2019. The impact of this factor on UCCC in most areas is negative. From the shape of the violin plots, the regression coefficients of total emission of industrial SO_2 become more concentrated and stable. The potential reason may be that the people's awareness of ecological and environmental protection is gradually enhanced.

(8) GDP per capita (X12)
The estimation coefficients of the GDP per capita demonstrate a trend of slight decreasing and then increasing. The median is first in the middle and then in the lower part of the inner box plot, indicating that the factor is first distributed normally and then right-skewed. Moreover, all the estimation coefficients are positive. From 2013 to 2019, the inner box plot become shorter, and the outer shape become longer, indicating that the estimated coefficients are increasingly concentrated and there are some outliers.

(9) Number of urban unemployed persons registered at the end of the year (X14)
The estimated coefficients of number of urban unemployed persons registered at the end of the year display a gradually increasing trend. The position of the median in the inner of the box plot is also increasing, further proving that the coefficients of this factor increase gradually. Furthermore, the effect of this factor on UCCC is negative in most cities. From the exterior of the plot, the regression coefficients of factors are more and more concentrated. But there is imbalance distribution, and this factor coefficients in some areas are significantly different from that in other cities.

(10) Proportion of agricultural land (X15)
The estimation coefficients of proportion of agricultural land appears decrease gradually during the study period. The median is mostly in the upper part of the box body, indicating that the factor shows a left deviation trend. Moreover, the influence of this driving factor on UCCC is positive in all areas. Its inner box body is

becoming shorter, and the tail of exterior shape gets longer, which indicates the change is greatly unstable.

The Spatial Distribution of Driving Factors

In this study, the Natural Breaks Jenks method is used to classify the regression coefficients for each driving factor in the GTWR model, and the data with the highest similarity are grouped into one class. The spatial distribution map of the coefficients of driving factors are shown in Figure 5. The number of circles in a city expresses the number of estimation coefficients covering the distribution interval during the period of 2009–2019, which reflects the change of driving factors in time. And the size of the circle demonstrates the difference in the distribution interval of the coefficients of driving factors in a city, which can display the spatial non-stationarity distribution.

(1) **Vegetation coverage (X3)**
According to Figure 5a, the vegetation coverage promoted UCCC are primarily concentrated in the north and show a trend of gradual decrease from north to south. The estimated coefficients are distributed between –0.0806 and 0.2231. The regions with high impact of this factor on UCCC are Yancheng, Yangzhou and Taizhou, while the low impact regions are Wuxi, Suzhou,

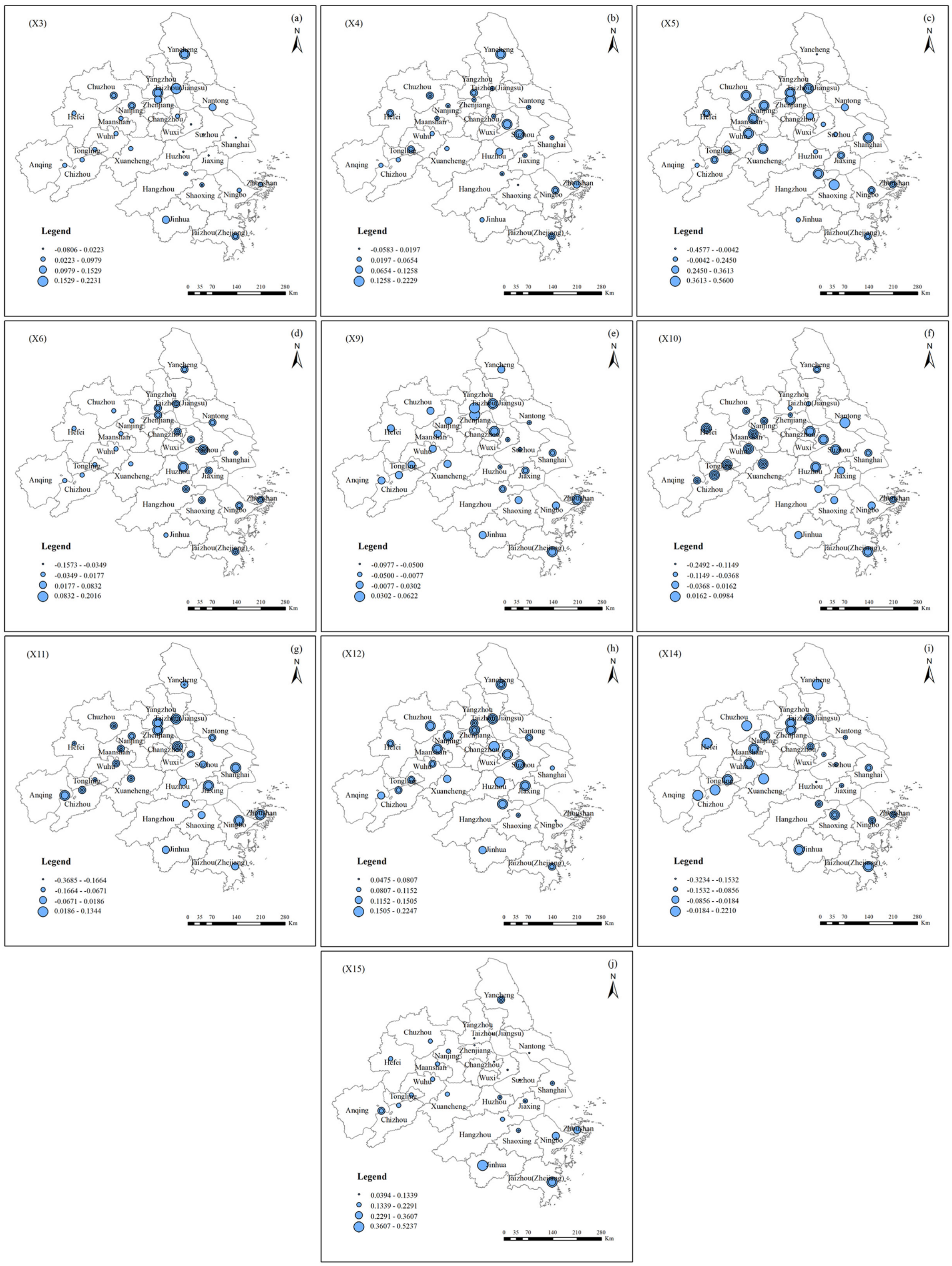

Figure 5. The spatial distribution of driving factors on UCCC in 2009–2019.

Shanghai, Jiaxing, and Huzhou. The time and space distribution characteristics of this driving factor on UCCC may have relations with grain for green policy.

(2) The proportion of tertiary industry in GDP (X4)
Figure 5b shows the distribution of the coefficients of the proportion of the tertiary industry in GDP, showing a trend of high in the northeast and low in the southwest. The estimation coefficients of this factor range from –0.0583 to 0.2229, indicating that the impact of economic structure on UCCC is positive. The highest values are primarily in Wuxi, Suzhou, Yancheng. The city of Shaoxing has the lowest values. Besides, the coefficients of Taizhou (Zhejiang) and Chuzhou showed the largest changes during the study period. Therefore, the impact of this factor on UCCC displays significant spatiotemporal variations.

(3) Education expenditure (X5)
The spatial distribution of regression coefficients of education expenditure is shown in Figure 5c. The estimation coefficients are between –0.4577 and 0.5600. The high value areas mainly accumulate in the southwest such as Chuzhou, Nanjing, Maanshan, Wuhu, Xuancheng, Zhenjiang, Yangzhou, and Taizhou. Furthermore, Shanghai, Hangzhou, and Shaoxing are also high value areas, while the low value area is distributed in Yancheng. The reason may be that the effect of this factor on UCCC related to the government's emphasis on education and the number of schools.

(4) Harmless treatment rate of domestic garbage (X6)
Figure 5d demonstrates that the estimated coefficients of this driving factor are distributed high in the west and low in the east, which ranges from –0.1573 to 0.2016. Through the control of environmental pollution, the ecological environment quality of the city has been improved. Therefore, the impact of this factor on UCCC is positive. The highest areas are mainly concentrated in Suzhou and Huzhou, while the lowest value areas are mostly gathered in Jinhua, Anqing, Chizhou, Tongling, Wuhu, Hefei, Chuzhou, Maanshan, and Nanjing.

(5) Comprehensive use rate of industrial solid (X9)
The spatial distribution of the coefficients of comprehensive use rate of industrial solid is shown in Figure 5e, and its influence on UCCC shows an increasing-decreasing-increasing gradient distribution trend from northwest to southeast. The estimation coefficients are between –0.0977 and 0.0622. This factor in most areas is to promote UCCC, especially in Yangzhou, Taizhou (Jiangsu), Zhenjiang, Changzhou, Taizhou (Zhejiang), and Zhoushan. However, UCCC in Nantong, Wuxi, Huzhou, and Suzhou are least affected by this factor.

(6) Total emission of industrial wastewater (X10)
Figure 5f shows that the spatial distribution of the coefficients of total emission of industrial wastewater. Their values range from –0.2492 to 0.0984. Total emission of industrial wastewater has a negative effect on UCCC. The distribution of this factor displays a very obvious aggregation. However, the influence of this factor on UCCC varies widely among all cities in Anhui province during the study period, which may be related to the policies issued by the province. In addition, there are small clusters in Nantong, Changzhou, Wuxi, Suzhou, and Huzhou.

(7) Total emission of industrial SO_2 (X11)
Figure 5g shows that the distribution of the coefficients of total emission of industrial SO_2, which ranges from –0.3685 to 0.1344. This factor weakens UCCC in most cities of the study area. The coefficients of cities on both sides of the Yangtze River change the most during the study period, especially Chizhou, Tongling, Xuancheng, Wuhu, Maanshan, and Hefei. In addition, total emission of industrial SO_2 had a strong inhibition effect on UCCC in Hefei and Tongling.

(8) GDP per capita (X12)
According to Figure 5h, the regions where GDP per capita plays an important role in promoting UCCC are mainly concentrated in the north, and the estimated coefficients are between 0.0475 and 0.2247. The high value areas are primarily distributed in Yancheng, Taizhou (Jiangsu), Zhenjiang, Nanjing, Chuzhou, Maanshan, Changzhou, Wuxi, Suzhou, Jiaxing, and Hangzhou, while the low value areas are mainly distributed in Shaoxing, Ningbo, and Zhoushan. Besides, the influence of this factor on UCCC in Yancheng, Taizhou (Zhejiang), Yangzhou, and Zhenjiang have a strong non-stationary time, which may relate to economic structure and economic efficiency.

(9) Number of urban unemployed persons registered at the end of the year (X14)
Figure 5i shows the spatial distribution of the regression coefficients of the number of urban unemployed persons registered at the end of the year. The range of the regression coefficients are from –0.3234 to 0.2210, indicating that this factor has a negative effect on UCCC. The high-value regions are mainly distributed in the cities on both sides of the Yangtze River, which may be due to the increase in labor demand, and the decrease in the unemployed people. The low-value regions are mostly in Nantong, Wuxi, Suzhou, and Huzhou, and the result is connected with unemployment mobility.

(10) Proportion of agricultural land (X15)
The spatial distribution for the coefficients of proportion of agricultural land is shown in Figure 5j. The regression coefficients are between 0.0394 and 0.5237, indicating that the proportion of agricultural land has a positive effect on UCCC. The impact of this factor on UCCC is greatest in the southeast including Jinhua, Ningbo, Zhoushan, and Taizhou (Zhejiang), while the least affected areas are in the northern cities of the YRDUA, including Yangzhou, Zhenjiang, Changzhou, Wuxi, Suzhou, Shanghai, Jiaxing, and Huzhou.

Discussion

This study selects 15 indicators from three aspects of nature, society, and economy, and uses entropy method to analysis UCCC evolution of the YRDUA from 2009 to 2019. On this basis, we explore the spatiotemporal heterogeneity of driving factors by using GTWR model. Three points can be highlighted.

Firstly, in the YRDUA, the best UCCC performance level is in Shanghai, followed by Jiangsu, Zhejiang, and Anhui, indicating that the degree of regional integration in the YRDUA is low. The reason may be that Shanghai can provide more resources and a higher level of infrastructure than other cities. Jiangsu is often in the middle level all the time, but Zhejiang and Anhui provinces remain at a low level from 2009 to 2019. The gap of UCCC in different provinces is primary caused by development mode and natural resources dependence. In addition, compared with other cities, provincial capitals and municipalities can provide more sufficient economic development potential and social reserves, so their UCCC is relatively high.

Secondly, the UCCC of cities in the YRDUA is generally at the medium level. But with the enhancing awareness of sustainable development, the level of UCCC presents continuous rising and has a trend of gradual improvement in each city. Furthermore, there is obvious spatiotemporal heterogeneity of UCCC in the YRDUA during 2009–2019, with the high value regions concentrated in the east and the low value regions primary in the west. The main reason is that the cities in the eastern with higher UCCC are relatively developed in terms of resources, economy, and environment.

Thirdly, the intensity change of each driving factor has non-stationarity in temporal and spatial dimension. Due to the different development stages of each city in the YRDUA, the driving factors of UCCC will also change. For example, in the period of urban rapid development, industrial environmental pollution treatment and resource demand have positive effects on UCCC. In well-developed cities, such as Shanghai, education expenditure, and investment in science and technology play a dominant role. Therefore, the same factor produces different effects in different regions and time.

To achieve sustainable development, some policy recommendations for improving UCCC in the YRDUA are tried to provide in this study.

Firstly, it is necessary to fully consider the characteristics of each subsystem carrying capacity in nature, society, and economy. Secondly, due to the unbalanced development of space, decision makers should strengthen the cooperation between the east and west regions, deepen the radiation effect of the cities with high UCCC to surrounding cities, and explore a win-win coordinated development model. Thirdly, the government should carry out top-level design for sustainable development of each city according to the spatiotemporal conditions of driving factors.

Conclusions

Under the impact of rapid urbanization, the YRDUA is facing the severe test of sustainable development. Therefore, this study takes 26 cities in the YRDUA as the research objects, and extracts 15 indicators from the three aspects of nature, society, and economy to comprehensively evaluate UCCC of each city in the YRDUA from 2009 to 2019. Besides, this study explores the spatiotemporal characteristics of driving factors by GTWR model. Some primary conclusions can be drawn: (1) there is a significant spatial heterogeneity of UCCC in the YRDUA, with a trend of high in the east and low in the west. Among these cities, Shanghai has the best level of UCCC performance, followed by Jiangsu, Zhejiang, and Anhui provinces. (2) The UCCC of cities in the YRDUA is generally at medium level and presents a gradually increasing trend. (3) Ten driving factors, including industrial structure, education expenditure, and harmless treatment rate of domestic waste and so on, have a significant influence on UCCC, and the influence intensity is non-stationary in time and space. These findings can be helpful to understand the driving factors of UCCC in the YRDUA and provide theoretical basis for realizing the sustainable development in the future.

Acknowledgments

The authors are sincerely grateful to the editors as well as the anonymous reviewers for their valuable suggestions and comments that helped us improve this paper significantly.

References

Allouhi, A., Y. El Fouih, T. Kousksou, A. Jamil, Y. Zeraouli and Y. Mourad. 2015. Energy consumption and efficiency in buildings: Current status and future trends. *Journal of Cleaner Production* 109:118–130.

Beck, U. 1992. From industrial society to the risk society: Questions of survival, social structure and ecological enlightenment. *Theory, Culture & Society* 9(1):97–123.

Behnke, J. 2006. Discovering statistics using SPSS. *Politische Vierteljahresschrift* 47(4):751–753.

Chen, J., Y. Wu, J. Wen, S. Cheng and J. Wang. 2017. Regional differences in China's fossil energy consumption: an analysis for the period 1997–2013. *Journal of Cleaner Production* 142:578–588.

Chen, J., Y. Zhang, Z. Chen and Z. Nie. 2015. Improving assessment of groundwater sustainability with analytic hierarchy process and information entropy method: A case study of the Hohhot Plain, China. *Environmental Earth Sciences* 73(5):2353–2363.

Fan, C. 2009. China's technology policies related to sustainable environment. In *Proceedings Sustainability 2009—The Next Horizon Conference,* held in Melbourne, Fla.

Edmonds, R. L. 2005. China's environment and the challenge of sustainable development. *China Quarterly* 184:971–973.

Fang, C. 2015. Important progress and future direction of studies on China's urban agglomerations. *Journal of Geographical Sciences* 25(08):1003–1024.

Guo, A. Q. and H. Liu. 2011. A study of urban land carrying capacity in Hebei province. In *Proceedings 3rd International Conference on Information Technology and Computer Science,* held in Huangshi, Peoples Republic of China.

Heikkila, E. and Y. Xu. 2013. Seven prototypical Chinese cities. *Urban Studies* 51(4):827–847.

Hintze, J. L. and R. D. Nelson. 1998. Violin plots: A box plot-density trace synergism. *American Statistician* 52(2):181–184.

Huang, B., B. Wu and M. Barry. 2010. Geographically and temporally weighted regression for modeling spatio-temporal variation in house prices. *International Journal of Geographical Information Science* 24(3):383–401.

Krebs, P., N. Koutsias and M. Conedera. 2012. Modelling the eco-cultural niche of giant chestnut trees: New insights into land use history in southern Switzerland through distribution analysis of a living heritage. *Journal of Historical Geography* 38(4):372–386.

Li, Y., C. Liu, H. Zhang and X. Gao. 2011. Evaluation on the human settlement's environment suitability in the Three Gorges Reservoir area of Chongqing based on RS and GIS. *Journal of Geographical Sciences* 21(2):346–358.

Li, Y., H. Commenges, F. Bordignon, C. Bonhomme and J.-F. Deroubaix. 2019. The Tianjin Eco-City model in the academic literature on urban sustainability. *Journal of Cleaner Production* 213:59–74.

Liu, M. Y., J. Y. Zhang, C. H. Wang and H. Lu. 2019. Research on water resources carrying capacity of Changzhou city based on neural network. *Fresenius Environmental Bulletin* 28(4):2725–2732.

Liu, Z., Y. Ren, L. Shen, X. Liao, X. Wei and J. Wang. 2020. Analysis on the effectiveness of indicators for evaluating urban carrying capacity: A popularity-suitability perspective. *Journal of Cleaner Production* 246:119019.

Pandit, A., B. Bras, E. A. Minné, E. Dunham-Jones, G. Augenbroe, H. Jeong, J.-A. C. James, J. P. Newell, M. Weissburg, M. A. Brown, M. E. Chang, M. Xu, M. M. Begovic, P. Yang, R. M. Fujimoto, S. P. French, V. M. Thomas, X. Yu, Y. Chen, Z. Lu and J. C. Crittenden. 2017. Infrastructure ecology: an evolving paradigm for sustainable urban development. *Journal of Cleaner Production* 163:S19–S27.

Shan, W. and F. F. Wang. 2021. An impact assessment of energy undesirable output on climate-carrying capacity: A case study of Shanghai. *Environmental Science and Pollution Research* 28(30):40126–40136.

Tian, P., H. Wu, T. Yang, F. Jiang, W. Zhang, Z. Zhu, Q. Yue, M. Liu and X. Xu. 2021. Evaluation of urban water ecological civilization: A case study of three urban agglomerations in the Yangtze River economic belt, China. *Ecological Indicators* 123:107351.

Tran, L. 2016. An interactive method to select a set of sustainable urban development indicators. *Ecological Indicators* 61:418–427.

Walz, R. 2000. Development of environmental indicator systems: Experiences from Germany. *Environmental Management* 25(6):613–623.

Wang, J., L. Shen, Y. Ren, X. Wei, Y. Tan and T. Shu. 2019. An alternative model for evaluating the balance of carrying capacity between functional urban infrastructures. *Environmental Impact Assessment Review* 79:106304.

Wang, J., X. Wei and Q. Guo. 2018. A three-dimensional evaluation model for regional carrying capacity of ecological environment to social economic development: Model development and a case study in China. *Ecological Indicators* 89:348–355.

Wang, Q., Y. Wang, W. Chen, X. Zhou, M. Zhao and B. Zhang. 2020. Do land price variation and environmental regulation improve chemical industrial agglomeration? A regional analysis in China. *Land Use Policy* 94:104568.

Wei, Y. G., C. Huang, J. Li and L. Xie. 2016. An evaluation model for urban carrying capacity: A case study of China's mega-cities. *Habitat International* 53:87–96.

Yang, C. Y. and H. M. Li. 2011. Comparative analysis of domestic and international ecological civilization theory. *Applied Mechanics and Materials* 71–78. http://doi.org/10.4028/www.scientific.net/AMM.71-78.2695.

Yuan, H. X., Y. Feng, J. Lee and H. Liu. 2020. The spatio-temporal heterogeneity of financial agglomeration on green development in China cities using GTWR model. *Sustainability* 12(16).

Zhang, M., Y. Liu, J. Wu and T. Wang. 2018. Index system of urban resource and environment carrying capacity based on ecological civilization. *Environmental Impact Assessment Review* 68:90–97.

Zhang, Y., C. Shuai, J. Bian, X. Chen, Y. Wu and L. Shen. 2019. Socioeconomic factors of PM2.5 concentrations in 152 Chinese cities: Decomposition analysis using LMDI. *Journal of Cleaner Production* 218:96–107.

Zhou, Y., Y. Shan, G.-S. Liu and D. Guan. 2018. Emissions and low-carbon development in Guangdong-Hong Kong-Macao Greater Bay Area cities and their surroundings. *Applied Energy* 228:1683–1692.

WHO'S WHO IN ASPRS

Founded in 1934, the American Society for Photogrammetry and Remote Sensing (ASPRS) is a scientific association serving thousands of professional members around the world. Our mission is to advance knowledge and improve understanding of mapping sciences to promote the responsible applications of photogrammetry, remote sensing, geographic information systems (GIS) and supporting technologies.

BOARD OF DIRECTORS

BOARD OFFICERS

President
Christopher Parrish, Ph.D
Oregon State University

President-Elect
Lorraine B. Amenda, PLS, CP
Towill, Inc.

Vice President
Bandana Kar
Oak Ridge National Lab

Past President
Jason M. Stoker, Ph.D,
U.S. Geological Survey

Treasurer
John McCombs
NOAA

Secretary
Harold Rempel
ESP Associates, Inc.

COUNCIL OFFICERS

ASPRS has six councils. To learn more, visit https://www.asprs.org/Councils.html.

Sustaining Members Council
Chair: Ryan Bowe
Deputy Chair: Melissa Martin

Technical Division Directors Council
Chair: Bill Swope
Deputy Chair: Hope Morgan

Standing Committee Chairs Council
Chair: David Stolarz
Deputy Chair: TBA

Early-Career Professionals Council
Chair: Madeline Stewart
Deputy Chair: Kyle Knapp

Region Officers Council
Chair: Demetrio Zourarakis
Deputy Chair: Jason Krueger

Student Advisory Council
Chair: Lauren McKinney-Wise
Deputy Chair: Oscar Duran

TECHNICAL DIVISION OFFICERS

ASPRS has seven professional divisions. To learn more, visit https://www.asprs.org/Divisions.html.

Geographic Information Systems Division
Director: Denise Theunissen
Assistant Director: Jin Lee

Lidar Division
Director: Ajit Sampath
Assistant Director: Mat Bethel

Photogrammetric Applications Division
Director: Ben Wilkinson
Assistant Director: Hank Theiss

Primary Data Acquisition Division
Director: Greg Stensaas
Assistant Director: Srini Dharmapuri

Professional Practice Division
Director: Bill Swope
Assistant Director: Hope Morgan

Remote Sensing Applications Division
Director: Amr Abd-Ehrahman
Assistant Director: Tao Liu

Unmanned Autonomous Systems (UAS)
Director: Jacob Lopez
Assistant Director: Bahram Salehi

REGION PRESIDENTS

ASPRS has 13 regions to serve the United States. To learn more, visit https://www.asprs.org/regions.html.

Alaska Region

Cascadia Region
Robert Hariston-Porter

Eastern Great Lakes Region
Michael Joos, CP, GISP

Florida Region
Xan Fredericks

Heartland Region
Whit Lynn

Intermountain Region
Robert T. Pack

Mid-South Region
David Hughes

Northeast Region

North Atlantic Region

Pacific Southwest Region
John Erickson, PLS, CP

Potomac Region
Dave Lasko

Rocky Mountain Region

Western Great Lakes Region
Adam Smith

SUSTAINING MEMBERS

ACI USA Inc.
Weston, Florida
https://acicorporation.com/
Member Since: 2/2018

Aerial Services, Inc.
Cedar Falls, Iowa
www.AerialServicesInc.com
Member Since: 5/2001

Airworks Solutions Inc.
Boston, Massachusetts
Member Since: 3/2022

Applanix
Richmond Hill, Ontario, Canada
http://www.applanix.com
Member Since: 7/1997

Ayres Associates
Madison, Wisconsin
www.AyresAssociates.com
Member Since: 1/1953

CT Consultants
Mentor, Ohio
Member Since: 3/2022

Dewberry
Fairfax, Virginia
www.dewberry.com
Member Since: 1/1985

Esri
Redlands, California
www.esri.com
Member Since: 1/1987

GeoCue Group
Madison, Alabama
http://www.geocue.com
Member Since: 10/2003

Geographic Imperatives LLC
Centennial, Colorado
Member Since: 12/2020

GeoWing Mapping, Inc.
Richmond, California
www.geowingmapping.com
Member Since: 12/2016

Halff Associates, Inc.
Richardson, Texas
www.halff.com
Member Since: 8/2021

Keystone Aerial Surveys, Inc.
Philadelphia, Pennsylvania
www.kasurveys.com
Member Since: 1/1985

Kucera International
Willoughby, Ohio
www.kucerainternational.com
Member Since: 1/1992

L3Harris Technologies
Broomfield, Colorado
www.l3harris.com
Member Since: 6/2008

Merrick & Company
Greenwood Village, Colorado
www.merrick.com/gis
Member Since: 4/1995

Nearmap
South Jordan, Utah
www.nearmap.com
Member Since: 6/2023

NV5 Geospatial
Sheboygan Falls, Wisconsin
www.quantumspatial.com
Member Since: 1/1974

Pickett and Associates, Inc.
Bartow, Florida
www.pickettusa.com
Member Since: 4/2007

Riegl USA, Inc.
Orlando, Florida
www.rieglusa.com
Member Since: 11/2004

Robinson Aerial Surveys, Inc.(RAS)
Hackettstown, New Jersey
www.robinsonaerial.com
Member Since: 1/1954

Sanborn Map Company
Colorado Springs, Colorado
www.sanborn.com
Member Since: 10/1984

Surdex Corporation
Chesterfield, Missouri
www.surdex.com
Member Since: 12/2011

Surveying And Mapping, LLC (SAM)
Austin, Texas
www.sam.biz
Member Since: 12/2005

T3 Global Strategies, Inc.
Bridgeville, Pennsylvania
https://t3gs.com/
Member Since: 6/2020

Towill, Inc.
San Francisco, California
www.towill.com
Member Since: 1/1952

Woolpert LLP
Dayton, Ohio
www.woolpert.com
Member Since: 1/1985

SUSTAINING MEMBER BENEFITS

Membership

- ✓ Provides a means for dissemination of new information
- ✓ Encourages an exchange of ideas and communication
- ✓ Offers prime exposure for companies

Benefits of an ASPRS Membership

- Complimentary and discounted Employee Membership*
- E-mail blast to full ASPRS membership*
- Professional Certification Application fee discount for any employee
- Member price for ASPRS publications
- Discount on group registration to ASPRS virtual conferences
- Sustaining Member company listing in ASPRS directory/website
- Hot link to company website from Sustaining Member company listing page on ASPRS website
- Press Release Priority Listing in *PE&RS* Industry News
- Priority publishing of Highlight Articles in *PE&RS* plus, 20% discount off cover fee
- Discount on *PE&RS* advertising
- Exhibit discounts at ASPRS sponsored conferences (exception ASPRS/ILMF)
- Free training webinar registrations per year*
- Discount on additional training webinar registrations for employees
- Discount for each new SMC member brought on board (Discount for first year only)

*quantity depends on membership level

Special Advertising Opportunities

FRONT COVER SPONSORSHIP

A *PE&RS* cover sponsorship is a unique opportunity to capture the undivided attention of your target market through three premium points of contact.

1— *PE&RS* FRONT COVER

(Only twelve available, first-come, first-served)
PE&RS is world-renowned for the outstanding imagery displayed monthly on its front cover—and readers have told us they eagerly anticipate every issue. This is a premium opportunity for any company, government agency, university or non-profit organization to provide a strong image that demonstrates their expertise in the geospatial information industry.

2— FREE ACCOMPANYING "HIGHLIGHT" ARTICLE

A detailed article to enhance your cover image is welcome but not a condition of placing an image. Many readers have asked for more information about the covers and your article is a highly visible way to tell your story in more depth for an audience keenly interested in your products and services. No article is guaranteed publication, as it must pass ASPRS editorial review. For more information, contact Rae Kelley at rkelley@asprs.org.

3— FREE TABLE OF CONTENTS COVER DESCRIPTION

Use this highly visible position to showcase your organization by featuring highlights of the technology used in capturing the front cover imagery. Limit 200-word description.

Terms: Fifty percent nonrefundable deposit with space reservation and payment of balance on or before materials closing deadline.

Cover Specifications: Bleed size: 8 5/8" × 11 1/4", Trim: 8 3/8" × 10 7/8"

PRICING

	Sustaining Member Exhibiting at a 2023 ASPRS Conference	Sustaining Member	Exhibitor	Non Member
Cover 1	$1,850	$2,000	$2,350	$2,500

Belly Bands, Inserts, Outserts & More!

Make your material the first impression readers have when they get their copy of *PE&RS*. Contact Bill Spilman at bill@innovativemediasolutions.com

VENDOR SEMINARS

ASPRS Sustaining Members now have the opportunity to hold a 1-hour informational session as a Virtual Vendor Seminar that will be free to all ASPRS Members wishing to attend. There will be one opportunity per month to reach out to all ASPRS Members with a demonstration of a new product, service, or other information. ASPRS will promote the Seminar through a blast email to all members, a notice on the ASPRS web site home page, and ads in the print and digital editions of *PE&RS*.

The Virtual Seminar will be hosted by ASPRS through its Zoom capability and has the capacity to accommodate 500 attendees.

Vendor Seminars	
Fee	$2,500 (no discounts)

DIGITAL ADVERTISING OPPORTUNITIES

EMPLOYMENT PROMOTION

When you need to fill a position right away, use this direct, right-to-the-desktop approach to announce your employment opportunity. The employment opportunity will be sent once to all ASPRS members in our regular Wednesday email newsletter to members, and will be posted on the ASPRS Web site for one month. This type of advertising gets results when you provide a web link with your text.

Employment Opportunity	Net Rate
30-Day Web + 1 email	$500/opportunity
Web-only (no email)	$300/opportunity

Do you have multiple vacancies that need to be filled? Contact us for pricing details for multiple listings.

NEWSLETTER DISPLAY ADVERTISING

Your vertical ad will show up in the right hand column of our weekly newsletter, which is sent to more than 3,000 people, including our membership and interested parties. **Open Rate: 32.9%**

Newsletter vertical banner ad	Net Rate
180 pixels x 240 pixels max	$500/opportunity

DEDICATED CONTENT EMAIL BLAST

Send a dedicated email blast to the ASPRS email list. Advertiser supplies HTML (including images). Lead time: 14 days.

Materials	Net Rate
Advertiser supplies HTML, including images.	$3000/ opportunity

PE&RS Digital Edition

Digital Edition Announcement E-Mail: 5,800+

PE&RS is available online in both a public version that is available to anyone but does not include the peer-reviewed articles, and a full version that is available to ASPRS members only upon login.

The enhanced version of *PE&RS* contains hot links for all ASPRS Sustaining Member Companies, as well as hot links on advertisements, ASPRS Who's Who, and internet references.

Become a sponsor today!

The e-mail blast sponsorship opportunity includes a **180 x 240 pixel ad** in the email announcement that goes out to our membership announcing the availability of the electronic issue.

Digital Edition Opportunities	Net Rate
E-mail Blast Sponsorship*	$1,000

Landsat's Enduring Legacy

Pioneering Global Land Observations from Space

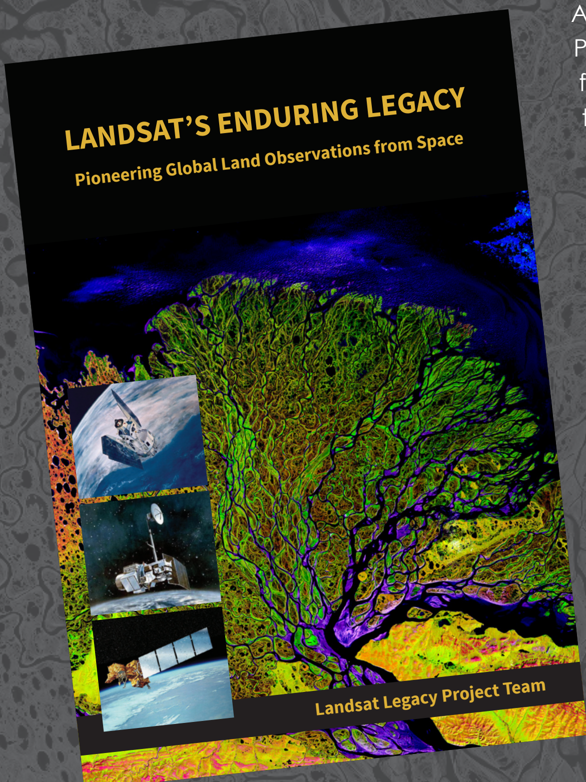

After more than 15 years of research and writing, the Landsat Legacy Project Team published, in collaboration with the American Society for Photogrammetry and Remote Sensing (ASPRS), a seminal work on the nearly half-century of monitoring the Earth's lands with Landsat. Born of technologies that evolved from the Second World War, Landsat not only pioneered global land monitoring but in the process drove innovation in digital imaging technologies and encouraged development of global imagery archives. Access to this imagery led to early breakthroughs in natural resources assessments, particularly for agriculture, forestry, and geology. The technical Landsat remote sensing revolution was not simple or straightforward. Early conflicts between civilian and defense satellite remote sensing users gave way to disagreements over whether the Landsat system should be a public service or a private enterprise. The failed attempts to privatize Landsat nearly led to its demise. Only the combined engagement of civilian and defense organizations ultimately saved this pioneer satellite land monitoring program. With the emergence of 21st century Earth system science research, the full value of the Landsat concept and its continuous 45-year global archive has been recognized and embraced. Discussion of Landsat's future continues but its heritage will not be forgotten.

The pioneering satellite system's vital history is captured in this notable volume on Landsat's Enduring Legacy.

Landsat Legacy Project Team

Samuel N. Goward
Darrel L. Williams
Terry Arvidson
Laura E. P. Rocchio
James R. Irons
Carol A. Russell
Shaida S. Johnston

Landsat's Enduring Legacy

Hardback. 2017, ISBN 1-57083-101-7

Member/Non-member	$48*
Student Member	$36*

* Plus shipping

Order online at

www.asprs.org/landsat

asprs THE IMAGING & GEOSPATIAL INFORMATION SOCIETY